Eur. Phys. J. B 72, 323–359 (2009)
DOI: 10.1140/epjb/e2009-00378-9

THE EUROPEAN
PHYSICAL JOURNAL B

Colloquium

Front-end process modeling in silicon

L. Pelaz[a], L.A. Marqués, M. Aboy, P. López, and I. Santos

Departamento de Electrónica, E.T.S.I. de Telecomunicación, Universidad de Valladolid, 47011 Valladolid, Spain

Received 5 August 2009 / Received in final form 25 September 2009
Published online 7 November 2009 – © EDP Sciences, Società Italiana di Fisica, Springer-Verlag 2009

Abstract. Front-end processing mostly deals with technologies associated to junction formation in semiconductor devices. Ion implantation and thermal anneal models are key to predict active dopant placement and activation. We review the main models involved in process simulation, including ion implantation, evolution of point and extended defects, amorphization and regrowth mechanisms, and dopant-defect interactions. Hierarchical simulation schemes, going from fundamental calculations to simplified models, are emphasized in this Colloquium. Although continuum modeling is the mainstream in the semiconductor industry, atomistic techniques are starting to play an important role in process simulation for devices with nanometer size features. We illustrate in some examples the use of atomistic modeling techniques to gain insight and provide clues for process optimization.

PACS. 02.70.-c Computational techniques; simulations – 61.72.Cc Kinetics of defect formation and annealing – 61.72.J- Point defects and defect clusters – 61.72.uf Ge and Si

1 Introduction

The International Technology Roadmap for Semiconductors (ITRS) provides the guidelines for the development of semiconductor devices in different aspects [1]. A chapter devoted to modeling and simulation indicates its relevance in the semiconductor industry. As many other technological fields, the fabrication and design of new integrated circuits (ICs) makes intensive use of Technology Computer-Aided Design tools. Although experimental tests are essential for the development and optimization of new technologies, modeling and simulation are becoming fundamental to reduce the development times and cost. Simulation tools are used in the different steps of the fabrication chain from the equipment-related issues to the material properties. Front-end process modeling deals with the simulation of the physical effects of manufacturing steps used to build transistors, and it is mostly concerned with junction formation. This information can then be used as input for device simulation to predict the electrical device behavior. The intrinsic electrical device performance goals drive the design of the junctions and in turn the requirements on dopant placement and activation. Therefore, the accurate prediction of dopant distribution and activation during the fabrication processes is one of the main goals of process modeling.

The most common technique used to selectively introduce dopants in the Si substrate and define junctions is ion implantation because it allows a precise control of the amount and distribution of dopants [2]. However, as the energetic incoming ions penetrate into the substrate the Si crystal lattice is damaged. Damage consists of Si self-interstitials (Is), vacancies (Vs) or agglomerates of these defects [3–5]. But the lattice can be completely amorphized if the implant dose is high enough [6]. Generally the as-implanted dopant atoms do not lie in substitutional lattice sites and they are electrically inactive. Subsequent thermal anneals are required to heal the crystal damage and to place the dopants in substitutional sites. Dopants and intrinsic lattice defects, Is and Vs, interact leading to mobile dopant species and to dopant-defect agglomerates that prevent their electrical activation. Since a large defect supersaturation (defect concentration compared to that in equilibrium) is created during ion implantation, the effects resulting from dopant-defect interactions are boosted. Thus, dopant diffusivity is enhanced and dopant activation is reduced compared to equilibrium values [7–15]. These effects are transient because defect supersaturation evolves toward equilibrium.

Device scaling allows a higher level of integration in ICs with improved cost/performance ratio. However, this evolution entails a number of technological challenges. At the junction level, the need to control the Short Channel Effects (SCE) in Metal-Oxide Semiconductor Field Effect Transistor (MOSFET) devices has motivated the progressive reduction of junction depth at the source and drain (S/D) extensions. This requires not only the shallow introduction of dopants but also the control of their diffusivity to avoid the profile broadening. The maximization of drive current for higher switching speed involves a minimization

[a] e-mail: lourdes@ele.uva.es

of access resistance. This requisite demands a high dopant activation and has also driven the development of strain technologies to enhance carrier mobility [16]. The minimization of off-state currents, especially for low-power applications, entails the removal of lattice defects as they may induce energy states in the gap responsible for additional leakage [17]. Dopant activation and defect removal generally require large thermal budgets, which cause the spreading of the junction depth, and therefore, deteriorate SCE control. The difficult trade-off between shallow and abrupt junction formation, maximum dopant activation and defect removal becomes more and more challenging as device dimensions shrink [1].

Thermal budgets with higher temperature and reduced times offer a better compromise for dopant diffusion and activation [18]. Thus, for S/D extension formation traditional furnace anneals have been substituted by other anneal schemes such as spike rapid thermal processes (temperatures around 1000 °C for a few seconds) or more recently, by the so-called millisecond anneals [19] (the substrate is exposed to the burst of flash-lamps [20] or to a sub-melting laser pulse [21] for about 1 ms with ultra fast temperature ramp-up and ramp-down). The use of Solid Phase Epitaxial Regrowth (SPER) of amorphous Si layers (a-layers) has been proved to result in a high dopant activation and with minimal diffusion [22–24]. However, the stable residual damage that remains beyond the amorphous/crystalline (a/c) interface is a pressing concern because millisecond anneals may not be able to completely remove them. Excimer laser annealing has also been considered for the healing of crystal damage and activation of dopants in particular device structures [25–27]. To be able to maintain a good SCE control while fulfilling other device requirements, the ITRS foresees a transition from traditional planar Si MOSFET to Ultra-Thin-Body Fully Depleted devices in the near future, and to alternative device architectures, such as Fin Field Effect Transistors (FinFETs), at the 22 nm node and beyond [1]. The incorporation of materials with very high carrier mobility, such as Ge and III–V compounds, to substitute Si in the channel of advanced device architectures, is being considered for further technologies [1,28,29].

Ion implantation and thermal annealing are key steps to define dopant distribution and are expected to play an important role also in future technologies. Physical models that include appropriate parameter setting are required to describe all the mechanisms involved in these processes. Models for ion implantation should provide not only the spatial dopant distribution but also the generated defects. Description of amorphization and regrowth is also needed. Much attention should be given to the evolution of defects since they control the point defect superstaturation, which in turn affect dopant redistribution [12]. Interactions among defects and dopants must be modeled in detail as they greatly determine dopant diffusion and activation through the diffusion of mobile species and the formation and dissolution of various types of impurity clusters [11]. The presence of high stresses to enhance charge mobility [30] should be also considered in process simulation since it affects the equilibrium concentration of point defects, the effective dopant diffusivities and also the dopant solid solubilities [31–34]. Excimer laser annealing requires a complex modeling that includes the coupled simulation of the electromagnetic field, for the calculation of the heat source distribution, and the simulation of the thermal, phase and impurity fields, for the prediction of the material modification [35–37].

Over the last decades, a great effort has been made to quantitatively model the kinetics of these processes and to determine the parameters that govern the interactions in Si. Dedicated experiments and fundamental calculations have been performed to extract parameters. Detailed models are generally computationally too expensive in terms of memory and time. Empirical approaches and fitting parameters are sometimes used in computationally efficient models, although there is no guarantee of their validity outside the range of conditions where they have been fitted. Simplified models can be also extracted from the understanding of the most relevant mechanisms through a multi-scale approach or hierarchical scheme, in which more fundamental simulation techniques are used to extract physical parameters and mechanisms that are then implemented in less detailed models [38]. Continuum models continue being the mainstream in industry because they are fast and can be easily coupled to device simulators. Nevertheless, the reduction of device dimensions has revealed the power of atomistic techniques to provide the basis of simplified physical models implemented in continuum simulators and even to directly perform simulations of actual Si processing.

In this paper we review the most relevant models involved in the prediction of dopant distribution and activation, including the determination of the important parameters. Hierarchical simulation schemes, going from fundamental calculations to simplified models, are emphasized. This paper is organized as follows. In Section 2 we briefly review simulation techniques used in Si front-end processing, from continuum to atomistic methods. Section 3 is specifically devoted to the modeling of ion implantation. In Section 4 we center our attention on the properties and simulation of point and extended defects, while Section 5 is focused on the modeling of amorphization and recrystallization processes. Section 6 is devoted to the analysis and modeling of dopant-defect interactions. Some practical applications of front-end process modeling are presented in Section 7. Finally, in Section 8 we draw some conclusions and give future perspectives about this topic.

2 Simulation techniques

With further reduction of the devices feature size on each new technology generation, new effects or effects that were neglected so far become relevant and compromise the reliability of the manufacturing process. Their experimental characterization is a complex task, firstly because the realization of test lots results extremely expensive, and secondly because these effects usually occur simultaneously

which makes the interpretation of measurements very difficult. In this situation, the use of predictive process simulation techniques becomes almost imperative. The development of reliable physically based models is essential to predict at least the correct trends during technology development, where new process and materials are explored, and they have not been previously calibrated. Nevertheless, sometimes best models available may be too complicated or too slow when used in multidimensional continuum simulations. Simplified phenomenological models are often developed for design applications, where speed and accuracy are primary requirements, while predictability in uncalibrated regimes is secondary.

Modeling of the dopant and damage profiles resulting from ion implantation is the first step in front-end processing simulations. Different approaches can be followed for that purpose, and they will be described in more detail in Section 3.2. The resulting profiles are the input for other methods that describe the dynamics of the system.

2.1 Continuum methods

Most process simulators used in industrial applications are based on continuum methods, as it is the case of FLOOPS [39]. In this kind of simulators the physics of the system is formulated as a series of partial differential equations for each particle type considered to be relevant in the process [40,41]. Typically they are continuity equations. As an example, we will consider the interaction of two different particles, A and B, to form a mobile species, C: A+B↔C. The gain or loss of species C is formulated in terms of the normalized concentrations as in the following partial differential equation,

$$\frac{\partial\,[\mathtt{C}]}{\partial t} = K_f\,[\mathtt{A}]\,[\mathtt{B}] - K_b\,[\mathtt{C}] - \nabla(-D_C\nabla\,[\mathtt{C}]) \qquad (1)$$

where K_f and K_b are the forward and backward reaction rates, respectively, and D_C the diffusivity of species C. These parameters are related to the capture volume of interacting species, diffusivities of mobile species, stability of species formed, etc. They need to be explicitly defined in order to solve the equation.

In the simulation of Si front-end processing, a relatively high number of coupled partial differential equations have to be considered, since a lot of different interacting atomic species (dopants, intrinsic defects, defect clusters, dopant-defect complexes, impurities, etc.) are usually involved. The numerical solution of this set of partial differential equations requires spatial and temporal discretization to reduce the derivatives into algebraic differences. The problem is converted to a large, nonlinear system of coupled equations, which are solved using standard numerical methods. Usually some approximations, based on empirical fitting, have to be introduced in order to reduce the number of equations and decouple them.

Continuum simulators are fast and allow the consideration of big systems by adjusting the grid used for the spatial discretization. However, this advantage is reduced as the device size shrinks to nanometric scale. The atomistic nature of the material arises and complex physical interactions show up. The use of a very refined grid and the addition of more equations to include such new effects is computationally expensive, which slows down the resolution of the problem using continuum methods. Then atomistic simulation techniques become a good alternative even for industrial applications [42–45].

2.2 Kinetic Monte Carlo

The dynamics of the system can also be simulated from an atomistic point of view by the use of *Kinetic Monte Carlo* (KMC) techniques. This method allow the simulation of device structures at a macroscopic scale, providing an atomic description of the material and allowing a fast development of new models. KMC simulates the kinetics of defects and dopants by modeling their diffusion and interactions [11,46]. In non-lattice KMC models, atoms in the perfect lattice are not simulated, and consequently system sizes of hundreds of nanometers can be treated using average computers. The most popular non-lattice KMC code for front-end process modeling is DADOS [46].

In a KMC simulator, reactions such as A+B↔C are modeled by performing *interactions* (forward reaction) and *events* (reverse reaction). When particles A and B are within the capture volume of each other they interact leading to the formation of C. On the other hand, the probability of species C breaking-up is controlled by its event rate. Other type of events are, for example, diffusion hops of mobile species, or emission of point defects from clusters.

Both interactions and events are determined by several parameters (capture volumes, activation and migration energies, etc.) whose values must be defined a priori. All events simulated in KMC are thermally activated processes. The probability of exceeding an energy barrier, E_{act}, follows a Boltzmann distribution,

$$P \propto \exp\left(-\frac{E_{act}}{kT}\right) \qquad (2)$$

being T the temperature and k the Boltzmann constant. Therefore, the frequency (or probability per unit time) at which a particular event i takes place can be expressed as,

$$\nu^i = \frac{1}{\tau^i} = \nu_0^i \exp\left(\frac{-E^i_{act}}{k_B T}\right) \qquad (3)$$

where ν_0^i is the prefactor. In a system with N^i particles which can undergo the event i, the total event rate is

$$R = \sum N^i \nu^i. \qquad (4)$$

In Figure 1 we show a schematic of the simulation flow. In each simulation loop, a particular event and an atom are randomly selected according to the event frequency distribution. Then, the selected atom performs a jump in a random direction in order to simulate diffusion or emission of mobile species from clusters. If the moved atom

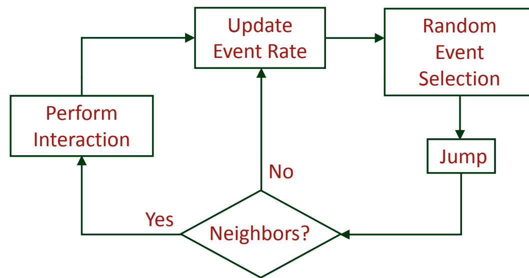

Fig. 1. Schematic of the simulation flow in KMC.

has neighbors to interact with in its new position, an interaction is performed. Event rates must be updated and the simulation time is increased by an amount $\triangle t = 1/R$. This loop is repeated millions of times in each simulation.

As the event frequency follows an exponential dependence there may be large variations between the rates associated to different events. The time-step $\triangle t$ is mostly determined by the fastest event. It may go from 10^{-9} s for some diffusing species, to 10^{-3} s, or even longer, for the emission of defects from stable clusters. Generally the fast events tend to disappear quickly leaving slower events that allow raising the time-step. This permits to easily access to macroscopic times, and thus to the simulation of actual processing conditions.

In KMC methods new reactions hardly add any computational load, since additional reactions only require new event rates to be added to the total event rate [47]. The main difficulty arises from the determination of the new parameters (binding energies, diffusivities, capture radius) that describe the interactions. These parameters are also necessary in continuum methods, but in this case new interactions imply a larger number of coupled equations which complicates their numerical resolution.

2.3 Fundamental atomistic methods

In order to simulate the dynamics of a system with KMC or continuum methods it is necessary to provide the values of the activation energies and prefactors for each one of the reactions that may take place. Only in a few cases these parameters can be obtained directly from experiments, due to the difficulty of extracting information at the atomic scale. Generally, this kind of information can be obtained from more fundamental atomistic simulation methods, where the system under study is treated as a set of interacting particles. Depending on the accuracy required to describe the particle interactions several techniques can be used, being each one able to reach different space and time scales. Once the particle interactions are defined, statical calculations (e.g. structure relaxations) or *Molecular Dynamics* (MD) simulations can be performed.

In the so-called *ab initio* methods, the interactions among particles are treated following the principles of quantum mechanics without introducing any parameter [48,49]. In these methods the Schrödinger equation has to be solved for the set of particles (nuclei and electrons) which constitute the system under study. Since, in general, it is not affordable to solve such a problem exactly, either analytically or numerically, it is necessary to find approximate solutions accurate enough to provide useful information. The first of such approximations, which was proposed in 1927 by Born and Oppenheimer [50], consists of a separation of the motion of the light and fast electrons from that of the slow nuclei. This allows to decouple the resolution of the equation for the nuclei, which can generally be treated classically, and for the electrons. The resolution of the Schrödinger equation for the electrons is still a formidable task, and further approximations have to be made. These approximations lead to different methodologies, the main ones being the *Hartree-Fock* methods [51–53] and the *Density Functional Theory* (DFT) [54,55].

Ab initio methods are computationally very expensive, specially if system dynamics is simulated, and thus they can only handle systems of a few hundred atoms and are limited to extremely short times, of the order of several femtosecons. Nevertheless, they give excellent insight into the underlying physics with no free parameters. For example, these methods have been used to study the energetics of point defects [56–59], to obtain an atomistic interpretation of Si self-diffusion in Si [48], to investigate dopant diffusion mechanisms [60–64] and the influence of charge states [62], and to analyze the formation and dissolution of dopant-defect complexes [65,66].

Another fundamental atomistic simulation technique is the *Tight Binding* (TB) method, where the crystalline electron wave function is developed as a linear combination of atomic orbitals [67–69]. Although TB is an exact theory that can be treated rigorously using quantum mechanics, for practical applications it is necessary to introduce certain approximations and eventually a fitting to experimental and *ab initio* data. This results in a semi-empirical technique whose accuracy and transferability depends on the chosen parametrization [70–73]. These simplifications allow in turn to simulate bigger systems (thousands of atoms) and longer times (of the order of picoseconds) with respect to those affordable by *ab initio* techniques. The TB method has been successfully used, for example, to analyze the formation, annihilation and migration mechanisms of native point defects in Si [69,74–79], to study the structure and energetics of small [80,81] and extended defect clusters [82–84], and to calculate the binding and formation energies of dopant-defect clusters in Si [85,86].

Some fundamental simulation studies require system sizes and time scales even larger than those affordable by TB methods. In these cases it is necessary to resort to atomistic simulation techniques with a lower computational cost. The computational overhead of previous techniques arises from the resolution of the Schrödinger equation to obtain the electronic description of the system. One possible simplification consists of sacrificing this electronic description and account for the effective influence of the electrons over the atoms through an analytical expression, called *empirical potential*. Empirical potentials must be

explicitly designed to properly describe the system under study. This implies choosing an adequate mathematical expression and a subsequent fitting process to a wide range of experimental results, *ab initio* and TB calculations. As in the case of semi-empirical TB methods, empirical potentials can only describe situations they have been designed for. If a new system is studied, a new parametrization or even a new mathematical expression must be developed, which is not an straightforward task (specially the latter case). Furthermore, no electronic structure information is obtained through them. Thus empirical potentials are not suitable for studying electronic properties or processes affected by charge states. The first potentials developed for Si, Stillinger-Weber and Tersoff, appeared in the mid eighties [87–90]. Since then, new potentials have been proposed in an attempt to improve the description of Si. Some are modifications of Stillinger-Weber [91,92] or Tersoff [93,94] original potentials, others are based on modifications of *embedded-atom* schemes typical of metals [95–97], and there are also new formulations such as the *environment-dependent interatomic potential* [98]. An extensive comparison of the results obtained with these potentials can be found in references [99–101].

With empirical potentials it is possible to run MD simulations with system sizes of several million atoms and to reach simulation times of about the nanosecond. For example, they have been used in Si for energetic and structural characterization of self-interstitials [102–105], vacancies [103–105], small interstitial clusters [106], as well as for studying self diffusion [102,105]. More complex situations, such as recrystallization of amorphous regions (*a*-regions) [101,107–109], structural transformations leading to planar {113} defects [110], and ion implantation [3,111–114], can also be simulated using empirical potentials.

2.4 Hierarchical scheme

As we have shown, each atomistic simulation technique gives information at a different scale level, sometimes complementary, so all of them have to be used in a *hierarchical* or *multi-scale* scheme to achieve full Si front-end processing simulation (see Fig. 2). Fundamental techniques such as *ab initio* and TB can be employed to study defect configurations and energetics, material and electronic properties, and to optimize empirical force potentials. MD simulations using empirical potentials can be used in turn to determine interaction and diffusion mechanisms involving defects, or to study the damage morphology obtained from individual implantation cascades as well as its annealing behavior. The parameters extracted from these detailed atomistic techniques, or even from experimental measurements, along with the mechanisms of defect interactions and diffusion, will define the relevant events to be considered in the KMC simulator.

Ion implantation models are used to generate dopant and defect distributions which are fed to the KMC simulator at time intervals determined by the dose-rate. During the inter-cascade time, defect diffusion and interaction

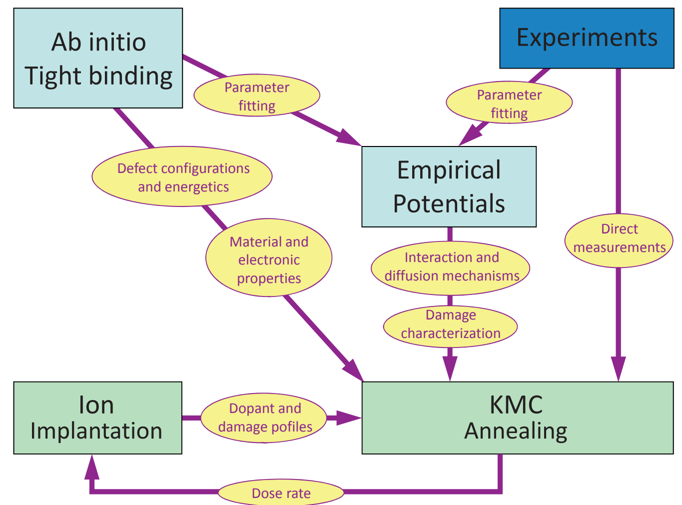

Fig. 2. Multi-scale hierarchical simulation scheme.

events occur at a rate that depends on the sample temperature, thus accounting for the dynamic anneal during the implantation process. This procedure is repeated until the specified dose is reached. Afterward, subsequent anneals can be simulated. It is worth to note that only the loop of implantation-annealing represents the actual front-end processing simulation, while the rest of techniques (fundamental simulation methods and experiments) are carried off-line.

3 Ion implantation modeling

Ion implantation is the technique preferred nowadays to fabricate junctions of devices since it is well established and provides a precise control of the distribution and concentration of the dopants in the Si substrate [2]. In this technique dopant atoms are first ionized, then accelerated through an electric field, and finally the resulting beam of ions is oriented toward the region to be doped. When the energetic ions penetrate into the substrate, they start to collide with its atoms until they come to rest. These collisions can produce permanent displacements of the substrate atoms from their perfect lattice positions. If the energy transferred to target atoms is high enough, they can initiate a subcascade leaving behind a vacancy and generating a Si interstitial where they stop, in addition to possible displacements during the subcascade. Furthermore, extensive damage regions can also be formed by the impact of heavy ions [3–5,111,115] and molecular implants [114,116–118]. During annealing treatments, the interactions of dopants with the excess of Is and Vs (generated during the implantation, or released by extended defects) can enhance dopant diffusion [8,119] and the formation of dopant clusters at concentrations much lower than their equilibrium solid solubility [120,121]. Therefore, for the fabrication of devices it is of critical importance not only to know the final dopant profiles, but also to quantify the amount and morphology of the damage since it will influence the final performance of the junctions.

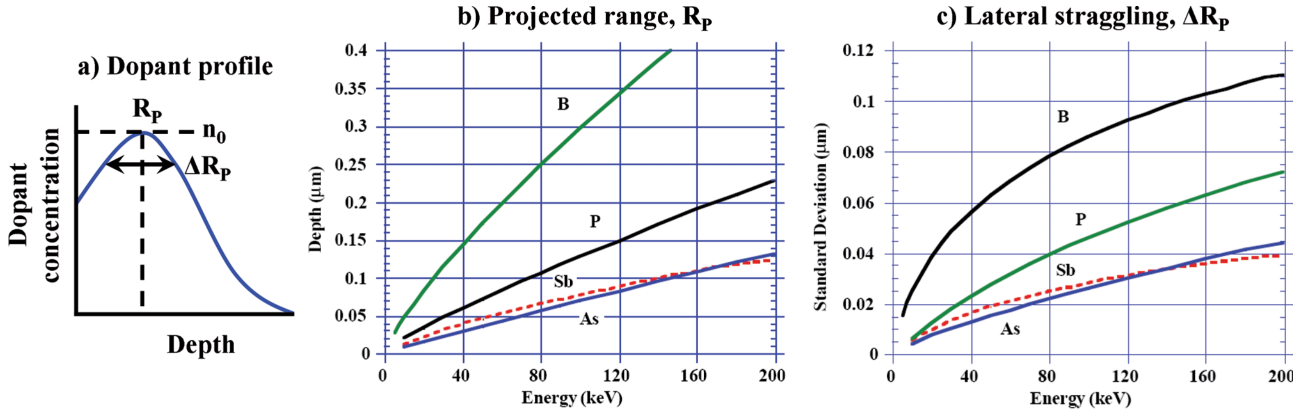

Fig. 3. (a) Schematic representation of a dopant profile, and variation of (b) R_P and (c) ΔR_P with implantation energy (from Ref. [122]).

3.1 Analytic distributions

For practical applications in the industry, it is convenient to obtain a fast estimation of dopant and damage profiles for different implant parameters (ion, energy, dose, ...) rather than carrying out test experiments or time consuming computational evaluations. Many analytic functions have been proposed to describe the final distribution of implanted dopants within the substrate. The simpler one is the Gaussian distribution given by

$$n(R) = n_0 \exp\left[-\frac{(R-R_P)^2}{2\Delta R_P^2}\right], \tag{5}$$

where n_0 is the distribution maximum, R_P is the projected range of the implanted ions, and ΔR_P is the longitudinal straggling, related to the width of the profile. In the case of a Gaussian distribution, R_P coincides with the depth of the maximum. These parameters determine the depth and abruptness of the junction, and depend on the implanted ion and its energy, as represented in Figure 3.

Gaussian distributions only provide an adequate fit to profiles around the projected range. The Pearson-IV distribution [123,124] accounts for the asymmetry and sharpness of the dopant profiles by considering two more new parameters, the *skewness* and the *kurtosis*. Pearson IV distributions are especially appropriate to describe dopant profiles in amorphous or amorphized materials. For crystalline materials, there are other alternatives, such as joining half Gaussian or Pearson IV functions with an exponential tail [125], or double-Pearson IV functions [126,127].

Analytic distributions allow a fast and accurate description of dopant profiles without statistical noise. They are frequently used as the input for continuum simulators. Nevertheless, it is necessary to calibrate the parameters involved for each set of implantation conditions (ion type, energy, incident angle ...). Thus, they cannot be used to predict the dopant profiles for implantations that have not being previously tabulated.

3.2 Binary collision approximation

The *Binary Collision Approximation* (BCA), on the basis of the Monte Carlo method, is used to describe individual collisions during an implant cascade. The basic idea of BCA is that the moving ion only interacts with its closest target atom through a repulsive pair potential $V(r)$ (being r the distance between them). The resulting collision can be numerically solved by considering the momentum and energy conservation laws of classical mechanics [128–130] to evaluate the energy transferred to the target atom, which constitutes the elastic energy losses of the ion.

In the BCA description of cascade evolution, a target atom is displaced from its lattice position when its energy after the collision with a moving atom exceeds the *displacement energy threshold*, E_d [129]. For Si, experimental and theoretical estimations for this energy range from 10 to 30 eV [131–135], but for most BCA simulators it is conventionally taken as 15 eV [136–138]. For energy transfers above E_d, the target atom can create a subcascade, but for energy transfers below E_d it is not displaced and the energy is assumed to be lost to phonons. A moving atom is considered to stop when its kinetic energy falls below a certain value, in the order of E_d, since it will not be able to permanently displace more atoms through collision events [129].

Several aspects need to be considered to physically model the collisions. Both the projectile and the target atom are under the influence of a repulsive potential $V(r)$. Accurate potentials for the colliding atoms can be obtained from *ab initio* calculations [139]. Nevertheless, universal functional forms are usually considered in order to have a wider range of application. They are defined as a screened Coulomb potential

$$V(r) = \frac{Z_P Z_T e^2}{4\pi\varepsilon_0 r}\Phi(r), \tag{6}$$

where Z_P and Z_T are the atomic numbers of the ion and the target, respectively, ε_0 is the vacuum permittivity, and $\Phi(r)$ is the screening function which takes into account

that the inner electrons shield some of the nuclear charge by reducing the repulsive Coulomb potential [130]. By modeling the electronic density of the atoms and analyzing the repulsive interaction for many different pairs of atoms, several screening functions have been obtained, such as Tomas-Fermi [140], Molière [141], Lenz-Jensen [142], and Ziegler-Biersak-Littmark (ZBL) [143]. Among them, the most used is probably the last one.

In addition to nuclear collisions, ions also interact with the electrons of the target, causing the so-called *inelastic energy losses*. Traditionally, both elastic and inelastic energy losses are treated separately, which simplifies considerably the analysis of the collisions. In the typical irradiation conditions during implantation in actual MOSFET fabrication, S/D extensions are generated through implants with an energy that may vary between 300 eV and 30 keV, and a dose in the range of 5×10^{13}–2×10^{15} cm^2 [144]. For these conditions, only elastic collisions are considered as responsible for damage generation during ion implantation, while electronic interactions diminish the energy of moving ions [130]. Damage produced via electron-phonon interactions in Si has been observed only for molecular implants and deposited energies above 28 keV/nm, which corresponds to implant energies of the order of MeV [145].

The inelastic energy losses are usually divided into two contributions. One arises from a *local* inelastic stopping power as a consequence of the momentum transfer between the electrons of the projectile and those of target atoms during collisions. The other one is associated to a *non-local* electronic stopping power since moving ions (charged particles) travel between consecutive collisions within a medium with electrons. The first contribution is commonly evaluated using the Firsov's model [146,147], which considers a viscous force derived from a velocity dependent potential acting on the particles during the collision. For the second contribution, the classical non-local model of Lindhard, Scharff and Schiott assumes that the energy losses due to electronic stopping are proportional to the ion velocity [148,149]. The Brandt-Kitagawa model [150] is also commonly used, in which the inelastic energy losses of a proton moving with the same velocity as the ion are evaluated. These results are scaled taking into account the effective charge of the ion due to its degree of ionization (which in general is a function of ion velocity and the charge density of the target). Subsequent modifications [151,152] resulted in a model with only one adjustable parameter for each implant species, related to the effective electron density of the target, depending on the ion-target combination. This model has been used both in BCA simulators [138,151] and in MD with empirical potentials [151–153].

All these physical models provide BCA simulations with great capability for simulating almost any implantation condition without additional calibrations. A detailed atomistic description of the whole cascade is obtained by following the trajectories of the implanted ion and of the generated recoils ('*full cascade*' BCA). The result of the simulation of the implantation cascade is the position of the implanted ion and the generated Is and Vs, called *Frenkel pairs* (FPs), which can be the input for KMC codes [154–156]. As an example, the position of the ion and the FPs generated by typical 1 keV B, Si and Ge cascades into Si simulated with BCA are represented in Figure 4. This approach adequately reproduces the dilute damage generated by light ions. However, it is not able to reproduce more complex damage structures such as amorphous pockets (*a*-pockets), which have been observed experimentally after heavy ion implantation [4,115,157].

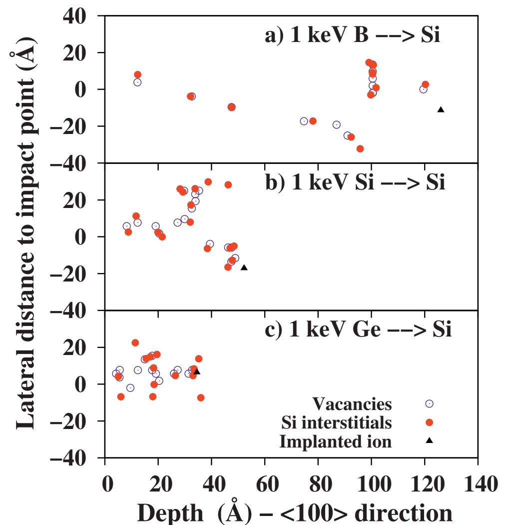

Fig. 4. Atomistic description of 1 keV of (a) B, (b) Si, and (c) Ge into Si provided by a typical 'full cascade' BCA simulation.

In order to accelerate the calculations, instead of simulating all the recoils, BCA simulators may follow only the trajectory of the implanted ion. Within this approach, damage is calculated according to the modified Kinchin-Pease (KP) formula [158]. When a certain amount of energy E_{dep} is deposited within a given target volume, the number n of displaced atoms generated is

$$n = 0.42\frac{E_{dep}}{E_d}. \quad (7)$$

Nevertheless, not all the generated defects may effectively contribute to increase the damage because some of them may recombine rapidly or may correspond to atoms previously displaced. Thus, the net increase of point defects after recombination, Δn, is given by

$$\Delta n = f_{surv}\ n\left(1 - \frac{N}{N_{sat}}\right), \quad (8)$$

where N is the previous local defect density in the region where energy is deposited, N_{sat} is the local defect density necessary to reach amorphization, and f_{surv} is the fraction of point defects surviving recombination within one recoil cascade [159,160], or surviving both intracascade and intercascade recombinations [138,161]. This parameter depends on implant conditions (temperature, dose, implant energy, etc.) so that the model can account for

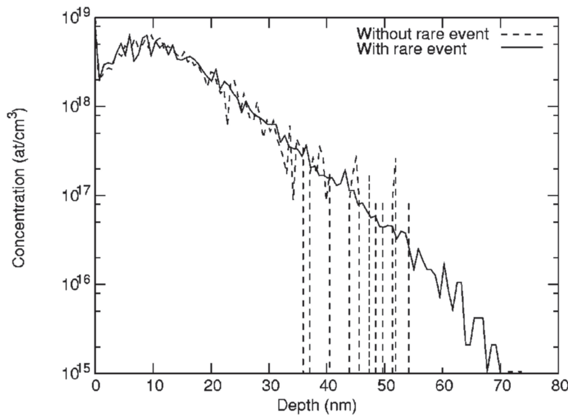

Fig. 5. Comparison of profiles of a 2 keV B implantation into (100)Si (tilt = 7°, rotation = 30°), simulated with 2000 ions with and without using rare event algorithms (from Ref. [138]).

dynamic annealing [162]. When implanting ions in a crystalline target, damage generated by previous ions can accumulate and the position of target atoms may differ from those of a perfect crystal. In order to account for the damage accumulation effect, the degree of amorphization of a region, N/N_{sat}, is used to define a probability (i) to displace the target atoms randomly from their position [159,160], (ii) to perform a random rotation of the crystal lattice [138], (iii) for the ion to collide with a target atom of the considered volume [161]. In any case, the effect of the accumulated damage can be regarded as the gradual transition from crystal to amorphous in the considered volume, which is also reflected in a gradual transition in the number of scattering events suffered by the ions. When N reaches N_{sat} within a given volume, the lattice is assumed to transform into the amorphous state and the target positions turn random.

Within this approach, ion profiles are rapidly evaluated and in good agreement with experiments, but at the expense of losing the atomic description of damage. The depth distribution of dopants and defects is obtained by simulating a large number of implant cascades. To reduce the statistical noise of the dopant profiles, specially relevant in the tails, several algorithms, called *rare event algorithms*, are used [138,153,163,164]. These algorithms consist of splitting the ion trajectory at certain points, which are assigned a statistical weight to the overall profile, depending on the number of times that the original trajectory was divided. As an example, dopant profiles obtained with a BCA simulation of low energy B implants into Si are represented in Figure 5.

There are different codes available that implement the BCA approximation for simulating ion implantation. In 1974 Robinson and co-workers developed one of the first atomistic BCA simulators, known as MARLOWE [129], in which the target material is considered to be crystalline. A different simulation scheme was followed in 1985 by Ziegler, Biersack and Littmark for their BCA simulator, TRIM [143], in which an amorphous target is considered rather than crystalline, and the projectile trajectory is statistically followed by randomly selecting a target atom, an impact parameter and a distance (mean free path). This model works well for amorphous targets, but it can not be employed for crystalline ones. In order to overcome this limitation, a combination of both MARLOWE and TRIM, known as CRYSTAL-TRIM [165], was developed. Other BCA simulators, such as IMSIL [159,160], UT-MARLOWE [137], UVA-MARLOWE [166,167] and IIS [138]) allow choosing between crystalline and amorphous targets.

3.3 Classical molecular dynamics

MD calculations with empirical potentials, usually known as Classical MD simulations (CMD), can also be used to model implantation cascades. For that purpose the atom to be implanted is set in motion toward the substrate with the desired energy and angle. The substrate consists of a simulation cell with a free surface with the appropriate orientation in the direction of the implantation, while periodic boundary conditions are commonly applied on the other spatial directions. This simulation cell must be big enough to encompass the full cascade evolution avoiding the self interaction due to periodic boundary conditions. Its final dimensions depend on both the mass of the ion considered and on its energy: lighter ions and high energies result in deeper projected ranges. For instance, Caturla et al. used simulation cells with $\sim 10^6$ atoms for simulating 3 keV B and 15 keV As cascades into Si, which entails a huge computational cost [3].

Empirical potentials employed in CMD to describe the atomic interactions are originally fitted to account for the equilibrium properties of the materials they model. Nevertheless, during the cascade evolution high energy collisions occur, and they must be properly described as well. For this purpose, a spline at short distances to repulsive pair potentials, such as Molière [141] or ZBL [143], is done [168]. In addition, the interaction of the ion with the electrons of the target is not considered within empirical potentials, and it is necessary to model it to account for the associated energy losses. In a simple approximation, the effect of the electrons can be regarded as a velocity dependent frictional force that arises from the movement of a charged particle in a material with an homogeneous electron density [3,112,169]. Nevertheless, more sophisticated electronic stopping models developed for BCA can also be implemented in CMD simulations [151–153].

CMD simulations of monatomic ion implantation reveal that light ions generate dilute damage in the form of isolated FPs or small defect clusters similar to the description provided by BCA [3,5]. However, heavier ions can also generate bigger defect clusters and a-pockets [3,5] whose description is not appropriately captured by traditional BCA models. A detailed analysis of the energy deposition conditions indicates that a-regions are generated directly from a cascade in a melting-like process [111,170], and they have a deficit of atoms while the surrounding regions contain isolated Si interstitials or small interstitial clusters [5,112].

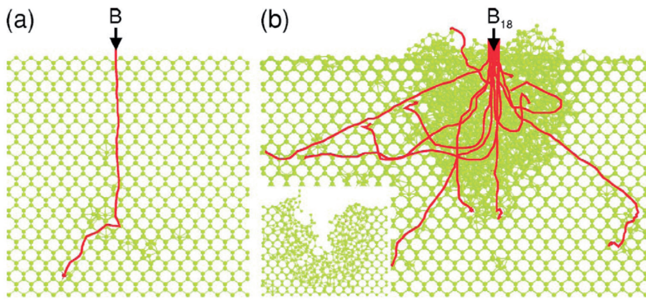

Fig. 6. Lateral snapshots showing the typical damage configurations obtained after (a) monatomic B and (b) B_{18} cluster implantations with 500 eV per B ion in both cases. Solid lines indicate B atom trajectories. Inset in (b) is a 12-Å-thick slice taken around the cluster impact point showing the generated crater (from Ref. [114]).

Cluster and molecular implantations have been studied using CMD simulations [114,116–118,171–173]. These type of implantations are of interest for surface modification processes (such as sputtering, surface smoothing and cluster ion assisted thin film deposition), and for the fabrication of ultra shallow junctions since they allow accessing to lower effective implant energies and are self-amorphizing [174,175]. CMD simulations have provided a relationship between the cluster size and the implant energy to maximize the surface sputtering or to achieve cluster deposition without sputtering [171]. They have also been used to characterize the damage generated by cluster impacts [114,118]. A comparison of the generated damage for monatomic B and B_{18} cluster implants with the same energy per implanted ion is shown in Figure 6. The average number of atoms disordered by each monatomic B cascade is 32, while for the B_{18} cascade, each B atom disorders 108 atoms. This is is a consequence of the different damage generation mechanisms present in each case. For monatomic B implants ballistic collisions dominate and mainly isolated point defects and small defect clusters are generated. For the cluster implantation a high local energy deposition at the impact point causes the melting of the substrate and its subsequent amorphization by quenching [114,116].

3.4 Linking BCA and CMD

Despite the good description of generated damage by implant cascades obtained with CMD simulations, the high computational cost of this technique limits its use to the study of individual cascades rather than a full implantation process (i.e. thousand of cascades on the same target with dynamic annealing during the intercascade time interval). Most efforts made in the past to accelerate CMD calculations [153,169,176–178] were about evaluating forces not on all the atoms of the simulation cell but only on those atoms that (i) interact with the ion [153,169], (ii) are under strong forces [177], (iii) are set in motion during the cascade [176], or (iv) fulfill some energetic criterion [178]. However, either the introduced approximations were at the expense of lacking a correct description of lattice damage, or the computational time reduction was not enough to replace BCA with CMD for the simulation of the full implantation in process simulators.

Another alternative is the use of multi-scale modeling, where several simulation techniques are applied at different time and size scales. One of the approaches uses BCA to simulate the evolution of high-energy atoms and, when their energy is lower than a certain threshold (500 eV [179] or 100 eV [180]), CMD is used to simulate the final part of the cascade. However, in this approach the most time-consuming stage of the cascade is still simulated with CMD, which implies a low computational gain factor.

Other approach consists of using CMD simulations for the evaluation and characterization of the damage generated under different energetic conditions. The information extracted from these studies is then fed to BCA simulators by means of improved damage generation models with appropriate parameters [180–184]. In addition to the FPs generated by the ballistic mechanism for energies transferred above E_d, Hobler et al. [181–183] and Santos et al. [184] simulated the generation of a-regions with BCA by accounting for the energy transfers below E_d that occur during the cascade evolution. From CMD simulations it was determined that the final size of an a-region depends on the total energy deposited [181] and also on the deposited energy density [170], and its generation is the result of the competition between the melting of the lattice and the energy out-diffusion [170]. In Hobler's model, to generate the damage by the melting mechanism, the heat diffusion equation together with a melting criterion is solved by using finite differences with a grid of points coincident with the crystallographic lattice sites [182]. They also included a lattice collapse model, which requires a minimum density of melted atoms to convert a region into amorphous [183]. In Santos' approach, an analytical expression similar to the modified KP formula was obtained [184]. The final number of additional disordered atoms as a function of the initial energy deposition conditions, N_{DA}, is given by

$$N_{DA} = \frac{N\rho - NE_T(N)}{D_C(N)}, \tag{9}$$

where ρ is the initial energy density (in eV/atom), and N is the initial number of atoms that receive energy below the displacement threshold. $E_T(N)$ and $D_C(N)$ are the *threshold energy density* for damage production and the *damage generation cost*, respectively. Unlike the modified KP formula where E_d is constant, in Santos' model both E_T and D_C vary with N, accounting for the non linear effects that appear in molecular implants. This model has been implemented in a BCA code and successfully used to simulate molecular implantations [184], as shown in Figure 7 for a B_{18} cascade.

4 Point and extended defects

Native point defects in Si have been an important field of both theoretical and experimental research for several

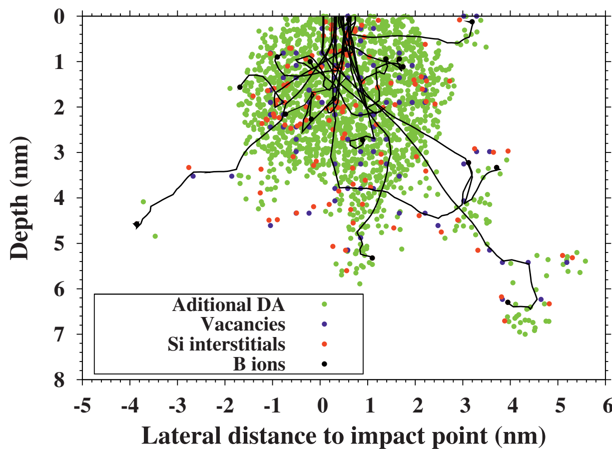

Fig. 7. Depth projection of damage generated by a B_{18} cascade obtained with the improved BCA. A conventional BCA code only provides the position of the FPs generated by the B ions. The improved damage model adds the disordered atoms generated through multiple interactions, which constitute the main volume of the *a*-region and can not be obtained only by the superposition of individual cascades. The dimensions of the obtained *a*-region are in good agreement with the results of CMD simulations (see Fig. 6).

decades. The interest in its study continues today due to their role in a large variety of phenomena, especially in those related to the fabrication of ICs. Native Si defects affect the microstructure evolution of the material during several of the manufacturing steps, and thus can alter the final performance of the device [185]. The most fundamental building blocks for microdefect formation in crystalline Si are the self-interstitial and the vacancy. These two species are the mediators for impurity diffusion and clustering [185,186].

Point defects interact among them giving rise to aggregates or clusters [187–189]. Generally, the formation energy of such clusters decreases with size, and consequently their population in the Si lattice is controlled by an Ostwald ripening process: larger clusters grow at the expense of point defects freed from smaller and less stable agglomerates [12,190]. The study of the properties of small clusters is difficult because they are too small to be visible in Transmission Electron Microscopy (TEM) images. Moreover, they show a great variety in their atomic configurations which complicates their analysis using simulation techniques. At sizes of several hundred point defects these aggregates start becoming visible in TEM; they usually show regular atomic structures, and are generally known as *extended defects* [191]. Understanding their behavior and properties is important in order to develop predictive atomistic simulators for the design of new IC generations [154].

4.1 Vacancy defects

The vacancy is the simplest intrinsic point defect in Si: its basic form is just a missing Si atom in an otherwise tetrahedrally coordinated lattice [192]. While at cryogenic temperatures the vacancy shows an Electron Paramagnetic Resonance (EPR) signal [193], at processing temperatures they are not directly detectable due to their high mobility, and so their association with phenomena at such temperatures is not straightforward [194]. The formation energy of the vacancy has been estimated using both theory and experiment. There is considerable uncertainty in the actual value, with various experimental estimates lying in the range of 2 to 4 eV [193,195,196]. Using *ab initio* techniques, calculated formation energies for the vacancy range from 3 to 6 eV (see Ref. [192] and references therein). The theoretical difficulties arising for the vacancy are related, at least in part, to the subtle reconstruction of the dangling bonds, where some controversy still remains [197,198]. The diffusivity of vacancies has been characterized experimentally by various methods: at low temperatures directly by EPR, and at high temperatures indirectly via their effect on the diffusion of dopants and metals. While vacancy migration energies determined experimentally range from 0.3 to 4 eV, *ab initio* calculations predict values in the lower end, between 0.3 and 0.4 eV [192].

Vacancy aggregation in Si has been studied extensively because large vacancy clusters (voids) are known to be harmful to microelectronic device yield and reliability, particularly gate-oxide integrity [199,200]. However, the introduction of voids in the Si lattice has been proposed as a way to reduce the interstitial supersaturation [201–204]. This controlled injection of voids, part of a more generic concept of *defect engineering*, allows the reduction of the anomalous diffusion of dopants such as B. Positron annihilation experiments have been used to determine the lifetime of vacancy clusters, being around 400 ps for sizes between V_3 and V_{10} [192]. Voids are much more stable, and have been observed directly by TEM to organize into octahedral structures aligned almost exclusively along the {111} crystallographic planes of the Si lattice [205]. This phenomenon has been explained by the low energy of the Si(111) surface relative to other orientations [206]. The thermodynamics and binding properties of these vacancy clusters have been studied using quantum and classical simulation techniques [194,207–209]. In particular, for small vacancy clusters it has been found that certain sizes show greater stability, as it is the case of the V_6, V_8 and V_{12} clusters (see Fig. 8), due to particular bond reconstructions in the Si lattice [207,209–211]. For larger sizes, binding energies tend to a value of around 3 eV, in agreement with Sb diffusion and Au labeling experiments [212,213].

4.2 Interstitial defects

The self-interstitial, one extra Si atom in the crystal lattice, is the natural counterpart of the vacancy. The study of the Si self-interstitial properties is of particular importance in Si processing. Self-interstitials have been implicated as the origin of rodlike defects observed in Czochralsky single-crystal growth, which can ultimately produce

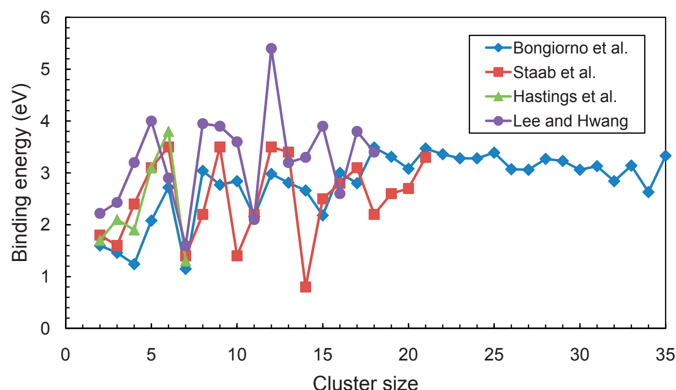

Fig. 8. Binding energy for vacancy clusters as a function of cluster size (from Refs. [207,209–211]).

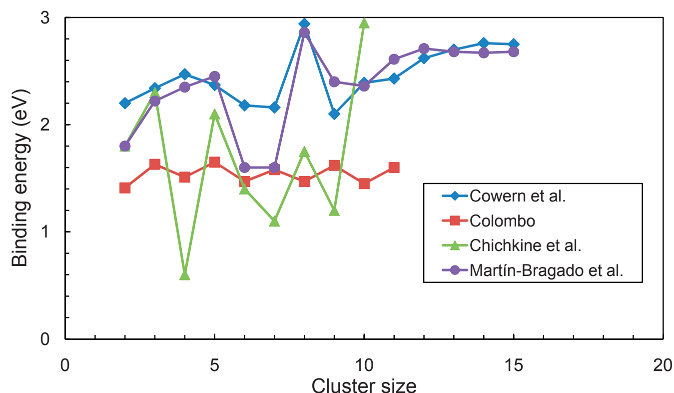

Fig. 9. Binding energy for interstitial clusters as a function of cluster size (from Refs. [12,231–233]).

the degradation of the manufactured Si devices [214]. On the other hand, during the implantation step a large concentration of excess interstitials is introduced in the lattice. They interact with dopants and cause the so-called *Transient-Enhanced Diffusion* (TED) which alters the junction depth [215].

Due to its importance in Si processing, a great number of theoretical studies have been devoted to determine the configuration and energetics of the Si self-interstitial, as well as its diffusive behavior. These include *ab initio* [48,56,58,64,216–220], TB [74,76–80,221], and empirical potential calculations [104,107,222–230]. However, even when using the same calculation techniques, different authors come to different conclusions regarding the Si self-interstitial properties. The discrepancies are mainly related to the determination of the lowest formation energy configuration and to the microscopic description of the interstitial-mediated diffusion mechanism. At least four different interstitial configurations have been identified: tetrahedral (T), dumbbell (D), hexagonal (H) and extended (E). Within the first-principle framework, most authors coincide that the lowest energy configuration is the D interstitial, with 2.2–3.4 eV [48,56,58,64], while Leung et al. determine that the lowest energy correspond to the H interstitial with 4.8 eV [219], and Needs states that D and H are degenerated configurations having both a formation energy of 3.3 eV [220]. In the case of TB simulations, some authors claim that the lowest formation energy configuration is the D interstitial with 3.8–5.6 eV [74,76], while others suggest it is the T configuration with formation energies between 3.8 and 4.4 eV [77,78,221]. When using empirical potentials the diversity in results is even higher [222,223,225,227–230]. There is not a clear agreement either regarding the microscopic description of interstitial-mediated diffusion, where very different diffusion mechanisms have been proposed, with migration energies ranging from 0.1 to 1.9 eV (see Ref. [192] and references therein). In spite of such a diversity of results, recently Marqués et al. demonstrated using CMD techniques that all self-interstitial configurations coexist in Si but with different concentrations, and diffusion occurs through transitions among them [102]. The macroscopic behavior for self-interstitial diffusion can be modeled by a simple description based on a unique interstitial species with an effective formation energy of 3.8 eV and a migration barrier of 0.8 eV, in very good agreement with experiments [12,196]. The exact numbers do not correspond to any of the particular interstitial configurations or diffusion mechanisms, but are the result of the *averaged* behavior of all of them. These findings help to explain why it is not straightforward to justify the experimental measurements on interstitial diffusion, related to the macroscopic behavior, resorting to a particular interstitial configuration and diffusion path theoretically determined using *ab initio* or TB techniques.

Due to their implications in Si technology, self-interstitial aggregation in Si has attracted much attention in the literature. Large interstitial clusters formed after implantation act as a reservoir of Si self-interstitials that are slowly released during subsequent thermal treatments causing the TED of interstitial-diffusing dopants such as B [8]. Moreover, interstitial extended defects show photoluminiscent signals [234], and have been proposed to fabricate optical emitters compatible with the standard and well-established IC technology. They introduce local strain fields in the Si lattice, which modify the band structure and provide spatial confinement of the charge carriers allowing room-temperature electroluminescence [235].

From B diffusion experiments, Cowern et al. deducted the formation energy of small interstitial clusters using the concept of Ostwald ripening and the fact that the Si interstitial supersaturation, and therefore B diffusion, is related to their stability [12]. Results for the binding energy of such clusters are shown in Figure 9, along with calculations carried out by other authors using *ab initio* [232], TB [231] and fitting to experiments [233]. The most important finding is that oscillations of the binding energies occur for small, discrete, "magic" sizes (as with vacancies). These more stable sizes correspond to configurations where atoms remain four-fold coordinated [236]. For larger sizes, of around one hundred atoms, {113} defects start to form. Their atomic structure was determined by Takeda using TEM [237]. {113} defects consist of large interstitial chains along the ⟨110⟩ direction, packed together along the {113} plane, which gives this defect its name. It has been experimentally shown that {113}

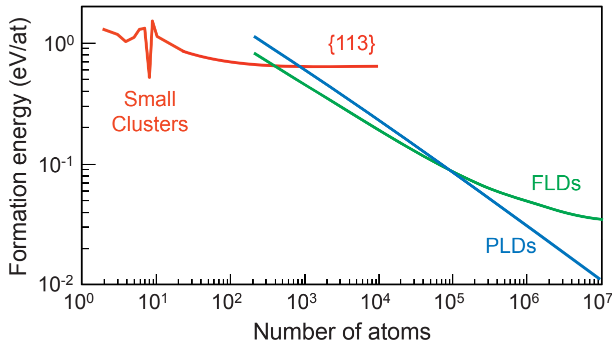

Fig. 10. Formation energy of the different types of interstitial agglomerates as a function of size (from Ref. [238]).

defects grow in length along the ⟨110⟩ direction [191]. In the process, their formation energy decreases from 0.8 to 0.65 eV [238]. Apart from the experimental characterization of these extended defects, many theoretical investigations on their structure, energetics and induced strain fields have been published [82–84,110,239,240]. If {113} defects grow up to a certain size, they can transform into dislocation loops, perfect (PDLs) and faulted (FDLs) [241]. This transformation has been proposed to be due to some unfaulting reactions, as it has been shown recently by using *ab initio* simulation techniques [242]. The formation energy of FDLs tends to 0.027 eV with increasing size, while it tends to 0 for PDLs [238]. In Figure 10 we show the formation energy of interstitial agglomerates as a function of size. This energy landscape determines the microstructural evolution of the material. For example, at a size of 1000 interstitials, a {113} would act as a sink for self-interstitials released by PDLs and as a source of self-interstitials for FDLs.

4.3 KMC and continuum modeling of defect evolution

The modeling of defect evolution is key to determine the annealing required to completely remove the damage and for an adequate prediction of dopant profiles. Although some calculations suggest that small clusters (di-interstitials, tri-interstitials, etc.) may be mobile [233,243], most models only consider Si interstitials and vacancies as the diffusing species. Therefore, the reactions that account for the interactions among defects leading to the formation of agglomerates of n Si interstitials (I_n) or vacancies (V_n) are:

$$I + V \longleftrightarrow 0 \quad (10)$$

$$I_n + I \longleftrightarrow I_{n+1} \quad (11)$$

$$V_n + V \longleftrightarrow V_{n+1} \quad (12)$$

$$I_n + V \longleftrightarrow I_{n-1} \quad (13)$$

$$V_n + I \longleftrightarrow V_{n-1}. \quad (14)$$

Since defect size may extend to large numbers, a huge set of reactions should be modeled ($n = 1 \rightarrow \infty$). Atomistic KMC simulators can track each and every of the generated Is and Vs and the different cluster sizes. The key parameters for these reactions are the point defect diffusivities

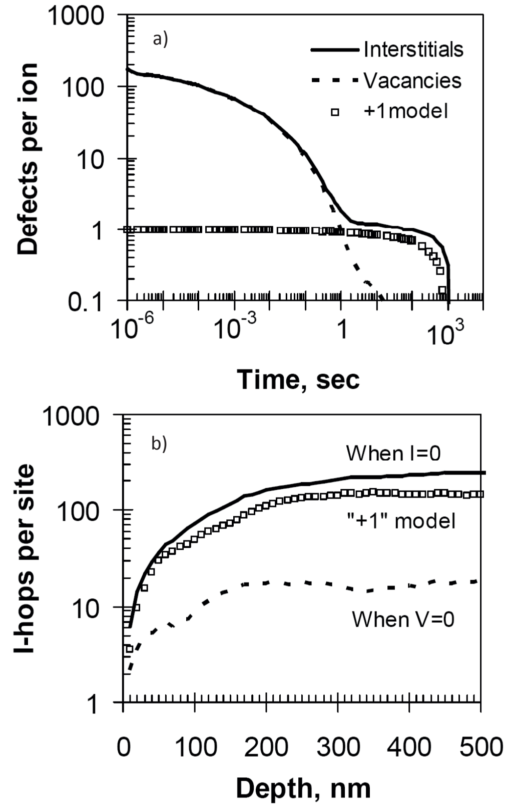

Fig. 11. KMC simulations of the time evolution of (a) the total number of Si self-interstitials and vacancies, and (b) the number of interstitial hops, for a 150 keV Si implant to a dose of 7×10^{13} cm^{-2}, annealed at 800 °C (from Ref. [254]).

and the capture and emission probabilities, which are dependent on defect stability (binding energy). For small clusters magic numbers are used [12], while for extended defects generally analytical expressions relate the binding energy to defect size [244,245]. In continuum simulators, a large number of equations derived from reactions (10) to (14) for $n = 1 \rightarrow \infty$ is prohibitive due to the high computational cost. Simplified models have been developed with the aim of reducing the number of equations to be solved [246–253].

KMC simulations show that most FPs quickly recombine during the implant itself and the initial stages of the annealing. However, when implanted ions become substitutional they generate excess Si interstitials that have no vacancies to recombine with, and survive for a long time until they are annihilated at the surface. This is evidenced in Figure 11a, which shows the number of generated defects per implanted ion as obtained from KMC simulations. After 1 s, almost all vacancies have recombined, but the excess Si self-interstitials remain several minutes. As can be observed in Figure 11b, the number of interstitial hops per lattice site (which is proportional to the interstitial supersaturation) after vacancy recombination ($V = 0$) is minimal compared to the I-hops after interstitial annihilation ($I = 0$). This proves that dopant diffusion and deactivation is mainly driven by the excess Si interstitials remaining after FP recombination. Based on

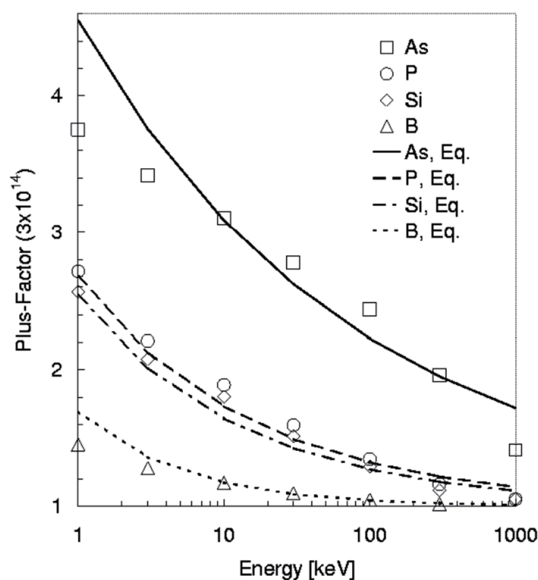

Fig. 12. Energy dependence of the plus factor for different species implanted with a dose of 3×10^{14} cm^{-2}. Symbols represent numerical data whereas lines correspond to an analytical fitting (from Ref. [253]).

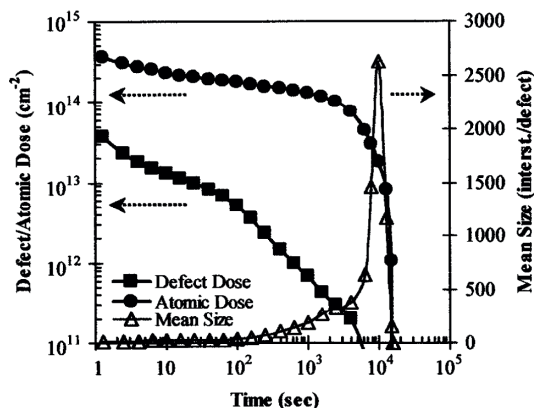

Fig. 13. Simulated time evolution during annealing at 750 °C of the atomic and defect dose of Si interstitials in defects for a simulated 40 keV Si implant to a dose of 10^{14} ions/cm^2. The time evolution of the mean size of the defects is also plotted (from Ref. [260]).

this observation, it is usually assumed that the amount of residual damage after implant is approximately the implanted dose (each ion contributes as one excess Si interstitial), which is known as the "+*1* model" [252]. This simple model provides similar results than full-cascade simulations (see Fig. 11).

The "+*1* model" relies on an efficient FP recombination and it is valid for light ions implanted at medium energies and doses. For heavy ions [255], low doses or high implant temperatures [256], FP recombination is not so efficient, and generated Si interstitials and vacancies may significantly contribute to dopant diffusion before their recombination. In this case, the "+*1* model" underestimates the amount of effective Si interstitials. For this reason, an *effective plus factor* or "$+n$" was defined to take into account the effect of implant parameters [253,255,257]. The "$+n$ model" determines the effective number of excess Si interstitials ("n") per implanted ion according to the ion mass, implant energy and dose. Figure 12 shows the $+n$ factors for several ion species and implant energies.

The "$+n$ model" allows to reduce the number of interactions to consider by neglecting the role of vacancies (Eqs. (10), (12) and (14) can be omitted) and reducing the number of interstitials to "$+n$". It provides good results for dopant diffusion and defect evolution at a macroscopic scale. However, some dopants undergo clustering during the implant or the initial stages of the annealing, before significant $I - V$ recombination has occurred. In these cases, dopant deactivation may be underestimated if the initial high interstitial and vacancy concentrations are not simulated [258].

The surface plays an important role on defect evolution. Its efficiency as a sink for point defects is modeled through the recombination probability (in KMC models) or the recombination length (in continuum simulators) [259]. Although the exact values of these parameters are not known, it is generally assumed that the probability of a defect that approaches the surface being annihilated is close to unity. After vacancy recombination, the surface is the only sink for excess interstitials. Initially, when there are many small defects, free Si self-interstitials are more likely to be captured by a defect than to reach the surface. Ostwald ripening takes place, leading to the growth of bigger defects at the expense of the smaller ones. As a result, defects increase their size but the total number of defects is reduced (see Fig. 13). When the separation among them is comparable to the distance to the surface, similar probabilities exist for an interstitial to reach the surface or to be trapped by a defect, and defects quickly dissolve [260].

The "$+n$ model" serves as a starting point in continuum models, but additional simplifications need to be done because interstitial defect evolution would require a set of differential equations, each equation describing the time evolution of a defect size ($n \to \infty$). Some models consider all clusters sizes, from small clusters of a few interstitials to defects with hundred of particles, but are computationally too expensive [12,261,262]. Several works have proposed reduced models with only a few equations to describe small interstitial clusters, without sacrificing accuracy [246–249]. Cowern et al. showed that small clusters should not be neglected, because they act as precursors of {113} defects and control the Si interstitial supersaturation at the early stages of the annealing [12]. A simple model considering a stable cluster (I_3) and two adjacent less stable clusters (I_2, I_4), has been proved to correctly reproduce the contribution of small interstitial clusters to TED [246].

The biggest effort in defect modeling has been devoted to {113} defects, since they have been identified as the main source of interstitials for TED [8]. As the binding energy of {113} defects is a smooth function of defect size [261], moment-based models can be used, in which

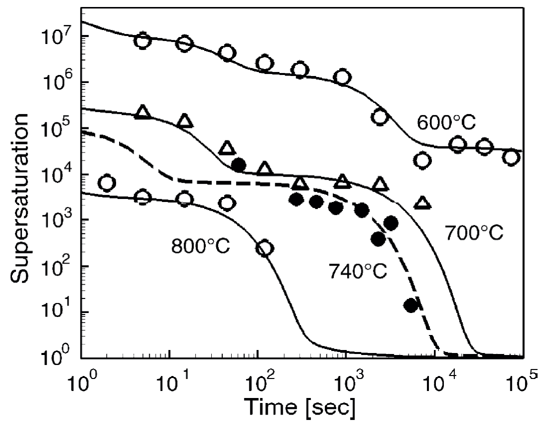

Fig. 14. Measured (symbols) and simulated (lines) interstitial supersaturation after 40 keV Si implantation (from Ref. [246]).

the cluster equations are replaced by differential equations for the moments of the cluster distribution [248]. The first proposed model only considered the concentration of interstitials trapped in clusters (first moment of the cluster distribution), neglecting the effects related to cluster growth [263]. Improved models do include these effects by considering not only the concentration of interstitials in {113} defects (C_{113}), but also their density (D_{113}), by means of two [244,246,247,250] or even three moments [248].

In a two-moments approach, the concentration of interstitials in {113} defects increases when the biggest cluster considered (I_4 in this example) incorporates an interstitial and becomes a new {113}, or when an existing {113} traps an interstitial. On the contrary, the concentration reduces when a {113} releases an interstitial or when it evolves to a dislocation loop. All these events are captured by the following equation [247],

$$\frac{dC_{113}}{dt} = 5k_f C_I C_{I4} + k_a C_I D_{113} - k_b D_{113} - k_{113\to DL} C_{113} \quad (15)$$

where C_I is the free interstitial concentration and C_{I4} is the concentration of small interstitial clusters with size 4. The density of {113} defects increases when a small cluster evolves to a {113}, and reduces when {113} defects ripen to larger sizes or become dislocation loops,

$$\frac{dD_{113}}{dt} = k_f C_I C_{I4} - k_b \frac{D_{113}}{C_{113}} D_{113} - k_{113\to DL} k_{D113} D_{113} \quad (16)$$

k_f, k_a, k_b, $k_{113\to DL}$, k_{D113} are the reaction rates that control the kinetics of the system [247]. These equations have been tested with experimental values of supersaturation (Fig. 14), concentration of interstitials trapped in defects and defects size [246,247].

Under certain conditions, particularly for high-dose implants, {113} defects can evolve into dislocation loops. To simulate this transformation, the most simple models consider that the evolution occurs when the {113} defects reach a certain size, around 300 interstitials (less than 20 nm in leght). However, TEM images indicate that {113} defects can reach sizes for which the dislocation loop configuration is energetically more favorable [238]. Improved models consider a transformation rate that is controlled by a size-dependent energy barrier [264]. In continuum models, evolution of dislocation loops can be also described by a two-moment system in a similar way to {113} defects [247,250,251,265].

5 Amorphization and recrystallization

Since the beginning of the use of ion implantation for the fabrication of Si devices, ion-beam-induced amorphization and SPER in Si have been the subject of a great number of studies. There is a renewed interest in the modeling of these processes because of their technological relevance for the semiconductor industry to achieve high dopant activation with minimal diffusion. For example, high implant doses of As required to achieve high levels of carrier concentration induce amorphization of the Si lattice. For B doping with monatomic beams, preamorphizing Ge implants are used to take advantage of the high dopant activation achieved by SPER [266]. Implants of BF_2 or heavy molecules, such as decaborane or octadecaborane [267,268], are self-amorphizing [114]. Damage recovery is different in amorphizing and sub-amorphizing implants because in the former the SPER of the a-layer occurs at a relatively low temperature, and leaves a free-of-defects zone. The amount of residual damage beyond the a/c interface, which in turn affects dopant diffusion and activation, depends on the a-layer depth [269]. Ion-induced amorphization and recrystallization models, compatible with process simulators, must be able to predict the onset of amorphization and its dependence on implant parameters.

5.1 Fundamental studies

In order to develop models that describe amorphization and recrystallization processes at atomic level it is essential to identify the defect or defects that can act as amorphous embryos, and those that induce recrystallization. In the literature, several defects have been proposed to be relevant in the amorphization and/or recrystallization mechanisms: vacancies [270,271] and vacancy complexes [272–274], self-interstitial clusters [275–277], pairs of di-vacancies and di-interstitials [278], dangling bonds in the amorphous phase [279], kinks along [110] ledges in the a/c interface [280,281], and bond defects [74,282]. Among all of them, the bond defect appears to be the most adequate to describe amorphization and recrystallization.

Tang and coworkers encountered the bond defect when studying self-diffusion and $I-V$ recombination in Si using TB techniques [74]. They found that when a vacancy approaches a ⟨110⟩ dumbbell interstitial, a metastable defect structure is generated instead of having immediate $I-V$ recombination. For this reason the bond defect is also known as *IV pair*. This defect, represented in Figure 15, consists of a local rearrangement of bonds in the

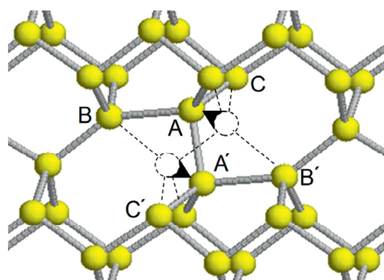

Fig. 15. Atomic structure of the IV pair. Dashed lines represent atoms and bonds in the perfect lattice. Atoms A and A′ move along the directions indicated by the arrows and switch their bonds with atoms B and B′, giving rise to the IV pair.

crystal with no excess or deficit of atoms. It introduces in the Si lattice the five- and seven-membered rings typical of the amorphous phase while maintaining perfect four-fold coordination. Information regarding the structure and energetics of this defect has been extracted using *ab initio* [59,283], TB [74] and CMD techniques [284]. The IV pair formation energy, 3.26 eV [59], is of the order of the corresponding to typical point defects in Si. Its equilibrium concentration should then be comparable or even larger than that of the other defects. However, the IV pair has not yet been detected experimentally, maybe because perfect four-fold coordination (which means no unpaired electrons) precludes its detection in standard experiments such as electronic paramagnetic resonance and electron nuclear double resonance. It has also been shown by *ab initio* techniques that the IV pair hardly disturbs the band structure of Si, which makes it undetectable in the deep level transient spectroscopy technique [283]. Using CMD techniques, Stock and coworkers observed that the bond defect can be generated not only by incomplete $I-V$ recombination, but also as a result of a pure ballistic process [282]. Thus the IV pair can be a primary defect generated by irradiation, with no need of pre-existing interstitials and vacancies in the lattice for its formation. They showed as well that the IV pair is a characteristic structural feature of the a/c interface [282,285].

The IV pair annihilates by the reverse movement of atoms A and A′ of Figure 15 toward the perfect lattice positions, switching again their bonds with atoms B and B′. Using CMD simulations, Marqués et al. showed that the IV pair lifetime follows an Arrhenius behavior over a wide temperature range with an activation energy of 0.43 eV [284]. At room temperature, the IV pair lifetime is about 3 μs, very short in comparison with the characteristic inter-cascade time at typical dose-rates. This indicates that the IV pair as an individual defect is not stable enough to accumulate and promote amorphization. However, the stability of the IV pair is affected by the proximity of other IV pairs in the Si lattice. CMD simulations indicate that IV pairs randomly scattered in the Si lattice and separated from each other by at least 4 Å recombine with an activation energy of 0.44 eV, i.e. as if they were isolated [286]. However, when the same number of IV pairs are arranged in a compact sphere with a radius of 1.2 nm, the activation energy for recombination is 0.86 eV, being the recrystallization dynamics slower. If IV pairs are arranged as to form a planar a/c interface, the activation energy is even higher, 2.44 eV, in good agreement with the experimental measurement of 2.7 eV [287]. This behavior indicates that IV pairs surrounded by crystalline atoms easily rearrange into the perfect crystal lattice structure, while IV pairs surrounded by other IV pairs have a larger effective energy barrier to rearrange.

According to CMD calculations, when IV pairs are present in the Si lattice to a given concentration (around 25%), amorphization of the Si lattice takes place [284]. The resulting structure is identical to the corresponding to a pure amorphous Si matrix. Besides, the amorphous zones created by IV pair accumulation and those by direct irradiation show the same features, as far as energy content, internal structure and recrystallization dynamics are concerned [108]. All these results indicate that amorphization can be achieved without the intervention of any additional defect, and also that amorphous pocket characterization can be studied by IV pair accumulation. This procedure of accumulating IV pairs can serve then as a controlled way to introduce damage in the Si lattice.

5.2 Atomistic KMC models

The results obtained from CMD and more fundamental methods set the basis of atomistic models implemented in KMC simulators that can reach actual Si processing scales. A unifying and consistent view of amorphization and recrystallization processes is provided by the atomistic amorphization model based on the IV pair [288]. It considers a-regions as agglomerates of IV pairs. To take into account the effect of the spatial distribution on the stability of IV pairs, each IV pair is locally characterized by the number of neighboring IV pairs [288,289]. Thus, the recombination rate of the IV pair decreases as the number of neighboring IV pairs increases reflecting the difficulty of "amorphous atoms" to properly rearrange when they have fewer neighboring atoms in crystalline positions.

IV pair recombination is a thermally activated process whose activation energy depends on the number of neighboring IV pairs. An activation energy for recombination of 0.43 eV is given to the isolated IV pair (0 neighbors), as obtained from CMD calculations [284]. IV pairs at a planar a/c interface are assigned the activation energy corresponding to that of the experimental recrystallization velocity, 2.7 eV [287]. IV pairs embedded into an amorphous matrix (completely surrounded by neighboring IV pairs, and thus with full coordination) have an activation energy of 5 eV, coincident with the experimentally observed activation energy for crystal nucleation in amorphous Si [290]. Other coordination numbers have intermediate activation energies, as shown in Figure 16, whose values have been obtained by the calibration of the model with experimental results [291].

The SPER velocity of a planar a/c interface and a-pockets has been experimentally observed to depend on

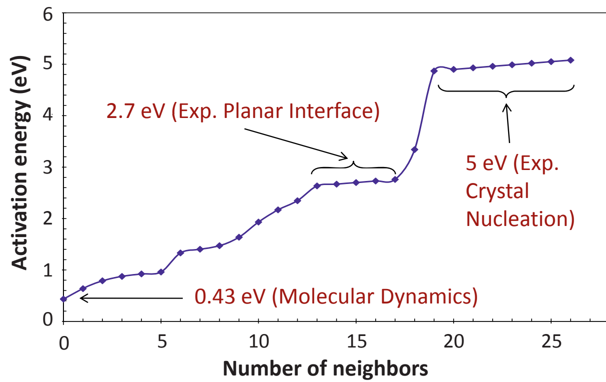

Fig. 16. Activation energies for IV pair recombination as a function of the number of neighboring IV pairs.

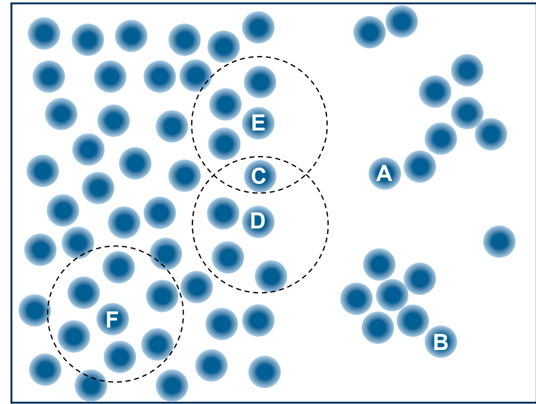

Fig. 17. Schematic of a damage distribution in which a continuous a-layer and several a-pockets are shown. IV pairs are represented by solid circles. For some IV pairs a dotted circle indicates their neighboring IV pairs.

the presence of impurities [292,293]. Dopants usually enhance SPER whereas non-dopant impurities, such as F, generally decrease it. The impurity effect on SPER is taken into account in the model by making the recombination probability of IV pairs to depend, not only on the number of neighboring IV pairs, but also on the local impurity concentration, according to the experimental data of Olson et al. [287,292].

The local characterization of the disordered atoms allows the model to capture any damage morphology that may arise from irradiation cascades, as well as the characteristic regrowth behavior observed in experiments [289]. Figure 17 is a schematic that shows a continuous a-layer and several a-pockets; for some IV pairs a dotted circle is used to highlight their neighboring IV pairs. Isolated IV pairs and those belonging to small a-pockets have few neighbors and recombine sooner. IV pairs at the corners or fingers of a-pockets, and therefore belonging to convex regions (like A and B in Fig. 17), have fewer neighboring IV pairs and recombine faster, shortening the lifetime of irregular a-pockets compared with more compact structures [108,289]. IV pairs at an a/c interface (C) have fewer neighboring IV pairs than those embedded within the a-region (F), and therefore recrystallization (IV pair recombination) will start at the interface. A continuous a-layer with a perfectly planar a/c interface is just a particular case of a-region, where all IV pairs at the interface have the same number of neighboring IV pairs and follow the same activation energy for regrowth, 2.7 eV. The recombination of the first IV pair at the planar interface (C) starts a triggering mechanism in which its neighbors (D and E) are the most likely ones to be recombined next since they have lost a neighbor (the one that has recombined first). This mechanism leads to the complete recrystallization of the whole monolayer. A new triggering event is required to start the regrowth of the next monolayer.

This simple model based on the IV pair encompasses and unifies homogeneous and heterogeneous mechanisms for amorphization. The nucleation of the amorphous phase consists of the formation of IV pair structures with enough number of IV neighbors to be stable. At the appropriate temperatures, these amorphous embryos can be either small IV pair complexes generated in dilute cascades (homogeneous nucleation) or dense IV pair agglomerates formed in the cascades of heavy ions (heterogeneous amorphization). Preexisting a-pockets or planar a/c interfaces can act as nucleation sites [294,295]. Isolated IV pairs may not be able to survive by themselves but, if they interact with a preexisting a-region, the generated IV pairs will have more IV neighbors and become stable. IV pairs are thus added to the amorphous zone producing its growth. The superlinear behavior of the accumulated damage versus dose [296] is also a consequence of the increased stability of the IV pairs with the number of IV neighbors.

The adequate modeling of dynamic annealing in process simulators is very important since it may strongly affect damage accumulation during the implant. Implant temperature, beam current and ion mass may determine whether most of generated damage anneals out during the implant or it accumulates leading to the formation of a-regions. In this model, implant temperature directly affects the stability of IV pairs, since the recombination of IV pairs is a thermally activated process. At low temperatures most generated IV pairs are stable, while at high temperature isolated IV pairs and those with few neighboring IV pairs quickly recombine, and only IV pairs belonging to large a-regions survive [289]. Beam current sets the temporal separation between cascades and therefore, the time during which the damage generated by one cascade undergoes dynamic annealing, before another cascade arrives at the same region increasing the damage. Damage topology is affected by ion mass. Light ions generate dilute damage that easily anneals out, while heavy ions produce large a-pockets that may be stable enough to survive dynamic annealing [297].

The a-regions generated during an implant cascade may contain a local excess (Is) or deficit (Vs) of atoms within the amorphous matrix. When an isolated a-region completely recrystallizes, the unbalanced atoms are released to the crystal and they appear as Si interstitials or vacancies, as reported by CMD simulations of the regrowth of a-pockets [111]. On the contrary, the regrowth of a continuous a-layer that extends to the surface results

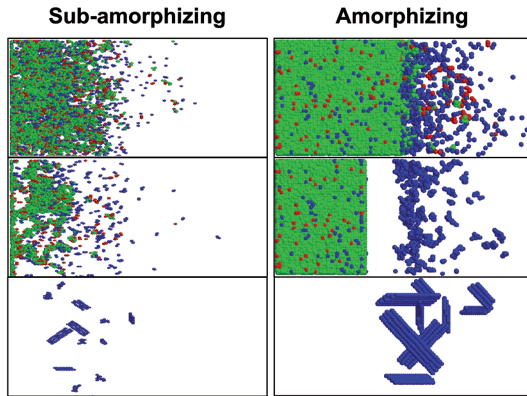

Fig. 18. Simulations of the annealing at 800 °C of a sample implanted with 5 keV 10^{14} cm^{-2} Si (sub-amorphizing) and 5 keV 10^{15} cm^{-2} Si (amorphizing). IV pairs are plotted as green circles, whereas Si Is and Vs are indicated by blue and red circles, respectively. Several snapshots during recrystallization are shown. Top images represent the as-implanted profiles.

in a regrown layer free of defects, because the local excess or deficit of atoms are swept toward the surface and annihilate there. In this model, the energy of the local excess or deficit of atoms decreases with the number of neighboring IV pairs, which implies that they tend to be within the a-region. As IV pairs recombine and the interface advances, the local excess or deficit of atoms is likely to be moved to inner regions of the a-layer. In Figure 18 it is shown the as-implanted damage profiles and several snapshots during the recrystallization of sub-amorphizing and amorphizing implants [298]. In the sub-amorphizing sample the as-implanted profile shows crystalline islands surrounded by large a-regions. Upon annealing isolated a-regions recrystallize, releasing the unbalanced atoms they contain. Finally, after recombination, defects are present along the damage profile but they accumulate around the mean projected range of the implant. The amount of Si Is retained in defects is approximately the implanted dose ("+*1* model" [252]). On the contrary, simulations show how defects contained in the continuous a-layer are swept toward the surface as the interface advances and are eliminated there. A band of extended defects is formed only at the end-of-range (EOR) region, the dose of Is stored in defects being lower than the implanted dose.

The detailed atomistic amorphization model described handles and stores all IV pairs generated during the implant process, up to the limit imposed by the amorphous material density. As each IV pair consists of two lattice atoms, a fully amorphous Si region represents an IV pair concentration of 2.5×10^{22} cm^{-3}. This high defect concentration translates into significant CPU time and memory requirements. This limitation has been overcome in some KMC models that implement a less detailed description of the amorphous phase, using the a-pocket as the basic amorphous structure [299]. A-pockets are considered as three-dimensional, irregular shape agglomerates of an arbitrary number of interstitials and vacancies and trapped impurities. A-pockets can grow by incorporating additional particles as the implant proceeds or shrink due to annealing. Their recrystallization is a thermally activated process whose activation energy depends on the effective size of the a-pocket, without taking into account the morphology [300]. The size is considered as the minimum number of Is or Vs it contains, i.e. the overall number of IV pairs. This number can be rather large because it refers to the whole size of the a-pocket, and it is not limited to the local neighboring distribution. By fitting the simulation results to experiments [291], the activation energy for the shrinking of an a-pocket from size s to size $(s-1)$ was estimated to be 0.7 eV for $s = 1$ and saturating at 2.7 eV for $s > 225$.

To optimize CPU time and memory consumption, the space is divided in small boxes of about 1 nm^3. When the defect $(I + V)$ concentration associated to the a-pockets in one of these boxes exceeds the amorphization threshold (1.5×10^{22} cm^{-3}), the box is labeled as a-region [299,300]. When an a-region is formed, only the number of unbalanced atoms and impurities it contains is stored, but the positions of the particles are not kept. Recrystallization of each of these boxes occurs as a whole at a rate given by the experimental regrowth velocity of a planar a/c interface and, if needed, the unbalanced atoms are transfered to neighboring boxes or released to the bulk.

5.3 Implementation in continuum methods

Continuum methods usually simulate the crystalline to amorphous transition induced by ion implantation by means of a critical energy/defect density model [301,302]. BCA calculations are typically used to evaluate the nuclear energy transferred to the lattice during the collision cascade. The critical energy density model states that the implanted region turns amorphous when an energy density threshold is exceeded, usually considered as approximately 5×10^{23} eV/cm^3 [6,303–305]. The deposited nuclear energy is responsible for the formation of defects in the crystalline lattice, according to the KP formula (Eq. (7)). Therefore, a critical defect concentration (CDC) can be used instead of an energy density to determine the crystalline to amorphous transition, typically in the order of 1.15×10^{22} cm^{-3} [306]. When the theoretical damage profile is compared with the position of the a/c interface experimentally measured, the CDC value required to obtain a good fitting is not unique. Variations of more than one order of magnitude have been reported [269], and it has been found to depend on ion mass, dose rate and implant temperature, among others. These variations introduce uncertainty in the position of the a/c interface. As it is shown in Figure 19, a small change in the position of the interface may result in a large change in the amount of residual damage remaining beyond the interface after SPER, which may reach up to 50% [307]. The dependence of the CDC value on implant parameters is due to the effects of dynamic annealing on damage accumulation. This effect can be taken into account by considering that a fraction of generated defects recombines during implant, as indicated in equation (8) [162].

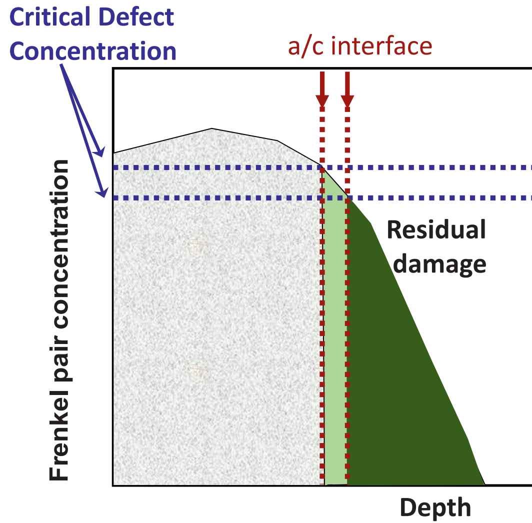

Fig. 19. Schematic that shows the a-layer depth and the amount of residual damage associated to two different CDC values.

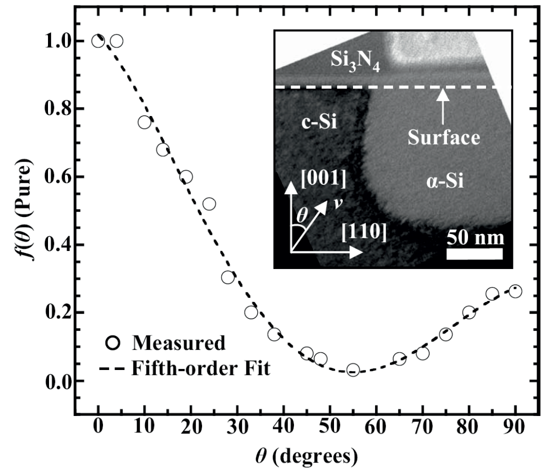

Fig. 20. The normalized SPER velocity, $f(\theta)$, as a function of the substrate orientation angle from [001] toward [110], θ, as measured by Csepregi et al. [309]. The inset shows a cross-section TEM micrograph of a typical 2D structure where the SPER process occurs (from Ref. [308]).

Since SPER is much faster than the dissolution of extended defects, for process modeling purposes the recrystallization of a-regions is sometimes assumed to occur instantaneously, leaving no defects in the recrystallized region, and only the residual defects beyond the a/c interface remain. Nevertheless, this is a very simplistic approach that does not account for the three dimensional (3D) topology of a-regions formed in the fabrication of transistors. In a general sense, SPER is a three dimensional process, but it can be treated as two dimensional, considering than the width of the transistor is very long. Recently, Morarka et al. have developed a model for the evolution of the SPER in two dimensional structures, based on level set methods [308]. In this model, the local velocity of the regrowth front is considered to depend on the crystallographic orientation of the interface [309] and the local interfacial curvature [310],

$$v(\theta, k) = v_{[001]} f(\theta)(1 + Ak), \tag{17}$$

where $v_{[001]}$ is the regrowth velocity along [001], θ is the substrate orientation angle from [001] to [110], A is a constant (2.0×10^{-7} cm) and k is the local interfacial curvature. $f(\theta)$ is a fit to the normalized regrowth velocity as a function of θ measured by Csepregi et al. as shown in Figure 20, using a least-squares fifth-order polynomial [308].

According to equation (17), if a portion of crystalline Si is encompassed by amorphous Si (convex or negative curvature) SPER should be retarded. On the contrary, SPER is enhanced when a region of amorphous Si is encompassed by crystalline Si (concave or positive curvature). The effect of the interface curvature on regrowth rate is analogous to the dependence of the IV pair recombination rate on the number of neighboring IV pairs. Those IV pairs located at a concave interface are mostly surrounded by crystalline Si (they have few neighboring IV pairs) and will undergo a fast recrystallization. If the curvature increases, the number of neighboring IV pairs is reduced, which will enhance the recrystallization rate [289].

6 Dopant-defect interactions

During some of the process steps in the fabrication of Si-based ICs, impurities or dopant atoms are selectively introduced into the Si substrate to modify its electrical conductivity and form n-type and p-type regions. The geometry and carrier concentration in these regions determine the electrical characteristics of electronic devices. For this reason, a great attention has been focused on understanding dopant behavior in Si, and the prediction of the spatial distribution of donors and acceptors after processing is one of the main goals of process simulation. The most commonly used species to dope Si are the group-III acceptor impurities B, Ga, In, and Al and the group-V donor impurities P, As, and Sb.

Two of the most relevant dopant properties for Si processing are the equilibrium solid solubility limit and diffusivity, whose values for the most common dopants in Si are included in Figures 21 and 22, respectively. The first one determines the maximum concentration which can be incorporated into the substitutional sites of the host lattice under equilibrium thermodynamic conditions without inducing a phase transition. Typically dopants need to dissolve substitutionally to be electrically active. Therefore, to achieve high carrier concentrations in Si high solid solubility values for dopants are required. On the other hand, dopant diffusivity is desirable to be low to avoid the broadening of shallow dopant profiles during thermal processes. B is the most common p-type dopant used for the formation of p-type regions in Si due to its high solid solubility, although it is a quite fast diffuser. In the case of n-type dopants, As is one of the slower diffusers, which combined

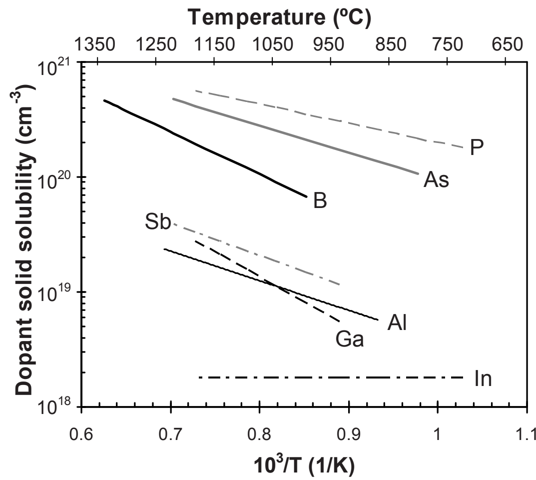

Fig. 21. Equilibrium solid solubility limits for B [311], Al [312], Ga [313], In [314], P [315], As [316] and Sb [317].

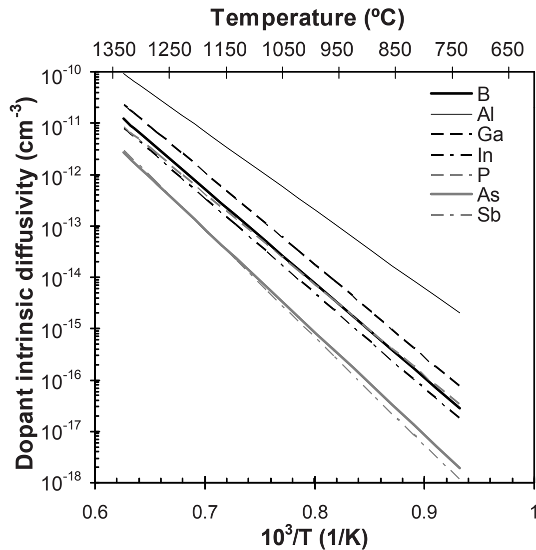

Fig. 22. Temperature dependence of intrinsic diffusivity for B, Al, Ga, In, P, As and Sb (from Ref. [192]).

with its high solid solubility make it the most preferred dopant to form n-type regions in Si.

These two equilibrium properties ultimately limit the electrical activation and the position of the introduced dopants. However, the situation is even more complex under non-equilibrium conditions as it occurs during dopant implantation. The implantation process generates damage in the Si lattice and the implanted dopants generally reside in non-substitutional positions, being thus electrically inactive. This makes necessary a post-implant annealing to annihilate damage and to electrically activate dopants. During these processes dopant-defect interactions take place, which enhance diffusivity above equilibrium values and decrease electrical activation below the solid solubility limit. These features complicate the formation of shallow and electrically active dopant profiles.

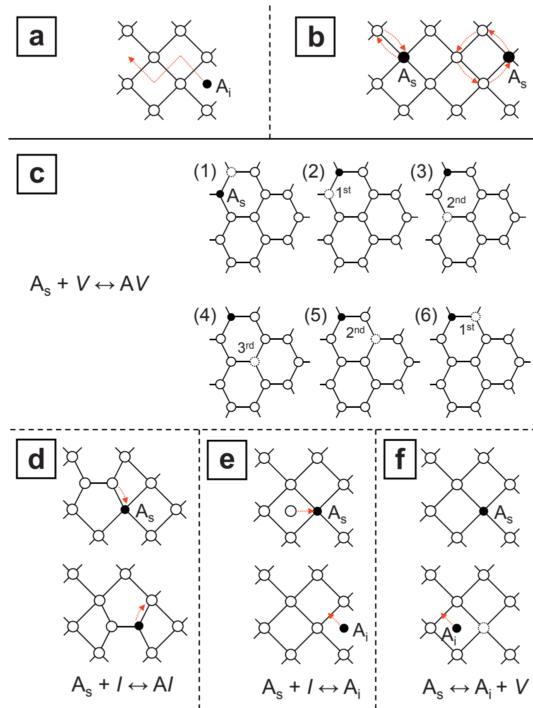

Fig. 23. Schematic two-dimensional representation of (a, b) direct and (c–f) indirect diffusion mechanisms of an impurity A in Si. A_i and A_s denote interstitially and substitutionally dissolved impurities whereas V and I represent vacancies and Si self-interstitials, respectively. AV and AI are defect pairs of the corresponding defects. Open circles represent Si atoms, dashed circles denote vacancies and black circles represent dopants.

6.1 Dopant diffusion mechanisms

The understanding and modeling of diffusion mechanisms is key for the prediction of dopant profiles. Figure 23 illustrates the possible mechanisms of diffusion of an impurity atom A in Si [185,318,319]. There are two basic types of mechanisms by which substitutional dopant impurities can diffuse: a *direct mechanism* or intrinsic mechanism that occurs spontaneously (i.e., in the absence of defects) in the bulk, and an *indirect mechanism* mediated by native point defects, such us vacancies and self-interstitials.

Figure 23a shows schematically a direct mechanism of diffusion via interstitial lattice sites without involving intrinsic point defects. It occurs for small impurities with small ionic radii that dissolve at the interstitial sites (A_i) in Si. Especially group-I and group-VIII elements diffuse mainly directly and are therefore fast diffusers. The direct mechanisms of diffusion of atoms on substitutional sites (A_s), shown in Figure 23b, can occur by means of a concerted exchange with an adjacent Si atom or a ring mechanism that does not involve any defects. Atoms move through a set of configurations in such a way that at any stage the number of broken bonds as well as distortions are kept at a minimum [320]. However, this mechanism requires very large activation energy and does not play a significant role in the diffusion of substitutional dopants in Si [185].

The diffusion of A_s by indirect mechanisms is usually more favorable. Various indirect diffusion mechanisms, that involve intrinsic point defects, are illustrated in Figures 23c–23f. These mechanisms can be expressed by the following point-defect reactions:

$$A_s + V \leftrightarrow AV, \quad (18)$$

$$A_s + I \leftrightarrow AI, \quad (19)$$

$$A_s + I \leftrightarrow A_i, \quad (20)$$

$$A_s \leftrightarrow A_i + V, \quad (21)$$

where A stands for the impurity atom, I for Si self-interstitial, V for vacancy, and the subscripts s and i indicate substitutional and interstitial positions, respectively. Reactions (18) and (19) represent the vacancy and interstitialcy mechanisms, respectively, shown in Figures 23c, 23d. In both reactions, isolated intrinsic defects approach substitutional impurities and form next-nearest AV and AI defect pairs due to Coulomb attraction and/or minimization of local strain. Reactions (20) and (21) (shown in Figs. 23e, 23f) represent the "kick-out" and Frank-Turnbull mechanisms, respectively. These two last reactions describe the diffusion behavior of hybrid elements that are mainly dissolved on substitutional sites, but that move as interstitial defects (A_i).

The vacancy mechanism of diffusion for a substitutional impurity (reaction (18)), shown schematically in Figure 23c, consists of a migration through the host lattice by moving onto an adjacent vacant lattice site. After exchange, in order to complete one diffusion step, the AV pair must partially dissociate, and the vacancy has to diffuse to at least a third nearest-neighbor site in the Si lattice so that it may return to a different lattice site adjacent to A_s along a different path.

Dopant diffusion via the interstitialcy mechanism (reaction (19)), shown schematically in Figure 23d, occurs when an isolated dopant atom in a substitutional position is approached by one of the atoms in a Si interstitialcy (two atoms in non-substitutional positions configured about a single substitutional lattice site) and form a dopant interstitialcy AI. The migration of the dopant interstitialcy takes place when the dopant moves toward an adjacent lattice site (already occupied by a Si atom) where it re-forms the dopant interstitialcy with the new Si atoms.

Dopant diffusion by the "kick-out" mechanism or the substitutional/interstitial interchange mechanism (reaction (20)) is shown in Figure 23e. It occurs when a dopant atom is displaced or "kicked-out" from the substitutional site into an interstitial site by a Si self-interstitial. The dopant atom migrates though interstitial channels as a dopant interstitial A_i until it takes up a substitutional site again by dislodging a Si atom from a substitutional site.

Finally, reaction (21) describes the dissociative or Frank-Turnbull mechanism where a pair of interstitial impurity and vacancy is formed at the cost of a substitutional impurity, as it is shown schematically in Figure 23f. The Frank-Turnbull mechanism is commonly believed to be negligible for the diffusion of p- and n-type dopants in Si.

Reactions (19) and (20) are similar in nature. Both predict an increase in mobile dopant atoms in the presence of excess Si interstitial concentrations. This makes very difficult to differentiate between the two mechanisms experimentally. From the point of view of predicting the redistribution of dopants the distinction between both mechanisms is not so relevant.

Both experimental observations and theoretical calculations indicate that diffusion of common dopants in Si is mediated by Si self-interstitials or vacancies. Generally, the diffusivity D_A of a dopant A is related to the concentration of the native point defects by [185]:

$$\frac{D_A}{D_A^*} = f_A \frac{C_I}{C_I^*} + (1 - f_A) \frac{C_V}{C_V^*} \quad (22)$$

where C_I/C_I^* and C_V/C_V^* represent the enhancement of the concentrations C_I and C_V of I and V, over the equilibrium value (denoted with "*"), respectively, and f_A is the interstitial fraction of diffusivity. Generally one of the two contributions to dopant diffusion, interstitials or vacancies, is dominant [321]. Thus, it is generally assumed that Si self-interstitials assist B, Al, Ga, In and P diffusion, whereas vacancies assist Sb diffusion. As is one of the few impurities that experiences diffusion assisted both by Si self-interstitials and vacancies.

Dopant diffusivity can vary when diffusion occurs under extrinsic doping conditions, well above the intrinsic electron concentration, n_i, at the annealing temperature. This effect has mainly been discussed within a model which considers Fermi-level-dependent point-defect concentrations due to the different charge states of the point defects [185,318]. It has been modeled in continuum methods by effective diffusion coefficients dependent on carrier concentration, being the general form of the diffusivity for a dopant A through an AX diffusing species (X refers either to a Si self-interstitial or a vacancy) [185]:

$$D_A^{eff} = D_{AX}^0 + D_{AX}^+ \left(\frac{p}{n_i}\right) + D_{AX}^{++} \left(\frac{p}{n_i}\right)^2 + D_{AX}^- \left(\frac{n}{n_i}\right) + D_{AX}^{=} \left(\frac{n}{n_i}\right)^2, \quad (23)$$

where n and p are the actual electron and hole concentrations at the anneal temperature, respectively, D_{AX}^0 is the intrinsic diffusion coefficient, and where the superscripts affecting D_{AX} refer to diffusion coefficients mediated by species with one or two positive or negative additional charges with respect to the substitutional dopant. Fermi-level effects have also been implemented in atomistic KMC models by considering in detail the different energetics of the various charge states of native defects and mobile dopant species, assuming local electrical equilibrium with Fermi level due to fast charge reactions [322,323].

In the following subsections the diffusion mechanisms of the most popular p-type and n-type dopants (B and As, respectively) are discussed in more detail.

Table 1. Migration and binding energies for B diffusion reported in the literature by several authors.

Authors (Ref.)	E_m^{BI} (eV)	E_b^{BI} (eV)	Diffusion mechanism	Method
Zhu et al. [64]	0.3	1.1	"Kick-out"	DFT
Sadigh et al. [63]	0.68 (MD)	0.9/[1.03]	Interstitialcy	MD-DFT
Windl et al. [62]	0.4–0.7	0.6/[0.9]	Interstitialcy	DFT
Alippi et al. [324]	0.66	–	Interstitialcy	TB-MD

6.1.1 B diffusion

B is generally introduced in Si by ion implantation. However, during subsequent thermal anneals, the B profile experiences a broadening significantly higher than expected from equilibrium B diffusivity due to TED [7,8,11], which poses a severe limitation for the formation of shallow junctions. The many studies devoted to the understanding and control of TED were correlated to the release of Si self-interstitials from small clusters and extended defects resulting from ion implantation [8,12,245]. Moreover, it has been observed experimentally that B diffusion is retarded during nitridation anneals (vacancy injection) and enhanced during oxidation anneals (Si self-interstial injection) compared to reference anneals in inert ambient [325]. Thus, it has been determined that B diffusion in Si is dominated to a degree of more than 98% by an interstitial or interstitialcy mechanism [321,325]. Therefore, the mobile entity for B diffusion is expected to be a B atom paired with a Si self-interstitial, either by an interstitialcy (Eq. (19)) or a "kick-out" (Eq. (20)) mechanism.

To accurately model dopant diffusion it is important to know the energetics governing the interaction of B and the Si self-interstitial as well as the diffusion barriers. The atomic details of B diffusion in Si have been studied by several authors using *ab initio* calculations [62–64,324]. Zhu et al. [64] proposed a "kick-out" mechanism in which the resulting B interstitial, B_i, can migrate through interstitial channels (with a migration barrier of 0.3 eV) for quite a long distance before falling back to another substitutional position. The energy barrier for the initial "kick-out" is about 1.0 eV whereas the energy barrier for the final reverse "kick-out" in the absence of vacancies is 0.6 eV, according to the scheme shown in Figure 24a. Several authors have proposed a similar "kick-out" mechanism for B diffusion [60,326]. More recently, several studies have revised this picture using more sophisticated *ab initio* DFT calculations. These studies suggested an interstitialcy mechanism for B diffusion in which BI pairs diffuse in the Si lattice with an energy barrier around 0.7 eV [62,63,324], following the scheme included in Figure 24b [63]. The configuration of the B atom is iteratively reversed from interstitial to substitutional and back. This mechanism has been experimentally evidenced for highly extrinsic substrates [327]. The change in the charge state affects the mean free path and generation rate of the mobile species. Table 1 summarizes the results of the theoretical calculations reported by different authors for the migration and binding energies of the mobile interstitial-B entity (E_m^{BI} and E_b^{BI}, respectively), the

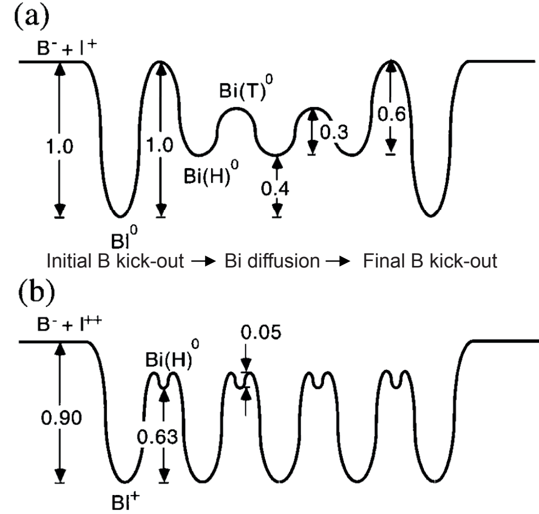

Fig. 24. Comparison for the B diffusion mechanism including charge states and energy barriers for: (a) the "kick-out" mechanism for B diffusion calculated by Zhu et al. [64] that predicted an effective migration barrier for the mobile species of $0.4 + 0.3 = 0.7$ eV, (b) the interstitialcy mechanism calculated by Sadigh et al. [63] that predicted a migration energy of $0.63 + 0.05 = 0.68$ eV.

diffusion mechanism suggested by these authors and the theoretical method used for these calculations.

6.1.2 As diffusion

As is one of the few impurities which diffuse in a considerable degree via Si self-interstitials as well as via vacancies [185,325,328–331]. Some values reported in the literature for the interstitial fraction of diffusivity for As, f_A, are compiled in Table 2. The two contributions are the consequence of the existence of two mobile As configurations, AsV (the association of an As atom with a vacancy) and AsI (either an As in an interstitial position or a pair of a substitutional As plus a Si self-interstitial). Thus, the reactions that control As diffusion are then given by equations (18) and (19)–(20). The migration and binding energies of AsV and AsI determine the As diffusion. If the concentrations of AsV and AsI are altered, e.g., due to the I supersaturation generated after As implantation, the As experiences TED [15,325,332].

From an atomistic point of view, the AsV pair migration is assumed to follow a vacancy ring mechanism in which the vacancy loops around the As atom for the pair to complete one diffusion step, as illustrated in Figure 23b.

Table 2. Interstitial fraction of diffusivity for As reported in the literature by several authors.

Authors (Ref.)	f_A for As	Temperature range (°C)
Matsumoto et al. [328]	42exp(–0.542 eV/kT)	950–1100
Mathiot & Pfister [329]	29.5exp(–0.6 eV/kT)	1100
Cowern [330]	∼0.4	1100
Novell and Law [331]	∼0.4	1000
Ural et al. [325]	0.33–0.57	1100

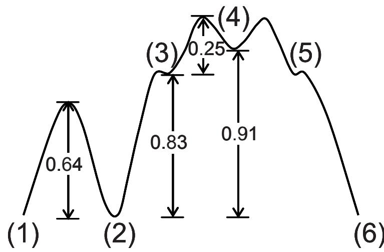

Fig. 25. Energy barriers obtained by Harrison [333] using DFT calculations. In brackets is represented the successive vacancy positions (represented schematically in Fig. 23c) in the loop around the dopant.

Several authors have supported by theoretical calculations this picture for AsV migration and found neutral AsV pair to be the most stable configuration. As an example, the energetics calculated by Harrison [333] for AsV^0 migration by using DFT calculations are shown in Figure 25. This author found a total diffusion barrier of the AsV^0 pair of 1.08 eV. Other values reported in the literature are included in Table 3. All of them indicate that the migration and binding energies are comparable (in the 0.9–1.6 eV range).

Less theoretical studies and data can be found in the literature regarding the mechanisms for AsI diffusion. The focus on vacancy-mediated diffusion can be attributed to earlier empirical models [329] and theoretical DFT calculations that computed a strong binding energy between As and a vacancy compared to that between As and a Si self-interstitial [61,334]. These previous studies supported the hypothesis that the vacancy mechanism dominantly contributes to the As diffusion. However, experimental evidences have suggested an important role for Si self-interstitials in As TED [15,325,341]. More recently, Harrison et al. [340] have analyzed the structure, stability and diffusion of AsI pairs based on *ab initio* DFT calculations. These authors found for the AsI^- pair a minimum energy structure in which the As atom bridges two approximate lattice Si atoms, whereas for the AsI^0 and AsI^+ they found that the lowest energy structure is comprised of an As and Si self-interstitial pair that is aligned in the [110] direction while sharing a lattice site. Under intrinsic conditions, they estimated migration and binding energies lower than those extracted by other authors by fitting models to experimental data, whose results are summarized in Table 4.

It has been experimentally observed that As diffusion significantly increases with electrically active As concentration [342]. As a result, instead of Gaussian-like diffusion profiles, characteristic box-like profiles appears for high As concentrations. For low-to-medium dopant concentrations (less than $\sim 2 \times 10^{20}$ cm^{-3}), equation (23) that includes Fermi-level effects on dopant diffusion gives a very good account of the experimental data on concentration dependent As diffusion. However, for concentrations slightly above 2×10^{20} cm^{-3} the As diffusion coefficient has been found to depend on n/n_i to a power higher than 2 [342], indicating that this model might not be adequate for high dopant concentrations. Moreover, strongly enhanced diffusion of ion implanted As in Si for As concentrations above $\sim 2 \times 10^{20}$ cm^{-3} has been reported [343], which also indicated that the above mentioned model could be not valid at high concentrations. Mathiot and Pfister suggested that enhanced As diffusion above this critical doping threshold was due to accelerated diffusion of vacancies through an "infinite percolation network" formed when the As concentration exceeds $\sim 3 \times 10^{20}$ cm^{-3} [344]. In this scenario they considered the case in which two As atoms are fifth neighbors of each other. If one of these As atoms is connected to a vacancy, then, during the migration of the AsV pair, when the V is a third neighbor of one As atom, it would be a second neighbor of the other. The net effect is a lowering of the migration energy. In contrast, Ramamoorthy et al. [61] rejected this percolation model arguing that this mechanism would let to a quick As clustering with vacancies and enhanced diffusion would halt rapidly, in contradiction with experimental observations [345,346]. Instead, they proposed an atomistic mechanism in which a mobile As_2V complex would be responsible for the observed diffusion enhancement.

6.2 Dopant-defect clusters

It has been experimentally observed that dopant implantation and subsequent annealing lead not only to TED of dopants but also to the formation of immobile and electrically inactive peak regions in dopant profiles, even at concentrations well below the solid solubility limit [10,11,14]. This phenomenon has been associated to the interaction between dopants and defects under non-equilibrium conditions that causes the formation of immobile and electrically inactive dopant-defect clusters, thus limiting dopant activation.

6.2.1 B clusters

The phenomena of B clustering and TED have been analyzed by several authors from experimental and theoretical

Table 3. Migration and binding energies for the different charged species of the AsV pair reported in the literature by several authors. Abbreviations AIC and FMED stand for isothermal Annealing studies of Irradiated Crystals containing As, and Fitting Models to Experimental Data, respectively.

Authors (Ref.)	Charge state	E_m (eV)	E_b (eV)	Method
Ramamoorthy et al. [61]	AsV^0	1.4	1.31	DTF
Sugino et al. [334]	AsV^0	0.9	0.9	DTF
Harrison [333]	AsV^0	1.08	1.3	DTF
Elkin and Watkins [335]	AsV^0	1.07	–	EPR
Hirata et al. [336]	AsV^0	1.07	–	AIC
Baccus et al. [337]	AsV^0	∼1.5	1.51	FMED
	AsV^-	–	1.52	
Hane et al. [338]	AsV^0	–	1.0	FMED
	AsV^-	–	1.6	
Pinacho et al. [339]	AsV^0	1.3	1.3	FMED
	AsV^-	1.6	1.6	
	AsV^+	1.3	1.01	

Table 4. Migration and binding energies for the different charged species of the AsI pair reported in the literature by several authors.

Authors (Ref.)	Charge state	E_m (eV)	E_b (eV)	Method
Harrison et al. [340]	AsI^0	0.15	0.59	DTF
	AsI^-	0.42	0.72	
	AsI^+	0.22	0.37	
Baccus et al. [337]	AsI^0	∼0.8	1.53	FMED
Hane et al. [338]	AsI^0	–	1.0	FMED
Pinacho et al. [339]	AsI^0	1.4	1.0	FMED
	AsI^+	1.4	0.1	

points of view. There is a consensus on the idea that TED is caused by the interaction of a Si self-interstitial and a B atom to form a mobile BI species, whereas B clustering is associated to the interaction between several B atoms and Si self-interstitials to form immobile and electrically inactive *B-interstitial clusters* (BICs) [7,10,11,185].

Experiments based on B markers in Si have shown that TED takes place even for relatively low Si interstitial supersaturations (as occurs for instance under oxidizing anneals [347]). However, B clustering only occurs for B concentrations higher than 1×10^{18} cm^{-3} [10] in the presence of a very high Si interstitial supersaturation such as the one that exists in the damaged zone of implanted regions [7,10,11], as it is illustrated in Figure 26. The immobilization of a fraction of B atoms occurs before any diffusion, i.e. during implantation and at the very early stages of anneals [11,348]. Based on these observations, Pelaz et al. [11,120] proposed a model for B clustering based on the formation of immobile precursors consisting of a B atom and several Si self-interstitials, that inhibit B diffusion and act as nucleation centers for the growth of BICs. This model includes a complex pathway for B and Si self-interstitials interactions that leads to the formation and dissolution of the different B$_n I_m$ configurations through the trapping/emission of mobile species (I, BI), described by the following reactions:

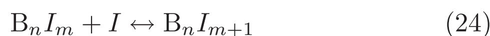
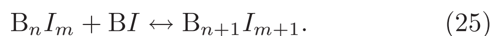

$$\mathrm{B}_n I_m + I \leftrightarrow \mathrm{B}_n I_{m+1} \quad (24)$$

$$\mathrm{B}_n I_m + \mathrm{B}I \leftrightarrow \mathrm{B}_{n+1} I_{m+1}. \quad (25)$$

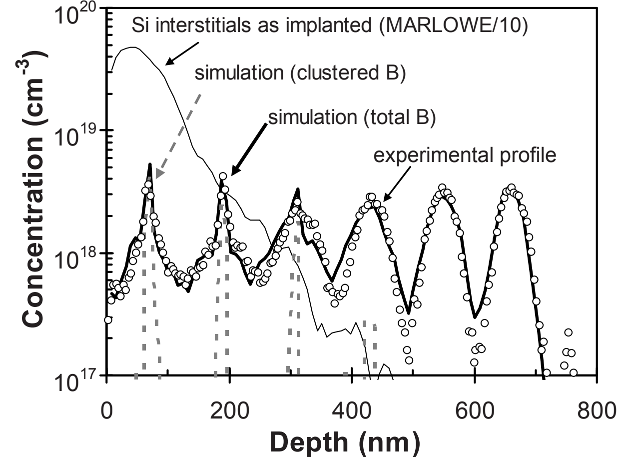

Fig. 26. Experimental profiles in a B-doped superlattice after a 40 keV, 5×10^{13} cm^{-2} Si implant and annealed at 790 °C for 10 min (open circles), along with simulation data for the MARLOWE calculation of the initial Si interstitial distribution after implantation, and the resulting doping markers into Gaussian diffusion profiles and an immobile (clustered) fraction in the near-surface spikes [11]. Only B markers in the damaged region show the characteristic peak associated to BIC formation for B concentrations higher than 1×10^{18} cm^{-3} whereas all the B markers experience TED.

The probabilities for the capture and emission of each species are given by the concentrations of B atoms and Si self-interstitials, as well as the total energies of the

+BI

+I

$B_nI_m + BI \leftrightarrow B_{n+1}I_{m+1}$

$B_nI_m + I \leftrightarrow B_nI_{m+1}$

Configuration	Liu et al. (DFT)	Alippi et al. (DFT-TB-MD)	Lenosky et al. (DFT)	Pelaz et al./Current model (FMED)
B_4	--/--	0.27/1.85	--	-0.8/+1.5
B_3	+2.3/+2.2	0.11/1.20	1.54	-0.6/+1.3
B_4I	-1.3/-2.1	-4.52/-4.32	-1.85	-4.6/-3.3
B_2	+0.9/+0.9	-0.07/0.78	1.38	0/+0.9
B_3I	-2.3/-3.0	-4.22/-4.14	-2.72	-3.6/-2.7
B_4I_2	-4.3/-5.5	-8.83/-7.15	-4.8	-6.8/-6.2
B	0/0	0/0	0	0/0
B_2I	-1.2/-2.0	-2.97/-3.03	-2.12	-0.6/-1.6
B_3I_2	-2.6/-4.1	-6.72/-5.58	-4.41	-5.8/-5.6
B_4I_3	-5.9/-7.0	--/--	--	-9.0/-8.9
BI	-0.4/-0.5	-0.43/-1.15	-0.79	-0.6/-1.0
B_2I_2	-2.4/-3.0	-5.14/-4.15	-3.24	-3.0/-3.2
B_3I_3	-5.6/-6.6	--/--	--	-7.8/-7.8
B_4I_4	-7.8/-9.2	--/--	--	-10.9/-11.2
BI_2	-2.3/-2.5	-3.23/-2.74	-2.24	-2.0/-2.2
B_2I_3	-5.3/-6.0	--/--	--	-3.0/-4.6
BI_3	-4.5/-4.8	--/--	--	--/-3.6

Liu *et al.* (DFT)
Alippi *et al.* (DFT-TB-MD)
Lenosky *et al.* (DFT)
Pelaz *et al.*/Current model (FMED)

Fig. 27. Total energies (in eV) for different B_nI_m configurations given by several authors in the literature, along with the current values included in the model. Total energies were determined by theoretical calculations [65,66,349] or by FMED [120].

different BIC configurations. Total energies for each B_nI_m configurations (relative to the isolated components) determined by fitting their simulations to experimental data are presented in Figure 27, including the original set of values reported by Pelaz et al. [120] as well as the current recalibration and theoretical calculations reported by other authors [65,66,349]. In the model, BICs with higher Si self-interstitial content have lower energy, and thus are energetically more favorable. These authors conclude then that the formation of BICs, at least for these experimental conditions of relatively low B concentration, takes place through a high Si self-interstitial content pathway (through B_nI_m configurations containing a large number of Si self-interstitials). Their dissolution takes places when the Si interstitial supersaturation decays close to the equilibrium value, by the emission of BI pairs and the capture of quasi-equilibrium Si interstitials.

Many groups have investigated the structure of BICs by theoretical methods. Luo and coworkers [85,86] investigated BICs configuration by TB calculations for B-B and B-I interactions, showing a good agreement with the predictions of the model proposed by Pelaz et al. These authors also found that symmetry can play a role in reducing the energy of a BIC, but this generally seems to be less important than strain improvement in the BIC. According to their model, B_nI_n clusters are favored over B_nI_m ($n \neq m$) and the formation energies of B_nI_m with $n < m$ are larger than those of B_nI_m with $n > m$. Moreover, they showed that B-vacancy clusters were not energetically favored. Using *ab initio* calculations, Liu et al. [65] determined the total energies of the different BIC configurations. Their calculated energetics also indicated that BICs with more Si self-interstitials are more stable. Moreover, they found that BIC configurations with no interstitials (such as B_2, B_3) are energetically unfavorable (they have positive energy), which was also confirmed by other authors [66,349]. Some *ab initio* calculations have assigned a rather high stability to B_3I configuration [66], whereas other authors [120,350] have considered that B_4I is the configuration that plays a crucial role in the dissolution of BICs during anneal.

In general, B clustering models only included B_nI_m configurations that contain few atoms, up to 4 B atoms and 4 interstitial defects. However, recent experiments under conditions of very high B concentrations (higher than $\sim 10^{20}$ cm^{-3}) have evidenced the formation of larger and very stable BICs [351,352]. To account for these experimental observations, the B clustering model proposed by Pelaz et al. has been extended as follows [353]: B_5I_m aggregates are proposed as unstable configurations in such a way that for low and middle B concentrations only BICs with 4 or less B atoms are formed, consistently with previous studies [348]. Only in the presence of very high B concentrations BICs could evolve toward B_nI_m configurations with $n > 5$, which are again stable in the model. Furthermore, to account for the slower BICs dissolution rate observed when large BICs are formed at high B concentrations [352], an activation energy of around 4.5 eV is established for the emission of BI from large and stable configurations [352], and around 3.7 eV for small BICs [352,354].

In spite of the increasing applications of the SPER technique, the modeling of BICs in amorphous Si has not been studied in detail. Experimental profiles evidence an immobilization of B atoms for concentrations above $\sim 2 \times 10^{20}$ cm^{-3} [22,23]. Sheet resistance measurements immediately after recrystallization are consistent with maximum levels of B activation of around $\sim 2 \times 10^{20}$ cm^{-3} [22–24]. These observations support the hypothesis of immobile BICs formation at B concentrations higher than that limit value, at the same time that lower B concentrations show B diffusion in amorphous Si during recrystallization [22,23,355]. By using CMD calculations, Mattoni and Colombo have characterized the formation kinetics of some BICs during recrystallization and found that B_2I, B_3I and B_4I_2 configurations could play the major role in the evolution of recrystallized B-doped Si [356]. The kinetics of the nucleation of BICs in amorphous Si is generally not modeled in detail. In turn, it is usually assumed as the initial conditions after SPER that BICs appear above 2×10^{20} cm^{-3} in the most stable configurations compatible with the energetics included in Figure 27 [353].

From the point of view of process simulators, the large number of B_nI_m configurations leads to a large number of reactions (Eqs. (24) and (25) for the various n and m values) that should be implemented in order to predict the electrically active dopant distribution resulting from ion implantation and annealing processes. Some simplified models that considered a reduced number of relevant interactions in the process (in contrast to the extensive reaction paths shown in Fig. 27) have been reported and implemented in continuum simulators. Thus, Lilak et al.

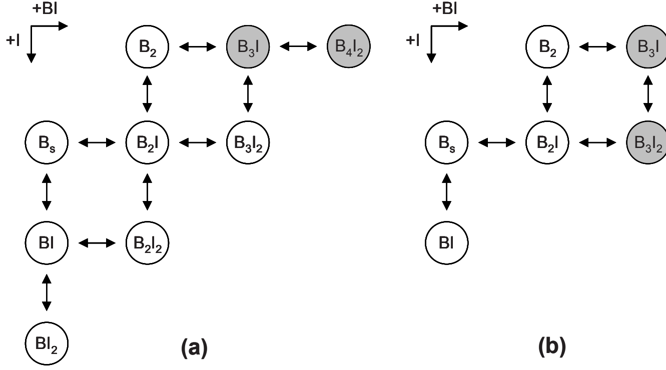

Fig. 28. Scheme of reactions for simplified B clustering models used in continuum simulators reported by (a) Lilak et al. [357] and (b) Schermer et al. [358]. Dominating BICs are marked with grey circles.

only considered interactions included in Figure 28a and assumed B_3I and B_4I_2 as dominating configurations for intense anneals [357]. Schermer et al. proposed an even more simplified model (shown in Fig. 28b) in which the configurations B_2 and B_2I serve as transition states for the formation of B_3I and B_3I_2, considered as the most stable configurations in the model [358]. These authors assumed temperature-dependent formation energies for the two dominant configurations B_3I and B_3I_2.

6.2.2 As clusters

At high concentrations ($>10^{20}$ cm^{-3}), implanted As atoms may undergo electrical deactivation [185] and TED [15,185,325,332] during post-implantation thermal treatment, as it is shown in Figure 29. In highly As-doped Si regions, the concentration of free electrons tends to saturate at the level of approximately 2×10^{20} cm^{-3} [343,359]. Clustering of the dissolved As atoms is commonly accepted as the phenomenon responsible for the electrically inactive, unprecipitated dopant in Si. An early DFT study ascribed As deactivation to the formation of As_4V complex [360]. In the mid-1990's, Rousseau and coworkers demonstrated experimentally that electrical deactivation of an As layer leads to a Si self-interstitial ejection that results in TED [9]. This work together with subsequent studies strongly suggested that As deactivates forming As-vacancy complexes and ejecting Si self-interstitials [27,359]. Additional experimental evidences for the role of As-vacancy complexes in deactivation have come from the identification of these complexes by positron annihilation spectroscopy in electrically deactivated As layers [361]. Several DFT studies have also confirmed the apparent stability and electrical inactivity of As-vacancy complexes [61,362,363].

Based on experimental data [27,359,361] and theoretical calculations [61,360,363], Pinacho et al. [339] developed a simplified model for As clustering. The total energies of the relevant As clusters as well as the reported cluster formation path driving As deactivation are indicated in Figure 30. They included the formation of electrically neutral

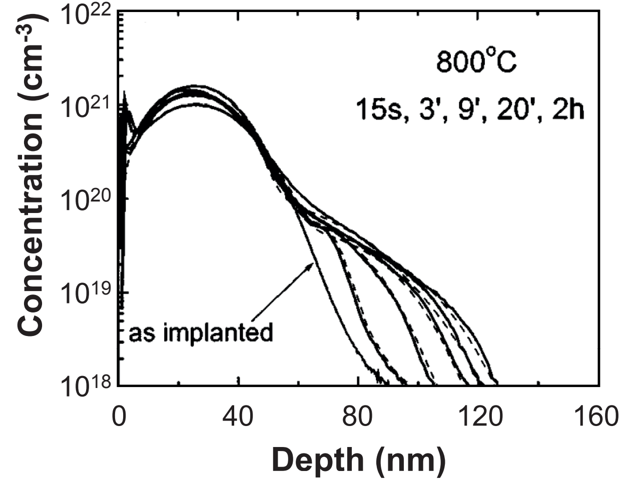

Fig. 29. Experimental As profiles for 35 keV, 5×10^{15} cm^{-2} As implants annealed at 800 °C for different times. Continuous and dashed lines correspond to measurements and simulations, respectively. During post-implant anneals the As profiles show a characteristic immobile peak associated to As clustering as well as some broadening associated to As TED (from Ref. [15]).

As_nV_m clusters, which are agglomerates formed by n As atoms and m vacancies. They did not include clusters of As combined with self-interstitials, As_nI_m, since most of the calculations reported in the literature at that time considered all As_nI_m complexes to be unstable [61,360,363]. For high enough As concentrations there exists a high probability of several As atoms being located close to each other. Thus, As deactivation is considered to be due to the bulk formation of stable As_nV clusters by the ejection of a Si self-interstitial (Eq. (28)). This makes the process highly dependent on As concentration when several As atoms are neighbors, as it has been experimentally observed [359]. The kinetics of As deactivation/activation is controlled by the growth/shrinkage of the As_nV_m clusters through the trapping/emission of mobile species (V, I, AsV, AsI), described by the following reactions:

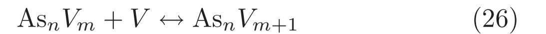

$$\mathrm{As}_nV_m + V \leftrightarrow \mathrm{As}_nV_{m+1} \quad (26)$$

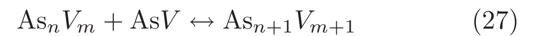

$$\mathrm{As}_nV_m + \mathrm{As}V \leftrightarrow \mathrm{As}_{n+1}V_{m+1} \quad (27)$$

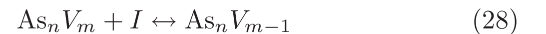

$$\mathrm{As}_nV_m + I \leftrightarrow \mathrm{As}_nV_{m-1} \quad (28)$$

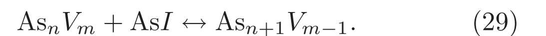

$$\mathrm{As}_nV_m + \mathrm{As}I \leftrightarrow \mathrm{As}_{n+1}V_{m-1}. \quad (29)$$

The reverse reaction of the last two expressions leads to the formation of an I-V pair from the bulk. The vacancy remains immobilized in the clusters whereas the interstitial is emitted alone (Eq. (28)) or combined with an As (Eq. (29)). In consequence, in both cases, the authors predict that an anomalous enhanced As diffusion can be generated.

Until recently, As deactivation has been attributed to As-vacancy complexes [61,339,360,363]. However, based on DFT calculations [340] and experimental investigations that evidenced a decrease in the density of extended {113} defects with the concentration of As [364], the possibility of As-interstitial clustering in interstitial-rich regions has been recently postulated [365]. Thus, DFT calculations

As	As_2	As_3	As_4
0	0	0	0
AsV	As_2V	As_3V	As_4V
-1.3	-3.5	-4.0	-4.5
			As_4V_2
			-7.5

↓ $As_n \rightarrow As_nV + I$

↘ $As + AsV \rightarrow As_2V$

↗ $As_nV + AsI \rightarrow As_{n+1}$

Fig. 30. Total energies (in eV) of the As_nV_m clusters reported by Pinacho et al. [339]. Arrows show the cluster formation path during As deactivation according to the model proposed by these authors. The clusters As_nV_m that are not indicated are supposed to be more unstable (higher total energy) in the model.

reported by Harrison et al. have provided a potential energy map for As agglomeration on their neutral-state (shown in Fig. 31) which demonstrated the existence of stable As-vacancy complexes as well as As-interstitial complexes [365]. Since both AsV and AsI are considered to be mobile [333,365], these authors suggested that As clustering can be mediated by both vacancies and Si self-interstitials. Moreover, due to the fact that As implantation results in an excess of Si self-interstitials, these authors stated that As-interstitial clusters will be predominant at the early stage of As cluster growth during thermal processing. As the density of Si self-interstitials decreases during annealing, the As-interstitial complexes will release Si self-interstitials, leaving defect-free As complexes. Those substitutional As agglomerates (without any interstitial or vacancy) tend to emit Si self-interstitials through the reverse reaction given by equation (28) to form As-vacancy complexes upon high temperature thermal treatments, according to experimental observations [9] and theoretical studies [339,362].

The scenario then becomes so complex that in continuum simulators diffusion and activation modeling for As has been simplified by including four main contributions to As electrical deactivation [366]. The initial level of electrical activation after recrystallization of the a-layer created by the usually self-amorphizing As implant was introduced as a parameter; a precipitation model was included to describe the formation of an SiAs phase for concentrations exceeding the solid solubility of As; an As clustering model in which four active As atoms and a vacancy form an inactive As_4V cluster was implemented to model deactivation below the solid solubility of As; finally, a segregation model was included to take into account the segregation and deactivation of As at the Si/SiO_2 interface.

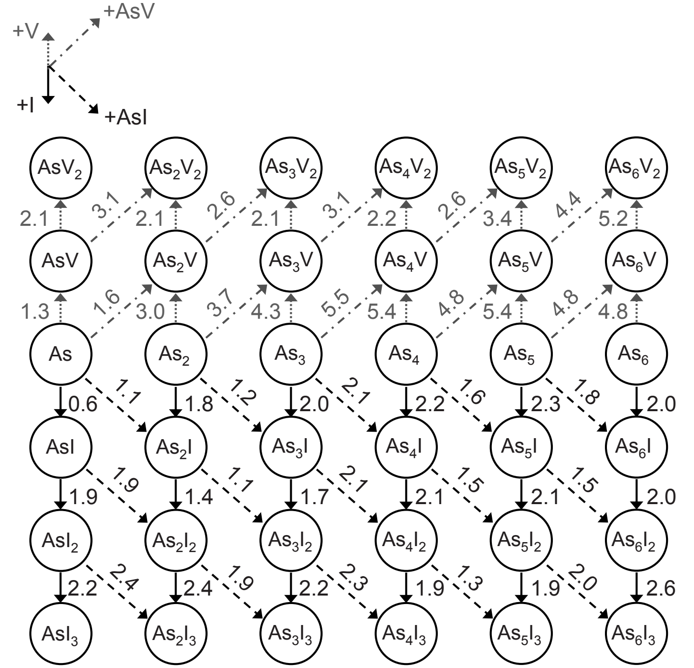

Fig. 31. Potential energy map of As-defect complexes calculated by Harrison et al. through theoretical DFT calculations [365]. The mobile defects V, AsV, I and AsI are represented by the arrows with their respective binding energies to the corresponding complexes.

7 Applications of process modeling to physical understanding and technology

The formation of ultra-shallow junctions for the future generations of ICs requires high levels of activation of dopant atoms combined with low diffusion to achieve high abruptness. Ion implantation is currently the preferred method for introducing dopants into Si for the fabrication of integrated circuits and it is expected to be used even in advanced devices such as FinFETs. Frequently high dopant doses used to form low-resistive junctions in Si are self-amorphizing. In the case of B implants, a pre-amorphizing implant is generally used (since it is difficult to amorphize with B [367]) to take the advantages of the enhanced dopant activation during low-temperature SPER with minimal diffusion [266]. Proper regrowth and removal of EOR defects are imperative to optimize device performance.

In order to obtain predictive simulations all models described in previous sections (for defect evolution, dopant-interactions, etc.) must be taken into account simultaneously. In this section we present some examples of physically-based simulations that provide understanding into the physical mechanisms involved in the processes, giving clues for process optimization.

7.1 B redistribution after SPER: clarifying B uphill diffusion

When high B fluences are implanted in pre-amorphized Si, it has been experimentally observed that B atoms in the region of medium B concentrations ($\sim 10^{19}$–10^{20} cm^{-3}) move toward higher B concentration regions during the early stages of post-SPER anneals [22,23,355,368]. This displacement against the B concentration gradient (the

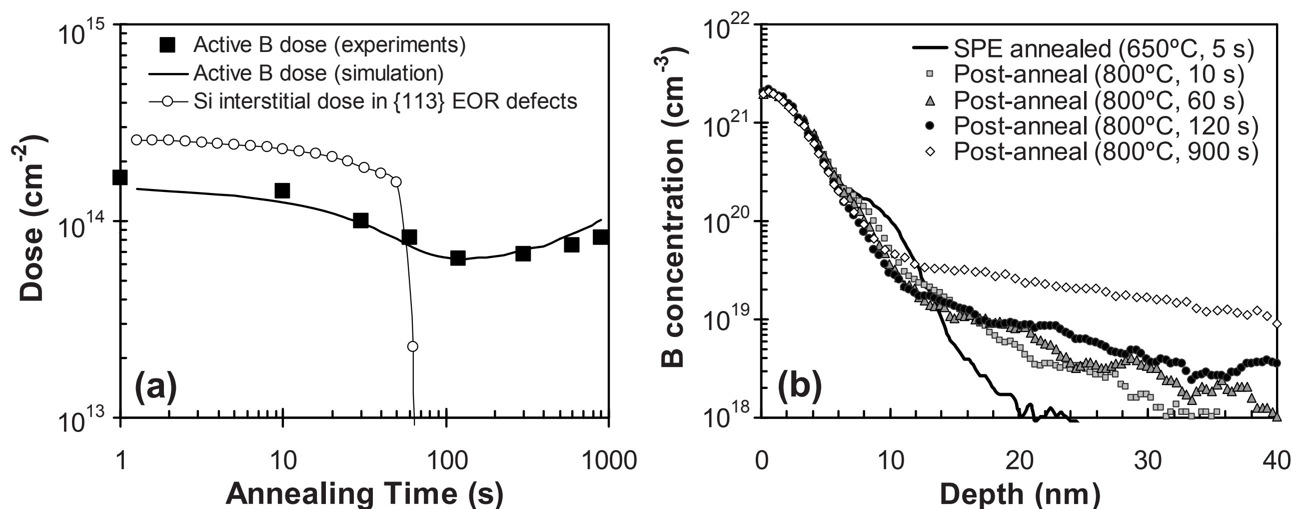

Fig. 32. (a) Simulated time evolution of the active B and the Si self-interstitials stored in small clusters and {113} defects, at the EOR region, during a 800 °C post-SPER annealing of a 0.5 keV, 1×10^{15} cm^{-2} B implant into a ∼50 nm thick a-layer. Si was pre-amorphized with a 30 keV, 1×10^{15} cm^{-2} Ge implant and annealed at 650 °C for 5 s (SPER). Experimental data for the active B dose are taken from reference [23]. (b) Evolution of the simulated B profile during annealing at 800 °C after SPER for the same conditions. B deactivation and uphill diffusion occurs while small clusters and {113} EOR defects are present.

so-called "uphill diffusion") does not occur when the same B fluences are implanted in crystalline Si [368].

Atomistic simulations have helped to clarify the physical mechanisms involved in this phenomenon. KMC simulations show that for a 0.5 keV, 1×10^{15} cm^{-2} B implant in crystalline Si around 90% of the implanted B atoms are initially immobilized in BICs after the implant [369], consistently with reported experimental observations [370]. On the contrary, in pre-amorphized Si, after the SPER process B is electrically active up to concentrations ∼2–3×10^{20} cm^{-3} [22–24], and thus, about ∼35% of the B atoms are susceptible to be moved. Moreover, the SPER process leaves Si self-interstitial defects at the EOR region that may be released and interact with substitutional B atoms.

A better understanding of the phenomenon of uphill diffusion in pre-amorphized Si can be obtained from the simultaneous analysis of the evolution of the electrically active B atoms and the redistribution of the B profile. Simulations and experiments based on a 0.5 keV, 1×10^{15} cm^{-2} B implant in a ∼55 nm thick pre-amorphized layer (created by a Ge implant) indicate that during a 800 °C post-SPER anneal B progressively deactivates until it reaches a minimum at ∼100 s, and afterwards B reactivates, as it is illustrated in Figure 32a. Simulations show that the observed B deactivation occurs while {113} defects at the EOR region exist. When these defects disappear or evolve to very stable configurations, such as dislocation loops, BICs cannot longer be maintained and they dissolve (i.e., B reactivates). The analysis of the evolution of the B profile during post-SPER annealing at 800 °C (shown in Fig. 32b) indicates that for B concentration values between 1.5×10^{19} and 2×10^{20} cm^{-3} a progressive displacement of the B profile toward the surface (uphill diffusion) occurs. This displacement takes place at the same time that EOR defects are emitting Si self-interstitials and a fraction of B deactivates. Later on the anneal the amount of B in the high concentration region decreases at the same time that the dose in the tail region increases significantly (as it occurs for instance for a 900 s anneal, included in Fig. 32b). These last observations are consistent with normal "down-hill" diffusion, in agreement with experimental data [23].

Atomistic KMC simulations have let to clarify the physical mechanisms involved in the phenomenon of uphill diffusion by running theoretical simulations in which the contributions of different mechanisms were artificially separated [369]. Firstly, when the evolution of the B profile was theoretically simulated without residual EOR damage beyond the a/c interface only normal B down-hill diffusion was observed. This fact indicates that Si self-interstitial EOR defects are necessary to observe uphill diffusion. Secondly, when the initial B profile was set in a uniform background of Si self-interstitials (thus, a Si interstitial supersaturation exists but not a gradient of Si self-interstitials) some uphill diffusion occurred. This indicates that the gradient of Si self-interstitials toward the surface may favor uphill diffusion, but it is not necessary. Finally, when the initial B profile (just after SPER) was considered fully active, at these high B concentrations BICs formed very quickly in the presence of EOR defects, leading to similar deactivation levels as in the case of pre-existing BICs that result from SPER. In consequence, an analogous B redistribution to the reference simulation (Fig. 32b) was obtained. However, when the formation of BICs was inhibited in the simulations while maintaining EOR defects, the B profile only experienced diffusion in the direction of the B concentration gradient, i.e. toward the tail region. This means that B clustering plays a role in B uphill diffusion acting as a trap for mobile B atoms. From all these observations it was concluded that B uphill diffusion needs the presence of an initially

high substitutional B concentration along with a Si interstitial supersaturation and a trap for mobile B, such as BICs. The presence of a Si interstitial supersaturation is required not only to cause B diffusion but also to stabilize BICs [371] and keep them acting as a trap for B atoms. Thus, the picture provided by simulations for the process of uphill diffusion could be summarized as follows: the Si interstitial supersaturation set by the EOR defects interacts with B atoms left in substitutional positions during the regrowth and form mobile interstitial B pairs that diffuse; these mobile B atoms can interact with pre-existing BICs in the high concentration region where B is trapped during BICs growth; this causes the increase of the total B concentration in the high concentration region, with the apparent uphill diffusion and B deactivation.

7.2 Understanding and optimization of B pocket activation

Highly active pockets or "halos" are needed to improve the capability to control SCE in Complementary-MOSFET processing [372]. Experiments have evidenced a worse SCE control in n-MOSFETs in which low temperature SPER was used for the activation of the extension regions, alternatively to other anneal treatments such as spike anneal [373]. In n-MOSFETs, the pocket typically consists of a medium energy (6–15 keV), low dose (3.5×10^{13}–1×10^{14} cm^{-2}) B implant followed by a spike anneal (typically in the order of 1100 °C) to fully activate the B pocket profile. Afterwards, the S/D extensions are formed by a typically high-dose low-energy self-amorphizing As implant, resulting in an EOR damage region which locally overlaps the low concentration B pocket profile previously activated.

Atomistic simulations can provide insight into the physics as a prior step to propose possible technological solutions. In order to understand the deactivation of the B pocket profiles, we performed atomistic KMC simulations in which we considered the EOR defects coming from an amorphizing implant locally overlapping with a typical B pocket profile, as it is shown in Figure 33. Upon annealing we observe the formation of a peak in the B profile within the EOR region as well as some B diffusion in the tail region of the B profile. Simulations indicate that the B peak is associated to BIC formation and that only ∼33% of the initially active B atoms located within the EOR region remains active after the 750 °C, 10 s anneal. From an n-MOSFET perspective, this is very important as it shows that a significant B pocket deactivation occurs close to and just beyond the extension profile, as confirmed also experimentally [373]. This leads to a deterioration of the capability of B pocket profiles to control SCE.

The dissolution of BICs formed within the region overlapping EOR defects requires intense thermal budgets [373]. However, simulations have indicated that the anneals required to fully activate the B pocket profile are in the order of the anneal times that lead to undesired B deactivation and diffusion in p-MOSFET extension regions formed by high-dose low-energy B implants in pre-

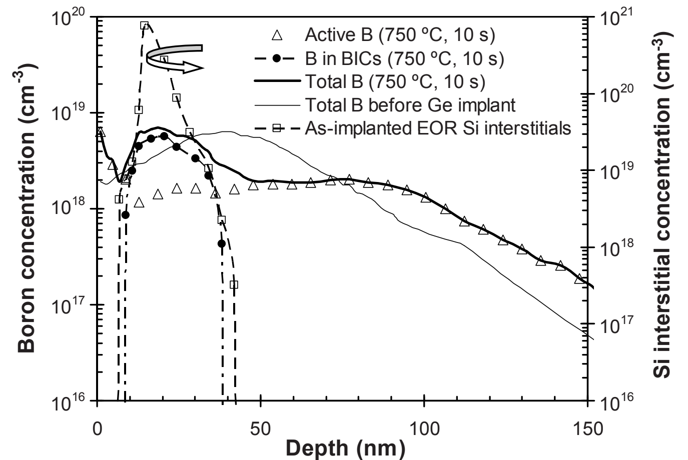

Fig. 33. Simulated depth profiles of initial total B (fully active) and active, clustered, and total B concentrations after a low temperature 750 °C 10 s anneal, for a 10 keV, 3.5×10^{13} cm^{-2} B implant fully activated by high-temperature spike anneal in the presence of EOR damage. The EOR Si interstitial damage profile (also included in the figure) was created by an amorphizing 8 keV, 2×10^{14} cm^{-2} Ge implant (a/c depth ∼12 nm), which could represent a self-amorphizing As extension implant. B clustering only occurs in the region where the high concentration of Si interstitials overlaps B profile.

amorphized Si [373]. This poses a difficult trade-off to simultaneously optimize n- and p-MOSFET devices.

Since the formation of BICs (B deactivation) only occurs in the region that overlaps with EOR defects, a possible technological solution consists of adding a Si or Ge pre-amorphizing implant to the process flow to create a deeper a-layer in such a way that the EOR defects would be moved away from the extension profile. With a deeper EOR defect band the localized B deactivation would also be deeper, and so the pocket close to the extension would remain active. Thus SCE control would be improved, although problems related to leakage currents due to EOR defects would still remain. Another possible technological solution consists of increasing the implanted B pocket in order to compensate for the deactivated dose [373]. Essentially the concentration ratio between B and Si self-interstitials becomes higher in the EOR region as the implanted B dose is raised, since the Si self-interstitial concentration is fixed by the amorphizing implant. Therefore, the B pocket profile is more efficient in terms of the ratio of active to inactive dopant. However, the disadvantage of this approach is the presence of more BICs in absolute terms that may contribute to non-ideal leakage in a similar way that EOR defects do.

7.3 Issues on FinFET devices: a challenge in 3D

Multigate metal-oxide-semiconductor devices such as FinFETs are a promising scaling approach due to excellent SCE and leakage control [374]. A schematic of a FinFET device is shown in Figure 34. Due to the 3D nature of the FinFET geometry and the feature size in the nanoscale,

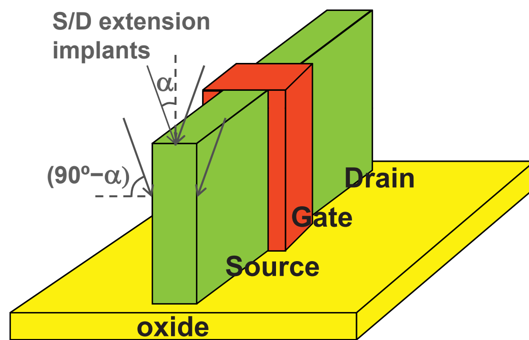

Fig. 34. Schematic of a FinFET device. S/D extensions implants typically used to incorporate dopants in the fin are marked. Note that the sidewalls of the fin are implanted with a single fluence with implant angle (90°-α) whereas the top of the fin is implanted twice with implant angle α.

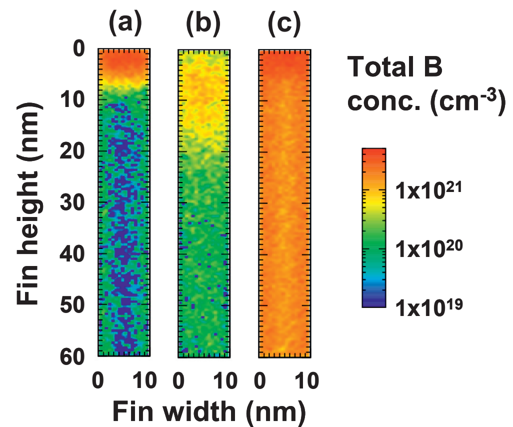

Fig. 35. 2D dopant profile of a 10 nm wide 10 nm high fin implanted with doses of 1×10^{15} cm^{-2} B at (a) 0.5 keV, 10°; (b) 2 keV, 10°; and (c) 0.5 keV, 45°. A highly non-conformal dopant profile is obtained for 10° implants.

experimental characterization techniques are challenging and atomistic simulations become essential tools for device optimization. For junction formation, ion implantation is a leading candidate as the means to introduce dopants into the fin. However, FinFETs suffer from specific challenges that need to be solved for making these devices competitive for IC manufacturing. One of the main challenges is the efficient dopant incorporation into the sidewalls of these vertical structures after the S/D extensions implants into the fin, as it directly affects the access resistance that defines the dynamic performance of FinFETs [375,376]. However, dopant incorporation in the fin is limited by several aspects mainly related to the particular geometry of the fin and the requirements for implant conditions [377]. Tilted implants are used for that purpose but there is an angle restriction to avoid shadowing during implant of dense fin pitches [377,378].

As an example, Figure 35 illustrates the simulated dopant distribution obtained for (a) 0.5 keV, 1×10^{15} cm^{-2} at 10°, (b) 2 keV, 1×10^{15} cm^{-2} at 10° and (c) 0.5 keV, 1×10^{15} cm^{-2} at 45°. For 10° implants both the conformality of the dopant distribution and the amount of dopants incorporated into the fin are poor. Due to geometrical considerations, the irradiated dose on the sidewalls is a factor of $1/2\tan(10°) \approx 0.08$ of the irradiated dose at the top surface, which makes conformality difficult. In addition, ion backscattering also contributes to the inefficient dopant incorporation in the sidewalls (80° implant angle). The ion loss is more pronounced for 0.5 keV (90% of the incident ions are backscattered and only 10% retained) than for 2 keV (30% of the incident ions are retained, 65% are backscattered and there is an additional effect of about 5% of the ions that are lost because their trajectories escape from the fin). For 45° implants, the conformality and the dopant incorporation are better since $1/2\tan(45°) = 1/2$ and about 60% of incident ions are retained. The inefficient incorporation of dopants into the sidewalls for low implant angles has been demonstrated by experimental analysis performed in blanket wafers [379] and fin structures [45]. The loss of dopants when using higher energy 45° implants in narrow fins has been confirmed by the increase in the resistance of the fins as implant energy is increased [45,377].

Amorphization and recrystallization in FinFETs has also become a pressing concern [377,380]. Experiments show that recrystallization is not perfect since line defects along {111} planes are formed during the regrowth of the amorphized body [380] which degrades device performance [45,377]. In Fig. 36 we illustrate different snapshots corresponding to CMD simulations of the regrowth of a 14 nm thick fin structure oriented along $\langle 110 \rangle$. The top amorphous phase is built by the accumulation of IV pairs. A crystalline seed is left at the bottom so that it can trigger SPER. Crystal recovery starts from the bottom, since the rest of the device body is surrounded by amorphous material. Thus, regrowth advances from the a/c interface toward the amorphous phase, starting from the bottom at the middle of the fin, but it is halted at the vertical interfaces because "amorphous" defects close to the a/c interfaces are more stable [378]. Then {111} planes start to form as the regrowth in that direction is slower than along $\langle 110 \rangle$ and $\langle 100 \rangle$ directions [309], preventing a clean regrowth. Implants at elevated temperatures may be needed to prevent amorphization.

8 Conclusions and future perspectives

The goal of process modeling is to provide physical understanding and simulation tools to help the development and optimization of device fabrication. Most important and challenging in the area of front-end process simulation is the modeling of ultra-shallow junction formation, which starts from very low energy implant and especially focuses on the thermal annealing. This involves phenomena like amorphization, nucleation and growth of intrinsic extended defects, dopant diffusion and formation of various cluster types. Continuous research during the last decades has led to a deep knowledge about the interactions of dopants, other impurities and intrinsic defects in Si [192]. This has allowed the development of models that

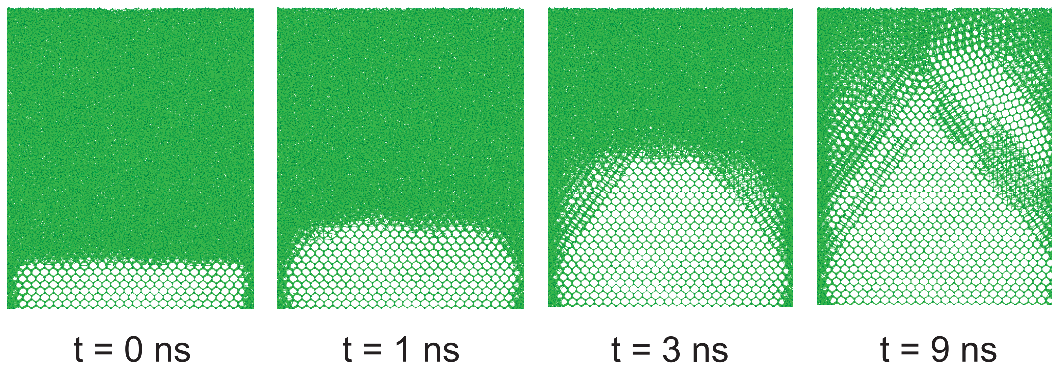

Fig. 36. CMD simulations of the evolution of a 14 nm fin structure. A covering a-layer surrounds the Si fin. A crystalline seed is left at the bottom to promote SPER. Poor regrowth causes {111} twin boundaries and polycrystalline Si.

provide a comprehensive description of diffusion and activation of implanted dopants in a broad technological window. Nevertheless, many issues remain unsolved.

In addition to the advances in the understanding of the physics involved in junction formation, the explosion of computer resources at an affordable price has greatly contributed to the progress in process simulation. Calculations that were prohibitive a decade ago are now affordable and open interesting possibilities for process simulation using detailed atomistic methods. Large memory cells and improved speed performance in multi-processor computers allows to deal with larger or more refined systems or to follow the dynamics of the system for longer times. Although continuum models continue being the mainstream in process simulation, atomistic KMC models are beginning to play an important role, both as direct simulation approaches for front-end processes and as a pathway to improve continuum models. *Ab initio* methods are also acquiring more relevance because the lack of free parameters makes them very useful for the modeling of new materials. In addition, the augmented computer power allows the use of larger simulation cells and fewer approximations to solve the Schrödinger equation, which make their results more reliable.

Process simulation capabilities must evolve to encompass processes, geometries and materials considered for present and future devices. Therefore, trends in device technology drive the requirements for process modeling. Scaling of transistors not only demands higher degree of accuracy but also may require new models for effects that were neglected in previous technology nodes. As the device dimensions are reduced and millisecond anneals are almost diffusion-less, the accurate prediction of the as-implanted 3D dopant and damage distributions is becoming more relevant. BCA-KMC based models maintain a good compromise between speed and accuracy. BCA damage models have been improved to describe the direct formation of *a*-pockets, as it occurs in molecular implants. The use of amorphizing implants followed by SPER has motivated the development of detailed models that account for amorphization and regrowth, including dynamic annealing during implant. The influence of crystal orientation and impurities on SPER needs to be considered. Residual damage is a pressing concern in low power applications. Modeling of the formation and dissolution of all kind of intrinsic extended defects is important to optimize the thermal budget for the complete defect removal while minimizing dopant diffusion and maximizing dopant activation. Particularly challenging is the physical modeling of the transition between {113} defects and dislocation loops.

Refinement of models for dopant-defect interactions continues being a key factor for optimizing transistor fabrication, pushing the limits of scaling traditional planar devices, and evaluating process issues in alternative device architectures. The interactions between defects and dopants, particularly for B and to some extend also for As, in crystal Si have been extensively studied, both at experimental and theoretical level. Other dopants have been also explored [192]. Impurities, such as C, F, N have received some attention because they can be used advantageously (defect engineering) in "cocktail implants" combined with dopants to optimize junction formation [381]. The dynamics of dopants in amorphous Si are not as well understood as it is in crystal Si. The study of dopants and impurities in general, in amorphous Si is much more complex than in crystal Si. The inherent diversity of local environments in an amorphous cell makes theoretical studies difficult, and the window for experiments is rather narrow because SPER occurs quite fast and at relatively low temperature. Although there are some empirical and simplistic models that account for some experimental observations, they lack of the physical basis that encompasses the rich phenomenological observations of dopants in amorphous Si [348,382,383]. For instance, as the initial condition after regrowth most models assume that B clusters exist above 2×10^{20} cm^{-3} [348]. However, it has been demonstrated that the threshold concentration for B clustering in amorphous Si increases when the regrowth occurs at high temperatures and that B diffuses in amorphous Si [384]. Other dopants, such as As, do not diffuse appreciably in amorphous Si [385] but they exhibit a strong segregation during regrowth, so that the dopant profile after annealing significantly differs from the as-implanted one [386]. It would be necessary to develop physically based models that can provide the understanding and the clues required

to optimize electrically active dopant profiles when SPER is involved. Being dopant profiles ever-shallower, the effect of interfaces is becoming increasingly important and needs to be properly simulated [387,388]. The segregation and trapping of impurities at interfaces needs to be modeled for all kinds of dielectrics, including high-κ material stacks, taking the influence of N, C, F, Ge, and metallic impurities and of knock-on oxygen into account. Moreover, as the mechanical stress engineering plays a crucial role to enhanced charge carrier mobility, all these models on diffusion, clustering, and dopant activation must take into account locally the effect of the mechanical stress [389–392]. The presence of dopants, defects and clusters may itself alter the stress in Si. Typically, this is only taken into account for high Ge or C concentration in Si, but may be equally important for high concentration of dopants or dopant clusters.

For new device architectures, such as FinFETs, it is necessary to assess existing processes and probably develop new ones to address new issues that arise in non planar structures. Although ion implantation remains the main candidate to introduce dopants, deposition techniques and plasma doping are strong contenders since they have the potential for conformal doping. 3D simulations of these processes will be needed for advanced device architectures. The incorporation of other materials to substitute Si in the channel, such as Ge or III–V compounds, is promoting a number of studies to establish models and parameters that describe accurately the behavior of dopants and defects in these materials during the process integration flow. Research on new materials could build on the experiences and methods developed in Si. Even for a material such as Ge, similar to Si in many aspects, the understanding even of basic aspects is very rudimentary [28]. It is known that Ge amorphizes much more easily than Si but the damage generation mechanisms in Ge are not clear. While self-interstitials play a dominant role in the evolution of intrinsic extended defects and in dopant diffusion and activation in Si, vacancies are attributed a dominant role in Ge. Some calculations have been performed, but the map of interactions in Ge is reduced to a few defects. It will be a challenge to collect all the information needed for predictive process modeling in time should Ge become an alternative to Si in future technology nodes. These difficulties are even bigger for other high-mobility channels like III–V compounds.

We want to acknowledge funding from the Spanish Goverment under project TEC2008-06069, and from the Junta de Castilla y León under Project VA011A09.

References

1. International Technology Roadmap for Semiconductors, `http://www.itrs.net/`
2. E. Chason, S.T. Picraux, J.M. Poate, J.O. Borland, M.I. Current, T.D. de la Rubia, D.J. Eaglesham, O.W. Holland, M.E. Law, C.W. Magee et al., J. Appl. Phys. **81**, 6513 (1997)
3. M.J. Caturla, T.D. de la Rubia, L.A. Marqués, G.H. Gilmer, Phys. Rev. B **54**, 16683 (1996)
4. S.E. Donnelly, R.C. Birtcher, V.M. Vishnyakov, G. Carter, Appl. Phys. Lett. **82**, 1860 (2003)
5. I. Santos, L.A. Marqués, L. Pelaz, P. López, M. Aboy, J. Barbolla, Mater. Sci. Eng. B **124–125**, 372 (2005)
6. S. Prussin, D.I. Margolese, R.N. Tauber, J. Appl. Phys. **57**, 180 (1985)
7. W.K. Hofker, H. Werner, D.P. Oosthoek, H.A.M. de Grefte, Appl. Phys. **2**, 165 (1973)
8. D.J. Eaglesham, P.A. Stolk, H.J. Gossmann, J.M. Poate, Appl. Phys. Lett. **65**, 2305 (1994)
9. P.M. Rousseau, P.B. Griffin, J.D. Plummer, Appl. Phys. Lett. **65**, 578 (1994)
10. P.A. Stolk, H.J.G.D.J. Eaglesham, D.C. Jacobson, C.S. Rafferty, G.H. Gilmer, M. Jaraiz, J.M. Poate, H.S. Luftman, T.E. Haynes, J. Appl. Phys. **81**, 6031 (1997)
11. L. Pelaz, M. Jaraiz, G.H. Gilmer, H.J. Gossmann, C.S. Rafferty, D.J. Eaglesham, J.M. Poate, Appl. Phys. Lett. **70**, 2285 (1997)
12. N.E.B. Cowern, G. Mannino, P.A. Stolk, F. Roozeboom, H.G.A. Huizing, J.G.M. van Berkum, F. Cristiano, A. Claverie, M. Jaraiz, Phys. Rev. Lett. **82**, 4460 (1999)
13. S. Whelan, V. Privitera, G. Mannino, M. Italia, C. Bongiorno, A. La-Magna, E. Napolitani, J. Appl. Phys. **90**, 3873 (2001)
14. S.C. Jain, W. Schoenmaker, R. Lindsay, P.A. Stolk, S. Decoutere, M. Willander, H.E. Maes, J. Appl. Phys. **91**, 8919 (2002)
15. S. Solmi, M. Ferri, M. Bersani, D. Giubertoni, V. Soncini, J. Appl. Phys. **94**, 4950 (2003)
16. K. Mistry, M. Armstrong, C. Auth, S. Cea, T. Coan, T. Ghani, T. Hoffmann, A. Murthy, J. Sandford, R. Shaheed et al., in *Symposium on VLSI Technology Digest of Technical Papers* (2004), pp. 50–51
17. D. Schroder, IEEE Trans. Elec. Dev. **44**, 160 (1997)
18. A. Argawal, A.T. Fiory, H.J. Gossmann, C.S. Rafferty, P. Frisella, Mater. Sci. Semicond. Process. **1**, 237 (1998)
19. R. Lindsay, B. Pawlak, J. Kittl, K. Henson, C. Torregiani, S. Giangrandi, R. Surdeanu, W. Vandervorst, A. Mayur, J. Ross et al., Mater. Res. Soc. Symp. Proc. **765**, D7.4.1 (2003)
20. M.P. Smith, R.A. McMahon, K.A. Seffen, D. Panknin, M. Voelskow, W. Skorupa, *Thermal and Stress Modeling for Flash Lamp Crystallization of Amorphous Silicon Films*, in *Mat. Res. Soc. Symp. Proc.* (2006), Vol. 910, p. A21
21. A. Colin, P. Morin, F. Cacho, H. Bono, R. Beneyton, M. Bidaud, D. Mathiot, E. Fogarassy, Mat. Sci. Eng. B **154–155**, 31 (2008)
22. J.Y. Jin, J. Liu, U. Jeong, S. Mehta, K. Jones, J. Vac. Sci. Technol. B **20**, 422 (2002)
23. W. Lerch, S. Paul, J. Niess, F. Cristiano, Y. Lamrani, P. Calvo, N. Cherkashin, D.F. Downey, E.A. Arevalo (2004)
24. B.J. Pawlak, R. Surdeanu, B. Colombeau, A.J. Smith, N.E.B. Cowern, R. Lindsay, W. Vandervorst, B. Brijs, O. Richard, F. Cristiano, Appl. Phys. Lett. **84**, 2055 (2004)
25. V. Privitera, A.L. Magna, G. Fortunato, M. Camalleri, A. Magri, F. Simon, B.G. Svensson, Mat. Sci. Eng. B **114–115**, 92 (2004)
26. Y. Takamura, S.H. Jain, P.B. Griffin, J.D. Plummer, J. Appl. Phys. **92**, 230 (2002)

27. Y. Takamura, P.B. Griffin, J.D. Plummer, J. Appl. Phys. **92**, 235 (2002)
28. C. Claeys, E. Simoen, *Germanium-based Technologies: From Materials to Devices* (Elsevier, Amsterdam, 2007)
29. N. Goel, D. Heh, S. Koveshnikov, I. Ok, S. Oktyabrsky, V. Tokranov, R. Kambhampati, M. Yakimov, Y. Sun, P. Pianetta et al., in *IEDM Technical Digest* (2008)
30. T. Ghani, M. Armstrong, C. Auth, M. Bost, P. Charvat, G. Glass, T. Hoffmann, K. Johnson, C. Kenyon, J. Klaus et al., *A 90 nm high volume manufacturing logic technology featuring novel 45 nm gate length strained silicon CMOS transistors*, in *IEDM Technical Digest* (2003)
31. M.J. Aziz, Appl. Phys. Lett. **70**, 2810 (1997)
32. A. Pakfar, Mat. Sci. Eng. B **89**, 225 (2002)
33. N.E.B. Cowern, Phys. Rev. Lett. **99**, 155903 (2007)
34. C. Ahn, N. Bennett, S.T. Dunham, N.E.B. Cowern, Phys. Rev. B **79**, 073201 (2009)
35. A.L. Magna, P. Alippi, V. Privitera, G. Fortunato, M. Camalleri, B. Svensson, J. Appl. Phys. **95**, 4806 (2004)
36. A.L. Magna, P. Alippi, V. Privitera, G. Fortunato, Appl. Phys. Lett. **86**, 161905 (2005)
37. A.L. Magna, V. Privitera, G. Fortunato, M. Cuscuna, B.G. Svensson, E. Monakhov, K. Kuitunen, J. Slotte, F. Tuomisto, Phys. Rev. B **75**, 235201 (2007)
38. L.A. Marqués, L. Pelaz, P. López, M. Aboy, I. Santos, J. Barbolla, Mat. Sci. Eng. B **124–125**, 72 (2005)
39. FLOOPS (FLorida Object Oriented Device and Process Simulator), `http://www.flooxs.tec.ufl.edu/`
40. M.E. Law, S.M. Cea, Comput. Mat. Sci. **12**, 289 (1998)
41. C. Rafferty, R.K. Smith, CMES-Comp. Model. Eng. **1**, 151 (2000)
42. T. Noda, W. Vandervorst, S. Felch, V. Parihar, C. Vranckena, S. Severi, A. Falepin, T. Janssens, H. Bender, B.V. Daele et al., IEDM Technical Digest (2006), p. 1
43. K.R.C. Mok, B. Colombeau, F. Benistant, R.S. Teo, S.H. Yeong, B. Yang, M. Jaraiz, S.S. Chu, IEEE Transac. Electron Devices **54**, 2155 (2007)
44. M. Jaraiz, P. Castrillo, R. Pinacho, J.E. Rubio, IEDM Technical Digest (2007), p. 951
45. L. Pelaz, R. Duffy, M. Aboy, L.A. Marqués, P. López, I. Santos, B.J. Pawlak, M.J.H. van Dal, B. Duriez, T. Merelle et al., in *IEDM Technical Digest* (2008), p. 535
46. M. Jaraiz, P. Castrillo, R. Pinacho, I. Martín-Bragado, J. Barbolla, in *Simulation of Semiconductor Processes and Devices*, edited by D. Tsoukalas, C. Tsamis (Springer-Verlag, Wien, 2001), p. 10
47. L. Pelaz, L.A. Marqués, M. Aboy, P. López, J. Barbolla, Comp. Mat. Sci. **33**, 92 (2005)
48. P.E. Blöchl, E. Smargiassi, R. Car, D.B. Laks, W. Andreoni, S.T. Pantelides, Phys. Rev. Lett. **70**, 2435 (1993)
49. K. Ohno, K. Esfarjani, Y. Kawazoe, *Computational Materials Science: from ab initio to Monte Carlo methods* (Springer-Verlag, Berlin, 1999)
50. M. Born, J.R. Oppenheimer, Ann. der Physik **84**, 457 (1927)
51. D.R. Hartree, Proc. Cambridge Philos. Soc. **24**, 89 (1928)
52. V. Fock, Z. f. Physik **61**, 126 (1930)
53. J.C. Slater, Phys. Rev. **35**, 210 (1930)
54. P. Hohenberg, W. Kohn, Phys. Rev. **136**, B864 (1964)
55. W. Kohn, Rev. Mod. Phys. **71**, 1253 (1999)
56. S.J. Clark, G.J. Ackland, Phys. Rev. B **56**, 47 (1997)
57. J.L. Mercer, J.S. Nelson, A.F. Wright, E.B. Stechel, Mod. Sim. Mat. Sci. Eng. **6**, 1 (1998)
58. O.K. Al-Mushadani, R.J. Needs, Phys. Rev. B **68**, 235205 (2003)
59. F. Cargnoni, C. Gatti, L. Colombo, Phys. Rev. B **57**, 170 (1998)
60. C.S. Nichols, C.G.V. de Walle, S.T. Pantelides, Phys. Rev. B **40**, 5484 (1989)
61. M. Ramamoorthy, S.T. Pantelides, Phys. Rev. Lett. **76**, 4753 (1996)
62. W. Windl, M.M. Bunea, R. Stumpf, S.T. Dunham, M.P. Masquelier, Phys. Rev. Lett. **83**, 4345 (1999)
63. B. Sadigh, T.J. Lenosky, S.K. Theiss, M.J. Caturla, Phys. Rev. Lett. **83**, 4341 (1999)
64. J. Zhu, T.D. de la Rubia, L.H. Yang, C. Mailhiot, G.H. Gilmer, Phys. Rev. B **54**, 4741 (1996)
65. X.Y. Liu, W. Windl, M.P. Masquelier, Appl. Phys. Lett. **77**, 2018 (2000)
66. T.J. Lenosky, B. Sadigh, S.K. Theiss, M.J. Caturla, T.D. de la Rubia, Appl. Phys. Lett. **77**, 1834 (2000)
67. N.W. Ashcroft, N.D. Mermin, *Solid State Physics* (HRW International Editions, New York, 1976)
68. F. Bloch, Z. f. Physik **52**, 555 (1928)
69. L. Colombo, Ann. Rev. Mater. Res. **32**, 271 (2005)
70. W.A. Harrison, *Electronic Structure and the Properties of Solids* (Dover, New York, 1989)
71. D.J. Chadi, M.L. Cohen, Phys. Status Solidi B **68**, 405 (1975)
72. L. Goodwin, A.J. Skinner, D.G. Pettifor, Europhys. Lett. **9**, 701 (1989)
73. I. Kwon, R. Biswas, C.Z. Wang, K.M. Ho, C.M. Soukoulis, Phys. Rev. B **49**, 7242 (1994)
74. M. Tang, L. Colombo, J. Zhu, T.D. de la Rubia, Phys. Rev. B **55**, 14279 (1997)
75. M.T. Zawadzki, W. Luo, P. Clancy, Phys. Rev. B **63**, 205205 (2001)
76. L.J. Munro, D.J. Wales, Phys. Rev. B **59**, 3969 (1999)
77. C.Z. Wang, C.T. Chan, K.M. Ho, Phys. Rev. Lett. **66**, 189 (1991)
78. E.G. Song, E. Kim, Y.H. Lee, Y.G. Hwang, Phys. Rev. B **48**, 1486 (1993)
79. A. Jääskeläinen, L. Colombo, R. Nieminen, Phys. Rev. B **64**, 233203 (2001)
80. D.A. Richie, J. Kim, S.A. Barr, K.R.A. Hazzard, R. Hennig, J.W. Wilkins, Phys. Rev. Lett. **92**, 045501 (2004)
81. M. Cogoni, B.P. Uberuaga, A.F. Voter, L. Colombo, Phys. Rev. B **71**, 121203 (2005)
82. J. Kim, J.W. Wilkins, F.S. Khan, A. Canning, Phys. Rev. B **55**, 16186 (1997)
83. M. Kohyama, S. Takeda, Phys. Rev. B **51**, 13111 (1995)
84. P. Alippi, L. Colombo, Phys. Rev. B **62**, 1815 (2000)
85. W. Luo, P.B. Rasband, P. Clancy, B.W. Roberts, J. Appl. Phys. **84**, 2476 (1998)
86. W. Luo, P. Clancy, J. Appl. Phys. **89**, 1596 (2001)
87. F.H. Stillinger, T.A. Weber, Phys. Rev. B **31**, 5262 (1985)
88. J. Tersoff, Phys. Rev. Lett. **56**, 632 (1986)
89. J. Tersoff, Phys. Rev. B **38**, 9902 (1988)
90. J. Tersoff, Phys. Rev. B **39**, 5566 (1989)
91. R. Biswas, D.R. Hamann, Phys. Rev. Lett. **55**, 2001 (1985)
92. E. Kaxiras, K.C. Pandey, Phys. Rev. B **38**, 12736 (1988)
93. B.W. Dodson, Phys. Rev. B **35**, 2795 (1987)
94. J. Wang, A. Rockett, Phys. Rev. B **43**, 12571 (1991)

95. M.I. Baskes, J.S. Nelson, A.F. Wright, Phys. Rev. B **40**, 6085 (1989)
96. M.I. Baskes, Phys. Rev. B **46**, 2727 (1992)
97. T.J. Lenosky, B. Sadigh, E. Alonso, V.V. Bulatov, T.D. de la Rubia, J. Kim, A.F. Woter, J.D. Kress, Modelling Simul. Mater. Sci. Eng. **8**, 825 (2000)
98. M.Z. Bazant, E. Kaxiras, J.F. Justo, Phys. Rev. B **56**, 8542 (1997)
99. H. Balamane, T. Halicioglu, W.A. Tiller, Phys. Rev. B **46**, 2250 (1992)
100. S.T. Cook, P. Clancy, Phys. Rev. B **47**, 7686 (1993)
101. C. Krzeminski, Q. Brulin, V. Cuny, E. Lecat, E. Lampin, F. Cleri, J. Appl. Phys. **101**, 123506 (2007)
102. L.A. Marqués, L. Pelaz, P. Castrillo, J. Barbolla, Phys. Rev. B **71**, 085204 (2005)
103. P.J. Ungar, T. Takai, T. Halicioglu, W.A. Tiller, J. Vac. Sci. Technol. A **11**, 224 (1994)
104. P.J. Ungar, T. Halicioglu, W.A. Tiller, Phys. Rev. B **50**, 7344 (1994)
105. M. Posselt, F. Gao, H. Bracht, Phys. Rev. B **78**, 035208 (2008)
106. M. Posselt, F. Gao, D. Zwicker, Phys. Rev. B **71**, 245202 (2005)
107. K. Nishihira, T. Motooka, Phys. Rev. B **66**, 233310 (2002)
108. L.A. Marqués, L. Pelaz, P. López, I. Santos, M. Aboy, Phys. Rev. B **76**, 153201 (2007)
109. A. Mattoni, L. Colombo, Phys. Rev. B **78**, 075408 (2008)
110. L.A. Marqués, L. Pelaz, I. Santos, P. López, M. Aboy, Phys. Rev. B **78**, 193201 (2008)
111. T.D. de la Rubia, G.H. Gilmer, Phys. Rev. Lett. **74**, 2507 (1995)
112. K. Nordlund, M. Ghaly, R.S. Averback, M.J. Caturla, T.D. de la Rubia, J. Tarus, Phys. Rev. B **57**, 7556 (1998)
113. K.M. Beardmore, N. Grønbech-Jensen, Phys. Rev. B **60**, 12610 (1999)
114. L.A. Marqués, L. Pelaz, I. Santos, V.C. Venezia, Phys. Rev. B **74**, 201201 (2006)
115. L.M. Howe, M.H. Rainville, H.K. Haugen, D.A. Thompson, Nucl. Instrum. Methods **170**, 419 (1980)
116. S. Ihara, S. Itoh, J. Kitakami, Phys. Rev. B **58**, 10736 (1998)
117. R. Smith, M. Shaw, R.P. Webb, M.A. Foad, J. Appl. Phys. **83**, 3148 (1998)
118. T. Aoki, J. Matsuo, G. Takaoka, N. Toyoda, I. Yamada, Nucl. Instrum. Methods Phys. Res. B **206**, 855 (2003)
119. N.E.B. Cowern, D.J. Godfrey, D.E. Sykes, Appl. Phys. Lett. **49**, 1711 (1986)
120. L. Pelaz, G.H. Gilmer, H.J. Gossmann, C.S. Rafferty, M. Jaraiz, J. Barbolla, Appl. Phys. Lett. **74**, 3657 (1999)
121. M. Aboy, L. Pelaz, L.A. Marqués, P. López, J. Barbolla, R. Duffy, V.C. Venezia, P.B. Griffin, Appl. Phys. Lett. **86**, 031908 (2005)
122. J.D. Plummer, M.D. Deal, P.B. Griffin, *Silicon VLSI Technology. Fundamentals, Practice and Modeling* (Prentice Hall, 2000)
123. F. Jahnel, I. Ryssel, G. Prinke, K. Hoffmann, K. Mijller, J. Biersack, R. Henkelmann, Nucl. Instrum. Methods **182–183**, 223 (1981)
124. D.G. Ashworth, R. Oven, B. Mundin, J. Phys. D **23**, 870 (1990)
125. K. Suzuki, R. Sudo, T. Feudel, W. Fichtner, IEEE Trans. Elec. Dev. **47**, 44 (2000)
126. C. Park, K.M. Klein, A.F. Tasch, Solid State Electronics **33**, 645 (1990)
127. S. Morris, S.H. Yang, D. Lim, C. Park, K. Klein, M. Manassian, A.F. Tasch, IEEE Transactions on Semiconductor Manufacturing **8**, 408 (1995)
128. H. Goldstein, *Classical Mechanics*, 3rd edn. (Addison-Wesley, Reading, MA, 2000)
129. M.T. Robinson, I.M. Torrens, Phys. Rev. B **9**, 5008 (1974)
130. J.F. Ziegler, *Ion Implantation: Science and Technology* (Academic Press, San Diego, 1988)
131. J.J. Loferski, P. Rappaport, Phys. Rev. **98**, 1861 (1955)
132. L.A. Miller, D.K. Brice, A.K. Prinja, S.T. Picraux, Phys. Rev. B **49**, 16953 (1994)
133. M. Sayed, J.H. Jefferson, A.B. Walker, A.G. Cullis, Nucl. Instrum. Methods Phys. Res. B **102**, 232 (1995)
134. M. Mazzarolo, L. Colombo, G. Lulli, E. Albertazzi, Phys. Rev. B **63**, 195207 (2001)
135. E. Hölmstrom, A. Kuronen, K. Nordlund, Phys. Rev. B **78**, 045202 (2008)
136. SRIM documentation, `www.srim.org`
137. UT-MARLOWE documentation, `http://homer.mer.utexas.edu/`
138. J.M. Hernández-Mangas, J. Arias, L. Bailón, M. Jaraíz, J. Barbolla, J. Appl. Phys. **91**, 658 (2002)
139. K. Nordlund, N. Runeberg, D. Sundholm, Nucl. Instrum. Methods Phys. Res. B **132**, 45 (1997)
140. A. Sommerfeld, Z. f. Physik **77**, 722 (1931)
141. G. Molière, Z. f. Naturforsch **A2**, 133 (1947)
142. W. Lenz, Z. f. Physik **77**, 713 (1947)
143. J.F. Ziegler, J.P. Biersack, U. Littmark, *The Stopping and Range of Ions in Solids* (Pergamon, New York, 1985)
144. L. Rubin, J. Poate, The Industrial Physicist **9**, 12 (2003)
145. A. Chettah, H. Kucal, Z.G. Wang, M. Kac, A. Meftah, M. Toulemonde, Nucl. Instrum. Methods Phys. Res. B **267**, 2719 (2009)
146. O.B. Firsov, Zh. Éksp. Teor. Fiz. **34**, 1517 (1959)
147. O.B. Firsov, Sov. Phys. JETP **9**, 1076 (1959)
148. J. Lindhard, M. Scharff, Phys. Rev. **124**, 128 (1961)
149. J. Lindhard, M. Scharff, H.E. Schiott, Dan. Vidensk. Seksk. Mat. Fys. Medd. **33**, 1 (1963)
150. W. Brandt, M. Kitagawa, Phys. Rev. B **25**, 5631 (1982)
151. D. Cai, N. Grønbech-Jensen, C.M. Snell, K.M. Beardmore, Phys. Rev. B **54**, 17147 (1996)
152. J. Sillanpää, K. Nordlund, J. Keinonen, Phys. Rev. B **62**, 3109 (2000)
153. K.M. Beardmore, N. Grønbech-Jensen, Phys. Rev. E **57**, 7278 (1998)
154. M. Jaraiz, L. Pelaz, E. Rubio, J. Barbolla, G.H. Gilmer, D.J. Eaglesham, H.J. Gossmann, J.M. Poate, Mater. Res. Soc. Symp. Proc. **54**, 532 (1998)
155. G. Hobler, G. Otto, D. Kovač, L. Palmetshofer, K. Mayerhofer, K. Piplits, Nucl. Instrum. Methods Phys. Res. B **228**, 360 (2005)
156. See for example description of the 'Kinetic Adaptive Damage Model' of UT-MARLOWE, `http://homer.mer.utexas.edu`
157. L.M. Howe, M.H. Rainville, Nucl. Instrum. Methods **182/183**, 143 (1981)
158. P. Sigmund, Appl. Phys. Lett. **14**, 114 (1969)
159. G. Hobler, A. Simionescu, L. Pametshofer, C. Tian, G. Stingeder, J. Appl. Phys. **77**, 3697 (1995)
160. G. Hobler, Nucl. Instrum. Methods Phys. Res. B **96**, 155 (1995)

161. For example, description of the 'Kinchin-Pease Damage Model' of UT-MARLOWE, `http://homer.mer.utexas.edu`
162. J.M. Hernández-Mangas, J. Arias, L.A. Marqués, A. Ruiz-Bueno, L. Bailón, Nucl. Instrum. Methods Phys. Res. B **228**, 235 (2005)
163. S.H. Yang, S. Morris, S. Tian, K. Karab, A.F. Tasch, P.M. Echenique, R. Capaz, J. Joannopoulos, Mat. Res. Soc. Symp. Proc. **389**, 77 (1995)
164. W. Bohmayr, A. Burenkov, J. Lorenz, H. Ryssel, S. Selberherr, IEEE Trans. Semic. Manuf. **8**, 402 (1995)
165. M. Posselt, Radiat. Eff. Defects Solids **130**, 87 (1994)
166. J. Arias, M. Jaraiz, L. Pelaz, L. Bailón, J. Barbolla, Nucl. Instrum. Methods Phys. Res. B **102**, 228 (1995)
167. J. Arias, M. Jaraiz, J.E. Rubio, L. Pelaz, L.A. Marqués, J. Barbolla, J. Mat. Sci. Tech. **11**, 1191 (1995)
168. K. Gärtner, D. Stock, B. Weber, G. Betz, M. Hautala, G. Hobler, M. Hou, S. Arite, W. Eckstein, J.J. Jiménez-Rodríguez et al., Nucl. Instrum. Methods Phys. Res. B **102**, 183 (1995)
169. K. Nordlund, Comp. Mater. Sci. **3**, 448 (1995)
170. I. Santos, L.A. Marqués, L. Pelaz, Phys. Rev. B **74**, 174115 (2006)
171. T. Aoki, J. Matsuo, G. Takaoka, Nucl. Instrum. Methods Phys. Res. B **202**, 278 (2003)
172. R.P. Webb, S.H. Winston, R.M. Gwilliam, B.J. Sealy, G. Boudreault, C. Jeynes, K.J. Kirkby, Nucl. Instrum. Methods Phys. Res. B **202**, 143 (2003)
173. T. Aoki, J. Matsuo, G. Takaoka, N. Toyoda, I. Yamada, Nucl. Instrum. Methods Phys. Res. B **206**, 855 (2006)
174. J. Borland, S. Shishiguchi, A. Mineji, W. Krull, D. Jacobson, M. Tanjyo, W. Lerch, S. Paul, J. Gelpey, S. McCoy et al., in *International Workshop on Junction Technology* (2006), p. 4
175. J. Borland, H. Kiyama, in *Proceedings of the 17th International Conference on Ion Implantation Technology* (2008), Vol. 1066, p. 63
176. R. Smith, D.E. Harrison, B.J. Garrison, Phys. Rev. B **40**, 93 (1989)
177. H. Zhu, Nucl. Instrum. Methods Phys. Res. B **83**, 334 (1993)
178. L.A. Marqués, J.E. Rubio, M. Jaraíz, L. Enríquez, J. Barbolla, Nucl. Instrum. Methods Phys. Res. B **102**, 7 (1995)
179. M. Jaraíz, G.H. Gilmer, D.M. Stock, T.D. de la Rubia, Nucl. Instrum. Methods Phys. Res. B **102**, 180 (1995)
180. M. Posselt, Mater. Sci. Semicond. Process. **3**, 317 (2000)
181. G. Hobler, G. Otto, Nucl. Instrum. Methods Phys. Res. B **206**, 81 (2003)
182. D. Kovač, G. Otto, G. Hobler, Nucl. Instrum. Methods Phys. Res. B **228**, 226 (2005)
183. D. Kovač, G. Hobler, Nucl. Instrum. Methods Phys. Res. B **267**, 1229 (2009)
184. I. Santos, L.A. Marqués, L. Pelaz, P. López, J. Appl. Phys. **105**, 083530 (2009)
185. P.M. Fahey, P.B. Griffin, J.D. Plummer, Rev. Mod. Phys. **61**, 289 (1989)
186. T.Y. Tan, U. Gösele, Appl. Phys. A: Solids Surf. **37**, 1 (1985)
187. H. Föll, U. Gösele, B.O. Kolbesen, J. Cryst. Growth **52**, 907 (1981)
188. R. Falster, V.V. Voronkov, F. Quast, Phys. Status Solidi B **222**, 219 (2000)
189. T. Sinno, E. Dornberger, W. von Ammon, R.A. Brown, F. Dupret, Mater. Sci. Eng. R **28**, 149 (2000)
190. S. Lee, G.S. Hwang, Phys. Rev. B **78**, 045204 (2008)
191. A. Claverie, B. Colombeau, B.D. Mauduit, C. Bonafos, X. Hebras, G.B. Assayag, F. Cristiano, Appl. Phys. A **76**, 1025 (2003)
192. P. Pichler, *Intrinsic Point Defects, Impurities, and Their Diffusion in Silicon* (Springer, Wien, 2004)
193. G.D. Watkins, J.W. Corbett, Phys. Rev. **134**, A1359 (1964)
194. J.P. Goss, P. Briddon, R. Jones, J. Phys.: Condens. Matter **16**, 3311 (2004)
195. S. Dannefaer, P. Mascher, D. Kerr, Phys. Rev. Lett. **56**, 2195 (1986)
196. H. Bracht, N.A. Stolwijk, H. Mehrer, Phys. Rev. B **52**, 16542 (1995)
197. M.I.J. Probert, M.C. Payne, Phys. Rev. B **67**, 075204 (2003)
198. J. Lento, R.M. Nieminen, J. Phys.: Condens. Matter **15**, 4387 (2003)
199. E. Domberger, D. Temmler, W. von Ammon, J. Electrochem. Soc. **149**, G226 (2002)
200. R. Winkler, G. Behnke, *Semiconductor Silicon* (The Electrochemical Society, Pennington, NJ, 1994), Vol. 94
201. E.G. Roth, O.W. Holland, J.L. Duggan, in *Proceedings of Application of Accelerators in Research and Industry, Pts 1 and 2* (1999), Vol. 475, p. 804
202. J. Xu, E.G. Roth, O.W. Holland, A.P. Mills, R. Suzuki, Appl. Phys. Lett. **74**, 997 (1999)
203. A.J. Smith, N.E.B. Cowern, R. Gwilliam, B.J. Sealy, B. Colombeau, E.J.H. Collart, S. Gennaro, D. Giubertoni, M. Bersani, M. Barozzi, Appl. Phys. Lett. **88**, 082112 (2006)
204. E. Bruno, S. Mirabella, F. Priolo, E. Napolitani, C. Bongiorno, V. Raineri, J. Appl. Phys. **101**, 023515 (2007)
205. M. Itsumi, H. Akiya, T. Ueki, M. Tomita, M. Yamawaki, J. Appl. Phys. **78**, 5984 (1995)
206. D.J. Eaglesham, A.E. White, L.C. Feldman, D.C. Jacobson, Phys. Rev. Lett. **70**, 1643 (1993)
207. A. Bongiorno, L. Colombo, T.D.D. la Rubia, Europhys. Lett. **43**, 695 (1998)
208. M. Prasad, T. Sinno, Phys. Rev. B **68**, 045206 (2003)
209. S. Lee, G.S. Hwang, Phys. Rev. B **78**, 125310 (2008)
210. T.E.M. Staab, A. Sieck, M. Haugk, M. Puska, T. Frauenheim, H. Leipner, Phys. Rev. B **65**, 115210 (2002)
211. J.L. Hastings, S.K. Estreicher, P. Fedders, Phys. Rev. B **56**, 10215 (1997)
212. V.C. Venezia, L. Pelaz, H.J.L. Gossmann, T.H. haynes, C.S. Rafferty, Phys. Rev. Lett. **79**, 1273 (2001)
213. R. Kalyanaraman, T.E. Haynes, O.W. Holland, H.J.L. Gossmann, C.S. Rafferty, G.H. Gilmer, Appl. Phys. Lett. **79**, 1983 (2001)
214. S. Takeda, M. Kohyama, K. Ibe, Philos. Mag. A **70**, 287 (1994)
215. A.E. Michel, W. Rausch, P.A. Ronsheim, R.H. Kastl, Appl. Phys. Lett. **50**, 416 (1987)
216. R. Car, P.J. Kelly, A. Oshiyama, S.T. Pantelides, Phys. Rev. Lett. **52**, 1814 (1984)
217. R. Car, P. Blöchl, E. Smargiassi, Mater. Sci. Forum **83–87**, 433 (1992)
218. J. Zhu, L.H. Yang, C. Mailhiot, T.D. de la Rubia, G.H. Gilmer, Nucl. Instrum. Methods Phys. Res. B **102**, 29 (1995)

219. W.K. Leung, R.J. Needs, G. Rajagopal, S. Itoh, S. Ihara, Phys. Rev. Lett. **83**, 2351 (1999)
220. R.J. Needs, J. Phys.: Condens. Matter **11**, 10437 (1999)
221. T.J. Lenosky, J.D. Kress, I. Kwon, A.F. Voter, B. Edwards, D.F. Richards, S. Yang, J.B. Adams, Phys. Rev. B **55**, 1528 (1997)
222. I.P. Batra, F.F. Abraham, S. Ciraci, Phys. Rev. B **35**, 9552 (1987)
223. H.R. Schober, Phys. Rev. B **39**, 13013 (1989)
224. D. Maroudas, R.A. Brown, Appl. Phys. Lett. **62**, 172 (1993)
225. D. Maroudas, R.A. Brown, Phys. Rev. B **47**, 15562 (1993)
226. D. Maroudas, S.T. Pantelides, Chem. Eng. Sci. **49**, 3001 (1994)
227. G.H. Gilmer, T.D. de la Rubia, D.M. Stock, M. Jaraiz, Nucl. Instrum. Methods Phys. Res. B **102**, 247 (1995)
228. T. Sinno, K. Jiang, R.A. Brown, Appl. Phys. Lett. **68**, 3028 (1996)
229. M. Nastar, V.V. Bulatov, S. Yip, Phys. Rev. B **53**, 13521 (1996)
230. M. Hane, T. Ikezawa, A. Furukawa, IEICE Trans. Electron. **E83-C**, 1247 (2000)
231. L. Colombo, Physica B **273–274**, 458 (1999)
232. M.P. Chichkine, M.M.D. Souza, E.M.S. Narayanan, Phys. Rev. Lett. **88**, 085501 (2002)
233. I. Martín-Bragado, M. Jaraiz, P. Castrillo, R. Pinacho, J. Barbolla, M.M.D. Souza, Phys. Rev. B **68**, 195204 (2003)
234. J.P. Goss, P. Briddon, T.A.G. Eberlein, R. Jones, N. Pinho, A. Blumenau, S. Öberg, Appl. Phys. Lett. **85**, 4633 (2004)
235. W.L. Ng, M.A. Lourenco, R.M. Gwilliam, S. Ledain, G. Shao, K.P. Homewood, Nature **410**, 192 (2001)
236. N. Arai, S. Takeda, M. Kohyama, Phys. Rev. Lett. **78**, 4265 (1997)
237. S. Takeda, Jap. J. Appl. Phys. **30**, L639 (1991)
238. F. Cristiano, N. Cherkashin, X. Hebras, P. Calvo, Y. Lamrani, E. Scheid, B. de Mauduit, B. Colombeau, W. Lerch, S. Paul et al., Nucl. Instrum. Methods Phys. Res. B **216**, 46 (2004)
239. M. Kohyama, S. Takeda, Phys. Rev. B **46**, 12305 (1992)
240. J.P. Goss, T.A.G. Eberlein, R. Jones, N. Pinho, A. Blumenau, T. Frauenheim, P. Briddon, S. Öberg, J. Phys. Condens. Mat. **14**, 12843 (2002)
241. J. Li, K. Jones, Appl. Phys. Lett. **73**, 3648 (1998)
242. H. Park, J.W. Wilkins, Phys. Rev. B **79**, 241203 (2009)
243. S.K. Estreicher, M. Gharaibeh, P.A. Fedders, P. Ordejón, Phys. Rev. Lett. **86**, 1247 (2001)
244. G. Hobler, C.S. Rafferty, in *Materials Research Society Symposium Proceedings*, edited by H.J.L. Gossmann, T.E. Haynes, M.E. Law, A.N. Larsen, S. Odanaka (1999)
245. F. Cristiano, J. Grisolia, B. Colombeau, M. Omri, B. de Mauduit, A. Claverie, F.L. Giles, J. Appl. Phys. **87**, 8420 (2000)
246. C. Zechner, N. Zographos, D. Matveev, A. Erlebach, Mater. Sci. Eng. B **124–125**, 401 (2005)
247. N. Zographos, C. Zechner, I. Avci, Mater. Res. Soc. Symp. Proc. **994**, 0994 (2007)
248. A.H. Gencer, S.T. Dunham, J. Appl. Phys. **81**, 631 (1997)
249. D. Stiebel, P. Pichler, N.E.B. Cowern, Appl. Phys. Lett. **79**, 2654 (2001)
250. A.H. Gencer, S.T. Dunham, J. Appl. Phys. **91**, 2883 (2002)
251. E. Lampin, V. Senez, A. Claverie, Mater. Sci. Eng. B **71**, 155 (2000)
252. M.D. Giles, J. Electrochem. Soc. **138**, 1160 (1991)
253. G. Hobler, V. Moroz, in *Proceedings of the 30th European Solid-State Device Research Conference (ESSDERC)*, edited by W.A. Lane, G.M. Crean, F.A. McCabe, H. Grünbacher (2000)
254. L. Pelaz, L.A. Marqués, M. Aboy, J. Barbolla, G.H. Gilmer, Appl. Phys. Lett. **82**, 2038 (2003)
255. L. Pelaz, G.H. Gilmer, M. Jaraiz, S.B. Herner, H.J. Gossmann, D.J. Eaglesham, G. Hobler, C.S. Rafferty, J. Barbolla, Appl. Phys. Lett. **73**, 1421 (1998)
256. L. Pelaz, G.H. Gilmer, V.C. Venezia, H.J. Gossmann, M. Jaraiz, J. Barbolla, Appl. Phys. Lett. **74**, 2017 (1999)
257. G. Hobler, L. Pelaz, C.S. Rafferty, J. Electrochem. Soc. **147**, 3494 (2000)
258. I. Martín-Bragado, M. Jaraiz, P. Castrillo, R. Pinacho, J.E. Rubio, J. Barbolla, Appl. Phys. Lett. **84**, 4962 (2004)
259. L. Pelaz, M. Aboy, P. López, L.A. Marqués, J. Vac. Sci. Technol. B **24**, 2432 (2006)
260. M. Aboy, L. Pelaz, L.A. Marqués, L. Enríquez, J. Barbolla, J. Appl. Phys. **94**, 1013 (2003)
261. A. Claverie, F. Cristiano, B. Colombeau, E. Scheid, B.D. Mauduit, in *Proceedings of the 14th International Conference on Ion Implantation* (2002)
262. C.J. Ortiz, T. Fuhner, P. Pichler, F. Cristiano, B. Colombeau, N.E.B. Cowern, A. Claverie, J. Appl. Phys. **96**, 4866 (2004)
263. C.S. Rafferty, G.H. Gilmer, M. Jaraiz, D.J. Eaglesham, H.J. Gossman, Appl. Phys. Lett. **68**, 2395 (1996)
264. P. Castrillo, I. Martín-Bragado, R. Pinacho, J.E. Rubio, K.R.C. Mok, F.J. Miguel-Herrero, J. Barbolla, Mater. Sci. Eng. B **124–125**, 404 (2005)
265. I. Avci, M.E. Law, E. Kuryliw, A.F. Saavedra, K.S. Jones, J. Appl. Phys. **95**, 2452 (2004)
266. E. Landi, A. Armigliato, S. Solmi, R. Köghler, E. Wieser, Appl. Phys. A **47**, 359 (1998)
267. D. Takeuchi, H. Shimada, J. Matsuo, I. Yamada, Nucl. Instrum. Methods Phys. Res. B **121**, 345 (1997)
268. Y. Kawasaki, T. Kuroi, T. Yamashita, K. Horita, T. Hayashi, M. Ishibashi, M. Togawa, Y. Ohno, M. Yoneda, T. Horsky et al., Nucl. Instrum. Methods Phys. Res. B **237**, 25 (2005)
269. G. Hobler, G. Otto, Mat. Sci. Semicond. Process. **6**, 1 (2003)
270. G. Holmen, J. Linnros, B. Svensson, Appl. Phys. Lett. **45**, 1116 (1984)
271. J. Linnros, B. Svensson, G. Holmen, Phys. Rev. B **30**, 3629 (1984)
272. D.A. Thompson, A. Golanski, H. Haugen, L.M. Howe, J.A. Davies, Radiat. Eff. **50**, 125 (1980)
273. R.G. Elliman, J. Linnros, W.L. Brown, Mater. Res. Soc. Symp. Proc. **100**, 363 (1988)
274. J. Linnros, R.G. Elliman, W.L. Brown, J. Mater. Res. **3**, 1208 (1988)
275. D.N. Seidman, R.S. Averback, P.R. Okamoto, A.C. Baily, Phys. Rev. Lett. **58**, 900 (1987)
276. S. Takeda, J. Yamasaki, Phys. Rev. Lett. **83**, 320 (1999)
277. S. Takeda, J. Yamasaki, Y. Kimura, Physica B **273–274**, 476 (1999)
278. T. Motooka, Phys. Rev. B **49**, 16367 (1994)
279. K.A. Jackson, J. Mater. Res. **3**, 1218 (1988)

280. J.S. Williams, R.G. Elliman, Phys. Rev. Lett. **51**, 1069 (1983)
281. F. Priolo, E. Rimini, Mater. Sci. Rep. **5**, 319 (1990)
282. D.M. Stock, B. Weber, K. Gärtner, Phys. Rev. B **61**, 8150 (2000)
283. S. Goedecker, T. Deutsch, L. Billard, Phys. Rev. Lett. **88**, 235501 (2002)
284. L.A. Marqués, L. Pelaz, J. Hernández, J. Barbolla, G.H. Gilmer, Phys. Rev. B **64**, 45214 (2001)
285. B. Weber, D.M. Stock, K. Gärtner, Mater. Sci. Eng. B **71**, 213 (2000)
286. L.A. Marqués, L. Pelaz, M. Aboy, L. Enríquez, J. Barbolla, Phys. Rev. Lett. **91**, 135504 (2003)
287. G.L. Olson, J.A. Roth, Mater. Sci. Reports **3**, 1 (1988)
288. L. Pelaz, L.A. Marqués, M. Aboy, J. Barbolla, Defect and Diffusion Forum **221**, 31 (2003)
289. P. López, L. Pelaz, L.A. Marqués, I. Santos, J. Appl. Phys. **101**, 093518 (2007)
290. Y. Masaki, P.G. LeComber, A.G. Fitzgerald, J. Appl. Phys. **74**, 129 (1993)
291. R.D. Goldberg, J.S. Williams, R.G. Elliman, Nucl. Instrum. Methods Phys. Res. B **106**, 242 (1995)
292. G.L. Olson, J.A. Roth, Handbook of crystal growth **3**, 255 (1994)
293. A. Battaglia, F. Priolo, E. Rimini, Nucl. Instrum. Methods Phys. Res. B **59**, 382 (1991)
294. A. Battaglia, S.U. Campisano, J. Appl. Phys. **74**, 6058 (1993)
295. R.D. Goldberg, R.G. Elliman, J.S. Williams, Nucl. Instrum. Methods Phys. Res. B **80/81**, 596 (1993)
296. J.S. Williams, Mater. Res. Soc. Symp. Proc. **51**, 83 (1985)
297. E.C. Baranova, V.M. Gusev, Y.V. Martynenko, C.V. Starinin, I.B. Haibullin, Radiat. Eff. **18**, 21 (1973)
298. P. López, L. Pelaz, L.A. Marqués, I. Santos, M. Aboy, J. Barbolla, Mater. Sci. Eng. B **114**, 82 (2004)
299. J.E. Rubio, M. Jaraiz, I. Martín-Bragado, R. Pinacho, P. Castrillo, J. Barbolla, Mater. Sci. Eng. B **114**, 151 (2004)
300. K.R.C. Mok, F. Benistant, M. Jaraiz, J.E. Rubio, P. Castrillo, R. Pinacho, M.P. Srinivasan, J. Appl. Phys. **103**, 014911 (2008)
301. J.R. Dennis, E.B. Hale, J. Appl. Phys. **49**, 1119 (1978)
302. F.L. Vook, in *Radiation Damage and Defects in Semiconductors*, edited by J.E. Whitehouse (London, 1973), Inst. Phys. Conf. Ser. No. 16, p. 60
303. H.J. Stein, Radiat. Eff. **6**, 19 (1970)
304. S.T. Picraux, W. Weisenberger, F.L. Vook, Radiat. Eff. **7**, 101 (1971)
305. S.T. Picraux, F.L. Vook, Radiat. Eff. **11**, 179 (1971)
306. H. Cerva, G. Hobler, J. Electrochem. Soc. **139**, 3631 (1992)
307. I. Avci, M.E. Law, E. Kuryliw, K.S. Jones, IEDM Technical Digest (2001), p. 835
308. S. Morarka, N.G. Rudawski, M.E. Law, K.S. Jones, R.G. Elliman, J. Appl. Phys. **105**, 053701 (2009)
309. L. Csepregi, E.F. Kennedy, J.W. Mayer, T.W. Sigmon, J. Appl. Phys. **49**, 3906 (1978)
310. B. Drosd, J. Washburn, J. Appl. Phys. **51**, 4106 (1980)
311. A. Armigliato, D. Nobili, P. Ostoja, M. Servidori, S. Solmi (1977)
312. T. Yoshikawa, K. Morita, J. Electrochem. Soc. **150**, G465 (2003)
313. S. Haridoss, A.R.F. Bénière, M. Gauneau, J. Appl. Phys. **51**, 5833 (1980)
314. S. Solmi, A. Parisini, M. Bersani, D. Giubertoni, V. Soncini, G. Carnevale, A. Benvenuti, A. Marmiroli, J. Appl. Phys. **92**, 1361 (2002)
315. S. Solmi, A. Parisini, R. Angelucci, A. Armigliato, D. Nobili, L. Moro, Phys. Rev. B **53**, 7836 (1996)
316. D. Nobili, S. Solmi, A. Parisini, M. Derdour, A. Armigliato, L. Moro, Phys. Rev. B **49**, 2477 (1994)
317. D. Nobili, R. Angelucci, A. Armigliato, E. Landi, S. Solmi, J. Electrochem. Soc. **136**, 1142 (1989)
318. S.M. Hu, Mater. Sci. Eng. R **13**, 105 (1994)
319. H. Bracht, MRS Bulletin on Defects and Diffusion in Silicon Technology **25**, 22 (2000)
320. K.C. Pandey, Phys. Rev. Lett. **57**, 2287 (1986)
321. H.J. Gossmann, T.E. Haynes, P.A. Stolk, D.C. Jacobson, G.H. Gilmer, J.M. Poate, H.S. Luftman, T.K. Mogi, M.O. Thompson, Appl. Phys. Lett. **71**, 3862 (1997)
322. I. Martin-Bragado, P. Castrillo, M. Jaraiz, R. Pinacho, J.E. Rubio, J. Barbolla, Phys. Rev. B **72**, 35202 (2005)
323. I. Martin-Bragado, P. Castrillo, M. Jaraiz, R. Pinacho, J.E. Rubio, J. Barbolla, V. Moroz, J. Appl. Phys. **98**, 053709 (2005)
324. P. Alippi, L. Colombo, P. Ruggerone, A. Sieck, G. Seifert, T. Frauenheim, Phys. Rev. B **64**, 075207 (2001)
325. A. Ural, P.B. Griffin, J.D. Plummer, J. Appl. Phys. **85**, 6440 (1999)
326. N.E.B. Cowern, K.T.F. Janssen, G.F.A. van de Walle, D.J. Gravesteijn, Phys. Rev. Lett. **65**, 2434 (1990)
327. D. De Salvador, E. Napolitani, S. Mirabella, G. Bisognin, G. Impellizzeri, A. Carnera, F. Priolo, Phys. Rev. Lett. **97**, 255902 (2006)
328. S. Matsumoto, Y. Ishikawa, T. Niimi, J. Appl. Phys. **54**, 5049 (1983)
329. D. Mathiot, J.C. Pfister, J. Appl. Phys. **55**, 3518 (1984)
330. N.E.B. Cowern, J. Appl. Phys. **64**, 4484 (1988)
331. P. Novell, M.E. Law, in *Proc. of the NUPAD IV* (IEEE, New York, 1992), pp. 41–44
332. S. Whelan, V. Privitera, G. Mannino, M. Italia, C. Bongiorno, A.L. Magna, J. Appl. Phys. **94**, 3873 (2001)
333. S.A. Harrison, *Ph.D. Thesis: First Principles Modeling of Arsenic and Fluorine Behavior in Crystalline Silicon during Ultrashallow Junction Formation* (University of Texas at Austin, 2006)
334. O. Sugino, A. Oshiyama, Phys. Rev. B **46**, 12335 (1992)
335. E.L. Elkin, G.D. Watkins, Phys. Rev. **174**, 881 (1968)
336. M. Hirata, M. Hirata, H. Saito, J. Phys. Soc. Jpn **27**, 405 (1969)
337. B. Baccus, T. Wada, N. Shigyo, M. Norishima, H. Nakajima, K. Inou, T. Iinuma, H. Iwai, IEEE Trans. Elec. Dev. **39**, 648 (1992)
338. M. Hane, T. Ikezawa, M. Hiroi, H. Matsumoto, in *IEEE International Electron Devices Meeting* (1996), pp. 803–806
339. R. Pinacho, M. Jaraiz, P. Castrillo, I. Martin-Bragado, J.E. Rubio, J. Barbolla, Appl. Phys. Lett. **86**, 252103 (2005)
340. S.A. Harrison, T.F. Edgar, G.S. Hwang, Appl. Phys. Lett. **87**, 231905 (2005)
341. R. Kim, T. Hirose, T. Shano, H. Tsuji, K. Taniguchi, Jpn J. Appl. Phys. **41**, 227 (2002)
342. A. Nylandsted Larsen, K. Kyllesbech Larsen, P.E. Andersen, B.G. Svensson, J. Appl. Phys. **73**, 691 (1993)
343. A. Nylandsted Larsen, S.Y. Shiryaev, E.S. Sorensen, P. Tidemand-Petersson, Appl. Phys. Lett. **48**, 1805 (1986)

344. D. Mathiot, J.C. Pfister, Appl. Phys. Lett. **42**, 1043 (1983)
345. R.O. Schwenker, E.S. Pan, R.F. Lever, J. Appl. Phys. **42**, 3195 (1971)
346. W.K. Chu, Appl. Phys. Lett. **36**, 273 (1980)
347. H.J. Gossmann, G.H. Gilmer, C.S. Rafferty, F.C. Unterwald, T. Boone, J.M. Poate, H.S. Luftman, W. Frank, J. Appl. Phys. **77**, 1948 (1995)
348. M. Aboy, L. Pelaz, L.A. Marqués, P. López, J. Barbolla, J. Appl. Phys. **97**, 103520 (2005)
349. P. Alippi, P. Ruggerone, L. Colombo, Phys. Rev. B **69**, 125205 (2004)
350. M. Aboy, L. Pelaz, L.A. Marqués, J. Barbolla, A. Mokhberi, Y. Takamura, P.B. Griffin, J.D. Plummer, Appl. Phys. Lett. **83**, 4166 (2003)
351. S. Boninelli, S. Mirabella, E. Bruno, F. Priolo, F. Cristiano, A. Claverie, D. De Salvador, G. Bisognin, E. Napolitani, Appl. Phys. Lett. **91**, 031905 (2007)
352. D. De Salvador, E. Napolitani, G. Bisognin, A. Carnera, E. Bruno, S. Mirabella, G. Impellizzeri, F. Priolo, Appl. Phys. Lett. **87**, 221902 (2005)
353. M. Aboy, L. Pelaz, P. López, E. Bruno, S. Mirabella, E. Napolitani, Mater. Sci. Eng. B **144–145**, 247 (2008)
354. S. Mirabella, E. Bruno, F. Priolo, D. De Salvador, E. Napolitani, A.V. Drigo, A. Carnera, Appl. Phys. Lett. **83**, 680 (2003)
355. V.C. Venezia, R. Duffy, L. Pelaz, M. Aboy, A. Heringa, P.B. Griffin, C.C. Wang, M.J.P. Hopstaken, Y. Tamminga, T. Dao et al., in *IEEE International Electron Devices Meeting* (2003), pp. 20.3.1–4
356. A. Mattoni, L. Colombo, Phys. Rev. B **69**, 45204 (2004)
357. A.D. Lilak, S.K. Earles, K.S. Jones, M.E. Law, in *IEEE International Electron Devices Meeting* (1996), pp. 493–496
358. J. Schermer, A. Martinez-Limia, P. Pichler, C. Zechner, W. Lerch, S. Paul, Solid State Electronics **52**, 1424 (2008)
359. P.M. Rousseau, P.B. Griffin, W.T. Fang, J.D. Plummer, J. Appl. Phys. **84**, 3593 (1998)
360. R.C. Pandey, A. Erbil, G.S. Cargill, R.F. Boehme, D. Vanderbilt, Phys. Rev. Lett. **61**, 1282 (1988)
361. V. Ranki, J. Nissilä, K. Saarinen, Phys. Rev. Lett. **88**, 105506 (2002)
362. J. Xie, S. Chen, Phys. Rev. Lett. **83**, 1795 (1999)
363. D.C. Mueller, E. Alonso, W. Fichtner, Phys. Rev. B **68**, 045208 (2003)
364. R. Brindos, P. Keys, K. Jones, M. Law, Appl. Phys. Lett. **75**, 229 (1999)
365. S.A. Harrison, T.F. Edgar, G.S. Hwang, Electrochemical and Solid-State Letters **9**, G354 (2006)
366. A. Martinez-Limia, P. Pichler, W. Lerch, S. Paul, H. Kheyrandish, A. Pakfar, C. Tavernier, Mater. Sci. Eng. B **154–155**, 211 (2008)
367. K.S. Jones, D.K. Sadana, S. Prussin, J. Washburn, E.R. Weber, W.J. Hamilton, J. Appl. Phys. **63**, 1414 (1988)
368. R. Duffy, V.C. Venezia, A. Heringa, T.W.T. Hüsken, M.J.P. Hopstaken, N.E.B. Cowern, P.B. Griffin, C.C. Wang, Appl. Phys. Lett. **82**, 3647 (2003)
369. L. Pelaz, M. Aboy, P. López, L.A. Marqués, I. Santos, Nucl. Instrum. Methods Phys. Res. B **253**, 41 (2006)
370. A. Mokhberi, P.B. Griffin, J.D. Plummer, E. Paton, S. McCoy, K. Elliot, IEEE Trans. Elec. Dev. **49**, 1183 (2002)
371. M. Aboy, L. Pelaz, L.A. Marqués, P. López, J. Barbolla, R. Duffy, V.C. Venezia, P.B. Griffin, Appl. Phys. Lett. **86**, 031908 (2005)
372. S. Severi, K. Henson, R. Lindsay, A. Lauwers, B.J. Pawlak, R. Surdeanu, K.D. Meyer, Mat. Res. Soc. Symp. Proc. **810**, 455 (2004)
373. R. Duffy, M. Aboy, V.C. Venezia, S. Severi, B.J. Pawlak, P. Eyben, F. Roozeboom, L. Pelaz, IEEE Trans. Elec. Dev. **53**, 71 (2006)
374. M. van Dal, N. Collaert, G. Doornbos, G. Vellianitis, G. Curatola, B. Pawlak, R. Duffy, C. Jonville, B. Degroote, E. Altamirano et al., in *Symp. VLSI Tech. Dig.* (2007), pp. 110–111
375. H.J. Gossmann, A. Agarwal, T. Parrill, L.M. Rubin, J.M. Poate, IEEE Trans. Nanotechnology **2**, 285 (2003)
376. W. Vandervorst, J. Everaert, E. Rosseel, M. Jurczak, T. Hoffman, P. Eyben, J. Mody, G. Zschatzsch, S. Koelling, M. Gilbert et al., Ion Implantation Technology Conf. Proc. **1066**, 446 (2008)
377. M. van Dal, R. Duffy, B. Pawlak, N. Collaert, M. Jurczak, R. Lander, Mat. Res. Symp. Proc. **1070**, 67 (2008)
378. L. Pelaz et al., accepted for publication in J. Vac. Sci. Technol. B
379. R. Duffy, G. Curatola, B. Pawlak, G. Doornbos, K. van der Tak, P. Breimer, J. van Berkum, F. Roozeboom, J. Vac. Sci. Technol. B **26**, 402 (2008)
380. R. Duffy, M. van Dal, B. Pawlak, M. Kaiser, R. Weemaes, B. Degroote, E. Lunnen, E. Altamirano, Appl. Phys. Lett. **90**, 241912 (2007)
381. E. Collart, S. Felch, B. Pawlak, P. Absil, S. Severi, T. Janssens, W. Vandervorst, J. Vac. Sci. Technol. B **24**, 507 (2006)
382. K. Suzuki, Y. Kataoka, S. Nagayamaa, C.W. Magee, T.H. Buyuklimanli, T. Nagayama, IEEE Trans. Elec. Dev. **54**, 262 (2007)
383. N. Zographos, I. Martin-Bragado, in *Mat. Res. Soc. Symp. Proc.* (2008), Vol. 1070, pp. E03–01
384. S. Jain, P.B. Griffin, J.D. Plummer, S. Mccoy, J. Gelpey, T. Selinger, D.F. Downey, J. Appl. Phys. **96**, 7357 (2004)
385. R. Duffy, V.C. Venezia, A. Heringa, M.J.P. Hopstaken, G.C.J. Maas, T. Dao, Y. Tamminga, F. Roozeboom, in *Mat. Res. Soc. Symp. Proc.* (2005), Vol. 810, p. C10.2
386. M.J.P. Hopstaken, Y. Tamminga, M.A. Verheijen, R. Duffy, V.C. Venezia, A. Heringa, Appl. Surf. Phys. **231–232**, 688 (2004)
387. J. Dabrowski, H. Müssg, V. Zavodinski, R. Baierle, M.J. Caldas, Phys. Rev. B **65**, 245305 (2002)
388. C. Steen, A. Martinez-Limia, P. Pichler, H. Ryssel, S. Paul, W. Lerch, L. Pei, G. Duscher, F. Severac, F. Cristiano et al., J. Appl. Phys. **104**, 023518 (2008)
389. M.S. Daw, W. Windl, N.N. Carlson, M. Laudon, M.P. Masquelier, Phys. Rev. B **64**, 045205 (2001)
390. M.J. Aziz, Y. Zhao, H.J. Gossmann, S. Mitha, S.P. Smith, D. Schiferl, Phys. Rev. B **73**, 054101 (2006)
391. I. Martin-Bragado, I. Avci, K.E. Sayed, V. Koltyzhenkov, E. Lyumkis, M.D. Johnson, J. Comput. Electron. **7**, 103 (2008)
392. V. Moroz, I. Martin-Bragado, S. Felch, F. Nouri, C. Olsen, K.S. Jones, J. Vac. Sci. Technol. B **26**, 439 (2008)